Delayed Ionospheric Response to Solar EUV/UV Radiation Variations

Von der Fakultät für Physik und Geowissenschaften

der Universität Leipzig genehmigte

Dissertation

zur Erlangung des akademischen Grades

"doctor rerum naturalium" (Dr. rer. nat.)

UNIVERSITÄT LEIPZIG

vorgelegt von Rajesh Ishwardas Vaishnav, M. Sc. Physics,

geboren am 21 February 1990 in Rajasthan, India

Gutachter:

Prof. Dr. Ch. Jacobi

Dr. Jan Laštovička

Tag der Verleihung: 19. Oktober 2021

Bibliographische Beschreibung

Vaishnav, Rajesh Ishwardas

Delayed Ionospheric Response to Solar EUV/UV Radiation Variations

Universität Leipzig, Dissertation

103 pp., 191 bibl., 55 fig.

Kurzzusammenfassung

Die Veränderungen des Thermosphäre-Ionosphäre (T-I) Systems und dessen Komplexität werden entscheidend durch die sich ständig ändernde extreme ultraviolette (EUV) und ultraviolette (UV) Sonnenstrahlung geprägt. Hierbei wird die ionosphärische Elektronendichte (oder Ionendichte) hauptsächlich durch Photoionisation, Rekombination und Transportprozesse gesteuert. Insbesondere Transportprozesse spielen eine wichtige Rolle für die Zusammensetzung des T-I-Systems und sind für die Plasmaverteilung verantwortlich.

Die ionosphärische Reaktion auf Veränderungen der Sonnenaktivität wurde mithilfe des Gesamtelektronengehalts (englisch total electron content, TEC) und Messdaten des solaren EUV-Spektrums sowie solaren Proxys untersucht. Eine ionosphärische Verzögerung von 1 bis 2 Tagen für Tageswerte von TEC wurde für die 27-Tage-Sonnenrotation gefunden. Es wurde auch gezeigt, dass der He-II-Index einer der besten solaren Proxys ist, um die Sonnenaktivität auf verschiedenen Zeitskalen zu beschreiben.

Die ionosphärische Verzögerung in Bezug auf Variationen der Sonnenstrahlung wurde in der Vergangenheit wenig Aufmerksamkeit gewidmet. Insbesondere die zugrundenliegenden Mechanismen wurden nicht untersucht. Solche Studien sind jedoch von entscheidender Bedeutung für ein besseres Verständnis der komplexen Wechselwirkungen zwischen Sonnenstrahlung und Ionosphäre, die unteranderem die Leistung von Radiokommunikation

und globalen Navigationssystemen beeinflussen. Das T-I-System wird jedoch nicht nur von der solaren EUV-Strahlung kontrolliert. Prozesse der unteren Atmosphäre, geomagnetische Aktivität und Weltraumwettereignisse haben ebenfalls einen Einfluss auf diese Region. Daher bietet sich numerische Modellierung als Möglichkeit für die Interpretation der physikalischen Prozesse an.

Zur Klärung der offenen Fragen wurde in dieser Arbeit ein globales, dreidimensionales, zeitabhängiges physikalisches Modell verwendet und eine umfangreiche Studie der ionosphärischen Reaktion auf Veränderungen der Sonnenstrahlungen während der 27-Tage-Sonnenrotation wurde durchgeführt. Hierfür wurden Messdaten von Satellitenmissionen mit den Modellsimulationen verglichen. Im Mittel ergibt sich eine Verzögerung von 16 Stunden aus der Analyse der Messdaten und eine Verzögerung von 17 Stunden aus den Modellsimulationen. Die Studie bestätigt demnach die Fähigkeit des Modells, die verzögerte ionosphärische Reaktion in stündlicher und täglicher Auflösung zu simulieren. Diese Ergebnisse stimmen gut mit vorangegangenen Studien überein.

Im Rahmen dieser Arbeit wurden zum ersten Mal Simulationen zum Einfluss der Eddy-Diffusion durchgeführt. Diese Analyse zeigt, dass die Eddy-Diffusion ein wichtiger Faktor für die Ausprägung der ionosphärischen Verzögerung ist und dass der Einfluss von Prozessen der unteren Atmosphäre eine entscheidende Rolle spielt. Es wurde festgestellt, dass die Eddy-Diffusion eine erhebliche Veränderung der thermosphärischen Zusammensetzung verursacht, was wiederum zu Veränderung der Menge des atomaren Sauerstoffs führt. Dies beeinflusst dann die Ionisations- und Verlustrate. Da der atomare Sauerstoff erheblich zur Ionisierung beiträgt. Zunehmender Eddy-Diffusion folgen damit auch verkleinert der atomarer Sauerstoff Ionendichte und TEC. Daher nimmt TEC mit zunehmender Eddy-Diffusion ab und auch die Verzögerung wird kleiner. Andersherum führt ein langsamer Transport zu einem Maximum der ionosphärischen Verzögerung.

Diese Dissertation gibt eine umfangreiche Zusammenfassung für das Verständnis der ionosphärischen Verzögerung zu Variationen der solaren EUV-Strahlung. Dafür werden

TEC-Messungen mit numerischen Simulationen kombiniert. Weiterhin werden durch Vergleich die besten solaren Proxys für die Beschreibung der solaren Aktivität in T-I-Modellen bestimmt. Dies ist von entscheidender Bedeutung, um den Fokus auf die Verbesserung dieser Modelle zu lenken.

Bibliographic Description

Vaishnav, Rajesh Ishwardas

Delayed Ionospheric Response to Solar EUV/UV Radiation Variations

Universität Leipzig, Dissertation

103 pp., 191 bibl., 55 fig.

Abstract

The variability of the thermosphere-ionosphere (T-I) system and its complex behavior is strongly dependent on the continuously changing solar extreme ultraviolet (EUV) and ultraviolet (UV) radiation. The ionospheric electron density (or ion density) is mainly controlled by photoionization, loss by recombination, and transport processes. Transport processes play a significant role in the T-I composition and are responsible for the plasma distribution.

The ionospheric response to solar activity has been investigated using total electron content (TEC) and solar EUV observations, as well as various solar proxies. An ionospheric delay of about 1-2 days in the daily TEC on the time scale of 27 days solar rotation period has been reported. It has also been shown that the He-II index is one of the best solar proxies to represent the solar activity at different time scales.

The ionospheric delay in relation to solar radiation variations has attracted less attention in the past, especially with respect to its possible mechanisms. However, such studies, are of great importance for a better understanding of the complex interactions between solar radiation and the ionosphere that affect radio communications and navigation systems such as GNSS. Since the T-I region is affected not only by solar radiation, but also by lower atmospheric forcings, geomagnetic activity, and space weather events. Therefore, numerical modeling provides an opportunity to interpret the possible physical mechanism.

To shed more light on this issue, a global, 3-D, time-dependent, physics-based numerical model was used in this thesis. It is a comprehensive numerical study to investigate the ionospheric response to solar flux changes during the 27 days solar rotation period. Satellite observations were used for comparison with the model simulations. The average delay for the observed (modeled) TEC is about 17 (16) h against high-resolution solar EUV flux. The study confirms the capabilities of the model to reproduce the delayed ionospheric response with daily and hourly resolution. These results are in close agreement with previous studies.

For the first time, the model simulations were performed to understand the role of eddy diffusion. The study shows that eddy diffusion is an important factor affecting the ionospheric delay and highlights the influence of the lower atmospheric forcing. Eddy diffusion was found to cause a change in thermospheric composition, which induces changes in atomic oxygen by modifying loss and photoionization rates. Atomic oxygen contributes significantly to ionization. Enhanced eddy diffusion leads to a decrease in atomic oxygen ion density and consequently TEC. Therefore, TEC decreases due to enhanced eddy diffusion, showing that the ionospheric delay is reduced. Thus, slow transport leads to maximum ionospheric delay.

This dissertation provides a comprehensive understanding of the ionospheric response to varying EUV by combining TEC observations and numerical modeling aspects. Detailed comparisons have found the best solar proxies for representing solar activity in T-I models and help to focus attention on improving these models.

Contents

Acronyms

CDDIS	Crustal Dynamics Data Information System
CHAMP	CHAllenging Minisatellite Payload
CTIPe	Coupled Thermosphere Ionosphere Plasmasphere electrodynamics
CWT	Continuous Wavelet Transform
EOF	Empirical Orthogonal Function
EUV	Extreme Ultraviolet
EUVAC	EUV flux model for Aeronomic Calculations
EVE	EUV Variability Experiment
GAIA	Ground-to-topside model of Atmosphere and Ionosphere for Aeronomy
GCM	General Circulation Model
GIM	Global Ionosphere Maps
GITM	Global Ionosphere Thermosphere Model
GNSS	Global Navigation Satellite Systems
GOES	Geostationary Operational Environmental Satellite
GPS	Global Positioning System
GRACE	Gravity Recovery and Climate Experiment
GTEC	Global mean Total Electron Content
IGS	International GNSS Service
ISS	International Space Station

LISIRD	LASP Interactive Solar IRradiance Datacenter
LSP	Lomb–Scargle periodogram
MLT	Mesosphere-Lower Thermosphere
MODWT	Maximal Overlap Discrete Wavelet Transform
NCAR	National Aeronautics and Space Administration
NCAR	National Center for Atmospheric Research
NH	Northern Hemisphere
NOAA	National Oceanic and Atmospheric Administration
PC	Principal Component
SC	Solar Cycle
SDO	Solar Dynamics Observatory
SEE	Solar EUV Experiment
SH	Southern Hemisphere
SOHO	SOlar Heliospheric Observatory
SOLID	SOLar Irradiance Data Exploitation
SSA	Sunspot Area
SSN	Sunspot Number
SolACES	Solar Auto-Calibrating EUV/UV Spectrophotometers
T-I	Thermosphere-Ionosphere
TEC	Total Electron Content
TIE-GCM	Thermosphere–Ionosphere Electrodynamics General Circulation Model

TIMED	Thermosphere Ionosphere Mesosphere Energetics and Dynamics
TIROS	Television Infrared Observation Satellite
UV	Ultraviolet
WACCM-X	Whole Atmosphere Community Climate Model with thermosphere and ionosphere extension
WAM	Whole Atmosphere Model

1 General introduction

1.1. Introduction: Ionospheric delayed response

Solar activity plays a significant role in controlling variations in the thermosphere-ionosphere (T-I) system, especially by extreme ultraviolet (EUV) and ultraviolet (UV) radiation and their variability. The ionospheric E and F regions are important layers of the Earth's atmosphere (above $\approx$90 km) formed by the ionization of various species such as nitrogen, atomic oxygen, and molecular oxygen.

The response of the ionospheric plasma to solar EUV and UV variations has been extensively studied by ground- and space-based observations, as well as by numerical and empirical modeling. These studies have shown that the ionospheric response to solar EUV radiation variations is delayed by 1-2 days (hereafter; the days is denoted by d and the hours by h) at the time scale of the solar rotation period of 27 d (e.g. Jakowski et al., 1991; Afraimovich et al., 2008; Min et al., 2009; Lee et al., 2012; Jacobi et al., 2016). However, a comprehensive analysis of the ionospheric delay and its physical mechanism that puts this debate in perspective is largely lacking.

EUV radiation is not emitted at constant rates and varies on different time scales, including short-term variability (minutes (flares), daily, 27 d Carrington rotation, and seasonal) and long-term variability (11 years solar cycle). Since direct EUV measurements were not available before the space age due to atmospheric absorption, solar proxies were often used to represent solar variability. The most commonly used proxies for ionospheric applications are the F10.7 index, the Mg II index, and the sunspot number, which are available at daily resolution. All proxies do not always perfectly describe solar activity (Dudok de Wit et al., 2009), and their ability to represent the EUV depends on the wavelength and time scale. However, a comprehensive analysis of these solar proxies is needed to investigate the best proxy for representing solar activity through a long-term analysis

of the ionospheric delay on different time scales with multiple solar proxies.

To understand the variability of the T-I system and accurately estimate the ionospheric delay, analysis with higher resolution data sets is also essential. Understanding and realistically estimating solar irradiance has long been an open issue, but recently EUV datasets (either direct measurements, composite datasets, or models) have improved significantly (e.g. Haberreiter et al., 2017). However, continuous time series of the solar EUV spectrum itself have been available since the launch of the NASA Thermosphere Ionosphere Mesosphere Energetics and Dynamics (TIMED) satellite mission in 2001 (Woods et al., 2005). Furthermore, the Solar Dynamics Observatory (SDO) EUV Variability Experiment (EVE) provides a continuous high-resolution spectrum (Woods et al., 2010). Recently, the ionospheric delay has been accurately estimated using high-resolution datasets and is about 17-19 h (e.g. Schmölter et al., 2018; Schmölter et al., 2020). Therefore, a comprehensive analysis of the ionospheric delay at higher resolution using observations and modeling is now possible.

The ionospheric delay is basically known by an imbalance of production and loss of electrons or ions in the T-I region. The first attempt was made by Jakowski et al. (1991) to investigate the physical mechanism of the thermospheric response to solar radiation. To understand the underlying mechanisms of the delay of about 1-2 d observed in the ionospheric plasma, they used a one-dimensional numerical model between 100 and 250 km altitude with simplifying assumptions such as a fixed temperature profile, restriction to O and O_2 constituents of the thermosphere, and a fixed downward flow of atomic oxygen at the lower boundary. They proposed that the delayed density fluctuation of atomic oxygen at 180 km altitude is about 2 d, which is due to O_2 photodissociation and transport. To investigate mechanisms of ionospheric delay, this thesis seeks to contribute to the understanding of the delayed ionospheric response to solar EUV and UV radiation variations using the global first-principles nonlinear time-dependent 3D physics-based numerical model Coupled Thermosphere Ionosphere Plasmasphere electrodynamics (CTIPe)

(Fuller-Rowell and Rees, 1980). Using CTIPe model simulations, this dissertation identifies the specific role of eddy diffusion. In doing so, the delayed ionospheric response is linked to the neutral compositions based on the production and loss of electrons and ions. The analysis provides an understanding of the major challenges related to the ionospheric delay using GNSS observations and numerical modeling to understand the complex interaction between the I-T system and solar EUV radiation variations. This thesis consists of four self-contained research articles with corresponding literature reviews. The rest of the introduction describes the objectives and provides an overview of the research conducted.

1.2. Objectives and structure of the thesis

The main objective of this research is to investigate the delayed response of the ionosphere to solar EUV and UV radiation variations on different time scales, specifically in the 27 d solar rotation period and 11 years solar cycle. In addition, extensive modeling is presented to understand the physical mechanism of the ionospheric delay and to validate the hypothesis put forward by Jakowski et al. (1991).

To approach the overall research objective, four objectives were selected:

The first paper focuses on the preliminary investigation of the ionospheric response to solar EUV variations using observed TEC, provided by the International GNSS Service (IGS), F10.7 index and TIMED SEE flux at daily resolution from January 2003 to December 2016. Wavelet coherence and cross-wavelet methods were used to derive the periodicities in GTEC and solar proxies. Preliminary results of a CTIPe model experiment to estimate the delay at the solar rotation time scale will also be presented.

The analysis carried out in the second paper mainly aims to investigate and evaluate the correlation between the TEC provided by the IGS and several solar EUV proxies (F10.7, F1.8, F3.2, F8, F15, F30, He II, Mg II index, Ly-α, Ca II K, daily sunspot area

(SSA) and sunspot number (SSN)) during the period from January 1999 to December 2017. The purpose of using multiple proxies is to estimate the respective correlation and ionospheric lag to identify proxies that are best suited to describe the solar-ionospheric relationship at different time scales and under different solar activities. Therefore, the ionospheric delay at the different oscillation periods of solar irradiance is addressed to investigate the response of the global mean TEC (GTEC) to solar variations as indicated by different solar proxies. To understand the variability in the ionosphere, we use the method of empirical orthogonal functions (EOFs) to classify the temporal and spatial variability in the ionosphere.

The analysis performed in the third paper mainly focuses on investigating the more precise estimation of the delayed ionospheric response to the EUV flux measured by the Solar Dynamics Observatory (SDO) EUV Variability Experiment (EVE) and its trend during 2011-2013 using the CTIPe model simulations and satellite observations with hourly resolution. In addition, relationships with solar irradiance and delayed response are presented over both the Northern and Southern Hemispheres. Here we analyze the delayed response at 15°E, covering latitudes from 70°S to 70°N, and compare the response over the South African region with the European region.

The fourth paper addresses the important role of eddy diffusion processes, which can affect the ionospheric delay by several hours, using CTIPe model simulations. In this work, our goal is to validate the hypothesis put forward by Jakowski et al. (1991) and explain the physical mechanisms of the ionospheric delay. To understand the role of T/I coupling in this study, we perform model runs that modify eddy diffusion. Therefore, in this work we focus on reproducing and investigating the ionospheric delay response and its physical mechanism over a European site (40°N).

Following the fourth paper, a concluding chapter discusses the findings based on the CTIPe modeling to validate the hypothesis provided by Jakowski et al. (1991), challenges

and shortcomings of this paper in a broader perspective. Moreover, further research is needed to understand the ionospheric delay under different atmospheric conditions and for developing the weather prediction models.

1.3.   Model description and data

1.3.1.   CTIPe model description

The CTIPe model is an advanced version of the CTIM model (Fuller-Rowell et al., 1987) and is a global, first principle, non-linear, time-dependent, 3-D, numerical, physics-based coupled thermosphere-ionosphere-plasmasphere model consisting of four fully coupled distinct components, namely, (a) a neutral thermosphere model (Fuller-Rowell and Rees, 1980), (b) a high-latitude ionosphere convection model (Quegan et al., 1982), (c) a mid- and low-latitude ionosphere plasmasphere model (Millward et al., 1996), and (d) an electrodynamics model (Richmond et al., 1992). The thermosphere component of the CTIPe model solves the continuity, momentum, and energy equations to calculate the wind components, global temperature, and composition.

The transport terms particularly specify the $E \times B$ drift and include ion-neutral interactions under the effect of the magnetospheric electric field. The geographic latitude/longitude resolution is $2°/18°$. In the vertical direction, the atmosphere is divided into 15 logarithmic pressure levels at an interval of one scale height, starting with a lower boundary at 1 Pa (about 80 km altitude) to above 500 km altitude at pressure level 15. The high-latitude ionosphere (poleward of geomagnetic coordinates $55°$ N/S) and the mid- and low-latitude ionosphere and plasmasphere are implemented as separate components, and there is an artificial boundary between these two model components. The equations for the neutral thermosphere model are solved self-consistently with a high-latitude iono-

sphere model (Quegan et al., 1982). The numerical solution of the composition equation describes transport, turbulence, and diffusion of atomic oxygen, molecular oxygen, and nitrogen (Fuller-Rowell and Rees, 1983). External inputs are needed to run the model, such as solar UV and EUV, Weimer electric field, TIROS/NOAA auroral precipitation, and tidal forcing from the Whole Atmosphere Model (WAM). The F10.7 index (Tapping, 1987) is used as a solar proxy for calculating ionization, heating, and oxygen dissociation processes. Within CTIPe, a reference solar spectrum based on the EUVAC model (Richards et al., 1994) and the Woods and Rottman (2002) model, driven by variations of input F10.7 is used. The EUVAC model is used for the wavelength range from 5 to 105 nm, and the Woods and Rottman (2002) model from 105 nm to 175 nm. Solar flux is obtained from the reference spectra using the following equation:

$$f(\lambda) = f_{ref}(\lambda)[1 + A(\lambda)(P - 80)] \tag{1.1}$$

where f_{ref} and A are the reference spectrum and a solar variability factor, and $P = 0.5 \times (F10.7 + F10.7A)$, where F10.7A is the average of F10.7 over 41 days. Detailed information on the CTIPe model is available in Fuller-Rowell (1984); Codrescu et al. (2008, 2012).

1.3.2.   Data

In this section, the used observational data is described such as TEC, solar proxies and geomagnetic indices. Global TEC maps are available from the International Global Navigation Satellite Systems (GNSS) Service (IGS, (Hernández-Pajares et al., 2009)). We used NASA's 1-hourly global TEC maps, which are available in IONEX format from the CDDIS data archive service (Noll, 2010) and have provided global coverage since 1998. These maps are available at a spatial resolution of 2.5° in latitude and 5° in longitude. The accuracy of the IGS TEC maps is reported to be 2-8 TECU (Chen et al., 2020).

Several solar proxies are available, often used in previous studies to represent the level of solar activity compared to ionospheric parameters before the space age, and due to the unavailability of direct solar EUV measurements. However, continuous time series of the solar EUV spectrum itself have been available since the launch of the NASA TIMED satellite mission in 2001. Measurements of solar irradiance by the TIMED SEE instrument have been available since January 22, 2002 (Woods et al., 2005). The SEE instrument is designed to measure soft X-ray and EUV radiation from 0.1 to 194 nm with a resolution and accuracy of 0.1 nm and about 10-20 %. SEE includes two instruments, the EUV grating spectrograph and the XUV photometer system (Woods et al., 2000). Here we use daily values of solar irradiance integrated from 1 to 105 nm wavelength. In addition, the SDO EVE provides a continuous high-resolution spectrum with a wavelength range from 0.1 to 120 nm, a spectral resolution of 0.1 nm, and a temporal resolution of 20 s. (Woods et al., 2010; Pesnell et al., 2011).

Furthermore, several solar proxies used in this work, namely the F10.7 index, the Bremen composite Mg II index (IUP, 2018), the Ca II K index, the daily sunspot area (SSA), the He II (Dudok de Wit, 2011) and the F1.8, F3.2, F8, F15, and F30 solar radio flux emission at five wavelengths (Dudok de Wit et al., 2014; Haberreiter et al., 2017), as well as Ly-α and sunspot number available from NASA's Goddard Space Flight Center via the OMNIWeb Plus database. The F10.7 index data were taken from the LISIRD (Dewolfe et al., 2010) database, while F1.8, F3.2, F8, F15, F30, Ca II K index and daily SSA proxies are available from the SOLID database (http://projects.pmodwrc.ch/solid/, (Schöll et al., 2016; Haberreiter et al., 2017)). SOLID data were only available for the time interval 1999-2012, all other data cover the entire period from 1999 to 2017. We also used daily Kp, Dst, and Ap indices taken from the OMNIWeb Plus database to investigate the relationship between GTEC and geomagnetic activity.

2 Paper 1: Ionospheric delayed response: preliminary results

In this chapter, we present the preliminary results of the delayed response of the ionosphere to solar EUV variations, using different proxies based on solar EUV spectra observed by the SEE on board the TIMED satellite, the F10.7 index and the Bremen composite Mg-II index during the period from January 2003 to December 2016. The main objective is to calculate the cross-correlation and ionospheric delay between the ionospheric TEC and solar EUV parameters. Wavelet coherence and cross-wavelet methods were used to derive the periodicities in GTEC and solar proxies. Preliminary results of a CTIPe model experiment to estimate the delay on the solar rotation time scale are also presented.

Our main contributions to scientific understanding of ionospheric delay:

- In this study, the strong correlation between GTEC and solar proxies (SEE-EUV integrated flux and the Mg II index) was observed at the 27 d solar rotation period, while F10.7 is less correlated with GTEC.

- We observed an ionospheric delay at the 27 d solar rotation period with the time scale of 1-2 d between GTEC and all solar proxies considered, confirming previous results in the literature.

- The model qualitatively reproduces the observed ionospheric delay of about 1-2 d in GTEC with respect to the F10.7 index.

- Transport processes could play an important role in the delay.

This analysis is subject to a few limitations. In this paper daily resolution datasets were used to calculate the cross-correlation and lag. Second, the CTIPe model was run for 27 d and the input index F10.7 was artificially varied while keeping all other conditions constant. This work shows that the CTIPe model is capable of reproducing

the ionospheric delay with daily resolution. Therefore, the work motivates future research to understand the physical mechanism of ionospheric delay.

This paper, **Vaishnav et al., (2018)** advocates model capabilities to reproduce ionospheric delay and the possible mechanism of ionospheric delay in TEC.

Research paper

Vaishnav et al., (2018): Vaishnav, R., Jacobi, C., Berdermann, J., Schmölter, E., and Codrescu, M. (2018). Ionospheric response to solar EUV variations: Preliminary results, Advances in Radio Science, 16, 157–165, https://doi.org/10.5194/ars-16-157-2018.

Author contributions statement

The doctoral student performed the following tasks independently for this paper: Conceptualizing the approach, analyzing the data, compiling and creating graphs, perform CTIPe model run, interpretation and conclusion, and writing the first draft of the paper.

Advances in
Radio Science
Open Access Proceedings

Ionospheric response to solar EUV variations: Preliminary results

Rajesh Vaishnav[1], **Christoph Jacobi**[1], **Jens Berdermann**[2], **Erik Schmölter**[2], **and Mihail Codrescu**[3]

[1]Leipzig Institute for Meteorology, Universität Leipzig, Stephanstr. 3, 04103 Leipzig, Germany
[2]German Aerospace Center, Kalkhorstweg 53, 17235 Neustrelitz, Germany
[3]Space Weather Prediction Centre, National Oceanic and Atmospheric Administration, Boulder, Colorado, USA

Correspondence: Rajesh Vaishnav (rajesh_ishwardas.vaishnav@uni-leipzig.de)

Abstract. We investigate the ionospheric response to solar Extreme Ultraviolet (EUV) variations using different proxies, based on solar EUV spectra observed from the Solar Extreme Ultraviolet Experiment (SEE) onboard the Thermosphere Ionosphere Mesosphere Energetics and Dynamics (TIMED) satellite, the F10.7 index (solar irradiance at 10.7 cm), and the Bremen composite Mg-II index during January 2003 to December 2016. The daily mean solar proxies are compared with global mean Total Electron Content (GTEC) values calculated from global IGS TEC maps. The preliminary analysis shows a significant correlation between GTEC and both the integrated flux from SEE and the Mg II index, while F10.7 correlates less strongly with GTEC. The correlations of EUV proxies and GTEC at different time periods are presented. An ionospheric delay in GTEC is observed at the 27 days solar rotation period with the time scale of about ∼ 1–2 days. An experiment with the physics based global 3-D Coupled Thermosphere/Ionosphere Plasmasphere electrodynamics (CTIPe) numerical model was performed to reproduce the ionospheric delay. Model simulations were performed for different values of the F10.7 index while keeping all the other model inputs constant. Preliminary results qualitatively reproduce the observed ∼ 1–2 days delay in GTEC, which is might be due to vertical transport processes.

1 Introduction

The ionospheric E and F regions are important layers of the Earth's atmosphere (above ∼ 60 km), which are created due to ionization of various species like nitrogen, atomic oxygen, and molecular oxygen. The ionosphere is built through absorbing solar extreme ultraviolet (EUV) radiation and soft X-rays mainly at wavelengths below 105 nm. The EUV radiation is not emitted at constant rates and varies at different timescales, including short-term variability (minutes (flares), daily, 27 days Carrington rotation, and seasonal) and long term variability (11 years solar cycle). The long term variability is expected to be greater than the short term variability (Woods and Rottman, 2002). For instance, the He II EUV emission line can change by a factor of 2 during the 11 years solar cycle and ∼ 50 % during the 27 days rotation period, and the variation in EUV can be 30 % at ∼ 100 nm and 100 % at ∼ 10 nm during the solar rotation period (e.g. Lean et al., 2001, 2011). During solar flares, the X-rays and the solar EUV regions may be enhanced by more than a factor of 50 and less than a factor of 2, respectively (Woods and Eparvier, 2006). Short-term solar variability is part of space weather, so that ionospheric parameters like the Total Electron Content (TEC) and the ionospheric height (McNamara and Smith, 1982) are influenced by space weather. TEC is the vertically integrated electron density of the ionosphere which is usually given in TEC units (1 TECU = 10^{16} electrons m^{-2}). The ionospheric variability due to changes in solar activity has been studied extensively by various researchers (e.g., Jakowski et al., 1991; Rishbeth, 1993; Su et al., 1999; Forbes et al., 2000; Liu et al., 2006; Afraimovich et al., 2008; Lee et al., 2012; Jacobi et al., 2016, and references therein). Such studies are of great importance for improving our understanding of the solar influence on radio communication and navigation systems like Global Navigation Satellite Systems (GNSS). Radio waves are refracted by the ionosphere, which in turn is affected by the solar activity.

Due to unavailability of direct EUV measurements before the space age, the variation in TEC is frequently compared against solar proxies, with the most common

one being the F10.7 index, which is the irradiance at a wavelength of 10.7 cm, usually given in solar flux units (sfu, 10^{-22} W m^{-2} Hz^{-1}) (Tapping, 1987; Rishbeth, 1993; Maruyama, 2010). Other indices are the Bremen composite MG-II index (the core to wing ratio of the MG-II line) (Maruyama, 2010), or EUV-TEC which have been introduced by Unglaub et al. (2011) to name only a few. The long-term and short-term relation between EUV and different solar proxies (F10.7 index, Mg-II index, Sunspot number) has been reported in previous studies (Dudok de Wit et al., 2009; Chen et al., 2012; Wintoft, 2011). In comparison to the short term variability, the long-term variations of EUV radiation are better represented by the solar proxies (Chen et al., 2012). All the proxies not always perfectly describe the solar activity (Dudok de Wit et al., 2009), and their capability in reproducing EUV depends on wavelength and time scale. Chen et al. (2011) suggested that the F10.7 index is not able to produce the solar activity level during the minima of solar cycle 23, and Chen et al. (2012) showed that the MG-II index is a better representative of SOHO EUV in the wavelength range 26–34 nm than the F10.7 index. On the other hand, good correlation has been observed between ionospheric parameters and F10.7 index during Autumn–Winter of the years 2003 to 2005 (Oinats et al., 2008).

In recent years, direct solar EUV flux measurements are available from various satellites such as the Solar EUV Experiment (SEE) onboard the Thermosphere Ionosphere Mesosphere Energetics and Dynamics (TIMED) satellite (Woods et al., 2000, 2005), and the Extreme Ultraviolet Variability Experiment (EVE) onboard the Solar Dynamics Observatory (SDO) (Woods et al., 2012; Pesnell et al., 2012). However, due to degradation of EUV measuring instruments solar proxies may be more suitable (BenMoussa et al., 2013), or repeated calibration is necessary. The availability of the direct EUV measurements provide an opportunity for comparing EUV with different solar proxies (e.g., Jacobi et al., 2016).

Various researchers had observed a delayed response of ∼ 1–2 days in TEC or global mean TEC (GTEC) with respect to solar activity changes (e.g. Jakowski et al., 1991; Oinats et al., 2008; Afraimovich et al., 2008; Min et al., 2009; Lee et al., 2012; Jacobi et al., 2016). Hocke (2008) showed the 11 years, 1 year, and 27 days oscillations of GTEC and the Mg-II index with a high correlation coefficient. Lee et al. (2012) studied the correlation and time lag at the 27 days solar rotation period using GPS TEC and in situ electron density measurements from the CHAMP and GRACE satellites. They found a 1-day difference of the time delay in the northern and southern hemisphere. Jakowski et al. (1991) used a 1-D numerical model to explain the delay of ∼ 1–2 days. The study concluded that the delay might be due to slow diffusion of atomic oxygen at 180 km, which was produced due to dissociation of molecular oxygen in the lower altitude.

In recent years numerical, empirical, and physics-based thermosphere/ionosphere models have been developed to characterize ionospheric dynamics. Among them are the Coupled Thermosphere Ionosphere Plasmasphere Electrodynamics (CTIPe, Fuller-Rowell and Rees, 1983; Millward et al., 2001; Codrescu et al., 2012), the International Reference Ionosphere (IRI, Rawer et al., 1978; Bilitza et al., 2011) and Thermosphere-Ionosphere-Electrodynamics General Circulation Model (TIE-GCM, Roble et al., 1988). These models play an important role in upper atmospheric studies (e.g., Negrea et al., 2012; Fedrizzi et al., 2012). To simulate solar variability, models are frequently driven by proxies like F10.7 index or the Mg-II index. The F10.7 index is the most widely used index in upper atmosphere research to represent the solar variability due to the availability of continuous measurements since 1947 (Woods et al., 2005). The solar EUV variability can be better represented by the improved F10.7 index using 81 days running mean (e.g., Viereck et al., 2001; Liu et al., 2006). The CTIPe model uses a modified F10.7 index, which is the average of the previous day value of the F10.7 index and the average of the previous 41 days (Codrescu et al., 2012). Fitzmaurice et al. (2017) used the CTIPe model to understand the influence of solar activity on the ionosphere/thermosphere during the geomagnetic storm. They reported that solar activity has the greatest effect on model simulated TEC.

The main aim of the present study is to find out the correlation and time delay between GTEC and solar proxies based on data from January 2003 to December 2016. To derive the periodicities in GTEC and solar proxies, the wavelet coherence and cross-wavelet method have been utilized. Preliminary results of a CTIPe model experiment to estimate the delay at the solar rotation time scale will also be presented.

2 Data and model description

2.1 Data sources

In this work, we use daily global TEC maps from the International GNSS Service (IGS, Hernandez-Pajares et al., 2009) provided by NASA's CDDIS (Noll, 2010) data archive service (CDDIS, 2017). Gridded global TEC data is available at a time resolution of 2 h and on a spatial grid of 2.5° × 5° in latitude-longitude. For the analysis of the correlation between solar proxies and GTEC, we have selected three commonly used solar proxies, namely daily values of the F10.7 index, the Bremen composite Mg-II index, and the integrated EUV flux from the TIMED/SEE satellite. The F10.7 index and TIMED/SEE measurements are taken from the LISIRD (DeWolfe et al., 2010) database. The NASA TIMED satellite was launched in 2001 and carried four instruments (GUVI, SABER, SEE and TIDI). Solar irradiance measurements from the TIMED/SEE instrument are available since 22 January 2002 (Woods et al., 2005). The SEE instrument is designed to measure the soft X-rays and EUV radiation from 0.1 to 194 nm with the resolution and accuracy of 0.1 nm and

~ 10–20%, respectively. SEE includes two instruments, the EUV grating spectrograph and the XUV photometer system (Woods et al., 2000). We have used the daily integrated value of solar irradiance from 5.5 to 105.5 nm wavelength.

2.2 CTIPe model description

The CTIPe model is a global, 3-D, time-dependent, physics-based numerical model. It consists of four components, namely (a) a neutral thermosphere model (Fuller-Rowell and Rees, 1980), (b) a mid- and high-latitude ionosphere convection model (Quegan et al., 1982), (c) a plasmasphere and low latitude ionosphere model (Millward et al., 1996), and (d) an electrodynamics model (Richmond et al., 1992), which run simultaneously and are fully coupled. The thermosphere model is solving the equation of momentum, continuity, and energy to calculate global temperature, density, wind components, and atmospheric neutral composition. The parameters calculated from the thermosphere code are used to calculate production, loss, and transport of plasma. The transport terms consider ExB drift and interactions of ionised and neutral particles under the influence of the magnetospheric electric field (Codrescu et al., 2012). In the high latitude model, the atomic ions of O^+ and H^+ are calculated by solving the momentum, energy, and continuity equations, and the model includes vertical diffusion, horizontal transport, ion-ion, and ion neutral processes in the height range of 100 to 10 000 km. The contribution from $N2^+$, $O2^+$, NO^+ and N^+ are additionally added below 400 km. The mid and low latitude ionosphere model is also calculating H^+, O^+ ions, and electrons as does the high latitude model. The numerical solution of the composition equation with the energy and momentum equations describe the transport, turbulence, and diffusion of atomic oxygen, molecular oxygen and nitrogen (Fuller-Rowell and Rees, 1983). The latitude/longitude resolution is $2°/18°$. In the vertical direction, the atmosphere is divided into 15 levels in logarithmic pressure starting from a lower boundary at 1 Pa to ~ 500 km altitude at an interval of one scale height. The corresponding geometric heights are variable depending on temperature and therefore on the solar and magnetic activity. External inputs are required to drive the model like solar UV and EUV, Weimer electric field, TIROS/NOAA auroral precipitation, and tidal forcing. The F10.7 index is used in an artificial manner as input solar proxy to calculate ionization, heating, and oxygen dissociation processes in the ionosphere. For the simulation, the Hinteregger et al. (1981) reference solar spectrum driven by variations of input F10.7 is used in the model. More description of CTIPe is available in Codrescu et al. (2008, 2012).

3 Results and discussion

3.1 Correlation between TEC and solar EUV proxies

To study the long-term variations in GTEC and EUV proxies, datasets from 2003 to 2016 have been used. Figure 1 shows the normalized time series of GTEC, SEE EUV flux, the F10.7 index, and the MG-II index. All data has been normalized by subtracting the mean and dividing by the respective standard deviation. The data represent the decreasing and increasing parts of solar cycle 23 and 24, respectively. As the solar radiation plays a major role in the electron production, the correlation of GTEC with solar EUV or EUV proxies must be significant and is also correlated at the 27 days solar rotation period. Figure 2 shows the cross correlation between GTEC and (a) TIMED/SEE integrated EUV flux (left panel), and (b) F10.7 index (right panel) from 1 January 2003 to 31 December 2016. Since we do not consider the seasonal cycle here, a low-pass filter with a cut off period of three months was applied to the data before.

Figure 2 shows a strong correlation between normalized GTEC and integrated EUV flux (black) with a maximum correlation coefficient of 0.90 and shows a weaker correlation with the F10.7 index (red) with a maximum correlation coefficient of 0.84. Also, we have analyzed the correlation between GTEC and Mg-II index which shows a good correlation with a correlation coefficient of 0.89 (figure not shown). Jacobi et al. (2016) analyzed GTEC and SDO/EVE integrated EUV flux data from 2011 to 2014 and they also found a good correlation of about 0.89. Unglaub et al. (2011, 2012) have shown that the GTEC is more strongly correlated with the EUV-TEC proxy than with the F10.7 index. Figure 2 shows a delay of ~ 1–2 days in GTEC with respect to both SEE flux and F10.7 index, which confirms earlier analyses e.g. by Jacobi et al. (2016).

3.2 Wavelet analysis

In order to investigate the oscillations in the time series of GTEC and all EUV proxies in more detail, the continuous wavelet transform (CWT) method has been applied. The cross wavelet transform is constructed using 2 CWTs, which shows common high energies of the two time series and relative phase (Grinsted et al., 2004). We have used a Morlet mother wavelet. Furthermore, the wavelet coherence method is used to calculate significant coherence using Monte Carlo methods (Grinsted et al., 2004). Wavelet coherence can be calculated using 2 CWTs which shows the local correlation between the time series. All data has been normalized by subtracting the mean and dividing by the respective standard deviation.

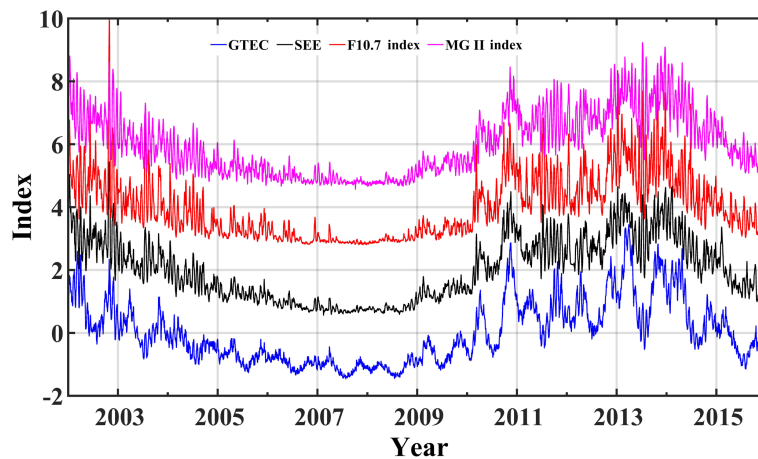The cross wavelet spectra between GTEC and both SEE–EUV flux and F10.7 index are shown in Fig. 3a and b, respectively.

Figure 1. Temporal variations of normalized datasets of GTEC (blue), SEE-EUV flux (black), F10.7 index (red), and Mg-II index (magenta) during year 2003 to 2016. The curves are vertically offset each by 2.
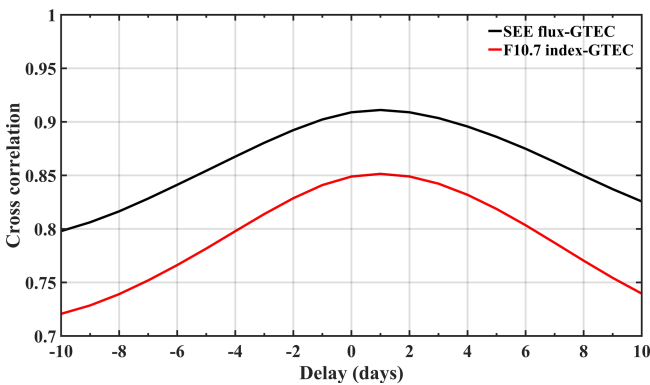

Figure 2. Cross-correlation of GTEC with SEE-EUV flux (black) and F10.7 index (red). Positive values denote GTEC lagging SEE-EUV or F10.7, respectively.

GTEC shows common high power with SEE-EUV flux and F10.7 at scales of 16–32 days during 2003 to 2005 and during 2009 to 2016. During those times when the coherence is significant, GTEC is in phase with SEE-EUV and F10.7. Much less power at the 27 days periodicity is observed from 2007 to 2009, which is the extended part of solar cycle 23.

The magnitude squared coherence of GTEC with SEE-EUV flux and the F10.7 index is shown in Fig. 3c and d, respectively. The coherence spectrum shows the time and period range where the two time series co-vary. As shown in both figures, a high correlation is observed at the 27 days periodicity. The magnitude squared coherence between GTEC and SEE flux is very high at 27 days periodicity, while GTEC and F10.7 behave less coherent. In comparison to the cross wavelet in Fig. 3a, b, wavelet coherence shows larger significant regions in Fig. 3c, d.

3.3 Variation in TEC using varying F10.7 values in CTIPe model

The CTIPe model has been used to simulate the ionospheric variability and to estimate the ionospheric delay due to solar variability. The model was run for 15 March 2013 conditions (Kp index = 3) and simulates TEC by varying the F10.7 index values in an artificial manner as input, keeping all the other input parameters constant. The input lower boundary in the CTIPe model is specified by the output of the Whole Atmospheric Model (WAM) (Akmaev, 2011). For the experiment, the model was first run for 30 days with constant input to reach a diurnally reproducible global temperature pattern, and then F10.7 was modified. Figure 4a shows the chosen F10.7 index values as input for the model, which vary from 80 to 120 sfu during one complete solar rotation period.

Figure 4b shows the zonal mean TEC simulated by the CTIPe model. The global TEC distribution qualitatively reproduces real ionospheric conditions, e.g. enhanced electron density near the equator due to the fountain effect (Appleton, 1946; Hanson and Moffett, 1966; Sterling et al., 1969). TEC varies according to the F10.7 index, but with a delay which can be seen by comparing the TEC maximum with the one of F10.7 in Fig. 4a. Figure 4c shows global mean values for the F10.7 index and the CTIPe TEC, both normalized by subtracting the mean and dividing by the respective standard deviation. A delay of about 1–2 days is observed. Figure 4d shows the cross-correlation and thus the delay between the input F10.7 index and TEC simulated by the CTIPe model. The delay introduced here may be due to vertical transport processes or slow diffusion of atomic oxygen, which has been suggested by Jakowski et al. (1991) as a possible process for the ionospheric delay. In order to understand the possible delay mechanism in the GTEC, the normalized modelled global mean atomic oxygen ion density (GAOID) is shown in Fig. 5 (upper row) for different
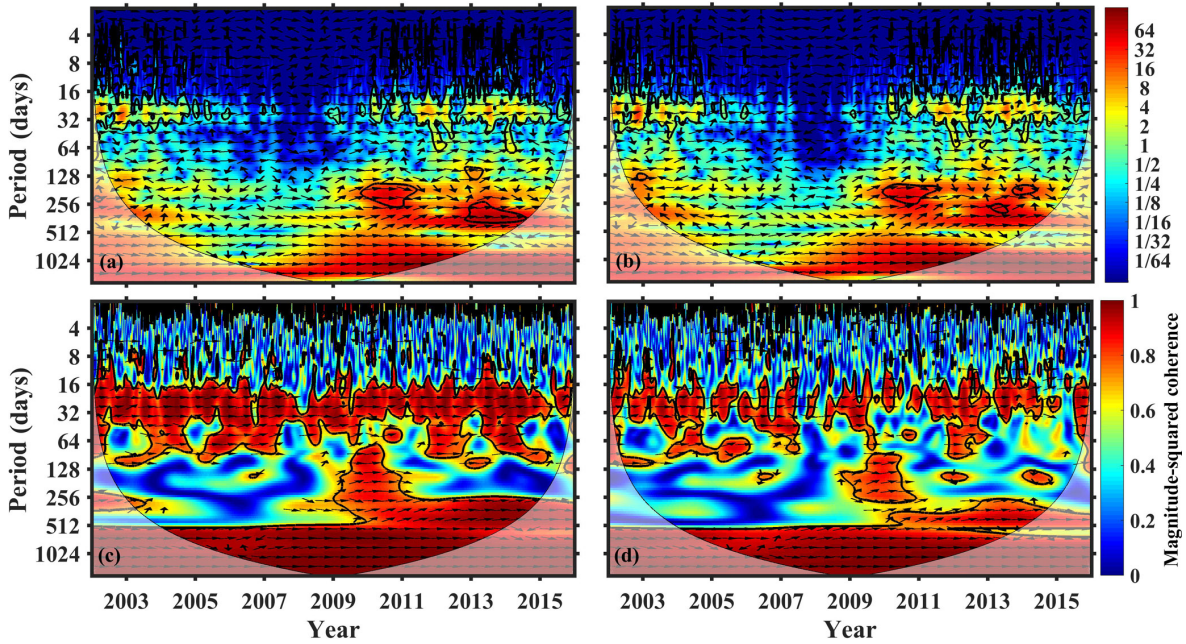
Figure 3. (a, b): cross-wavelet transform of the GTEC with **(a)** SEE-EUV flux and **(b)** F10.7 index. **(c, d)**: wavelet coherence of the GTEC with **(c)** SEE-EUV flux and **(d)** F10.7 index. The cone of influence is shown by a black line. Significant values are surrounded by a black line. The arrows show the phase relationship: in-phase pointing right, anti-phase pointing left, while downward direction means that GTEC is leading.
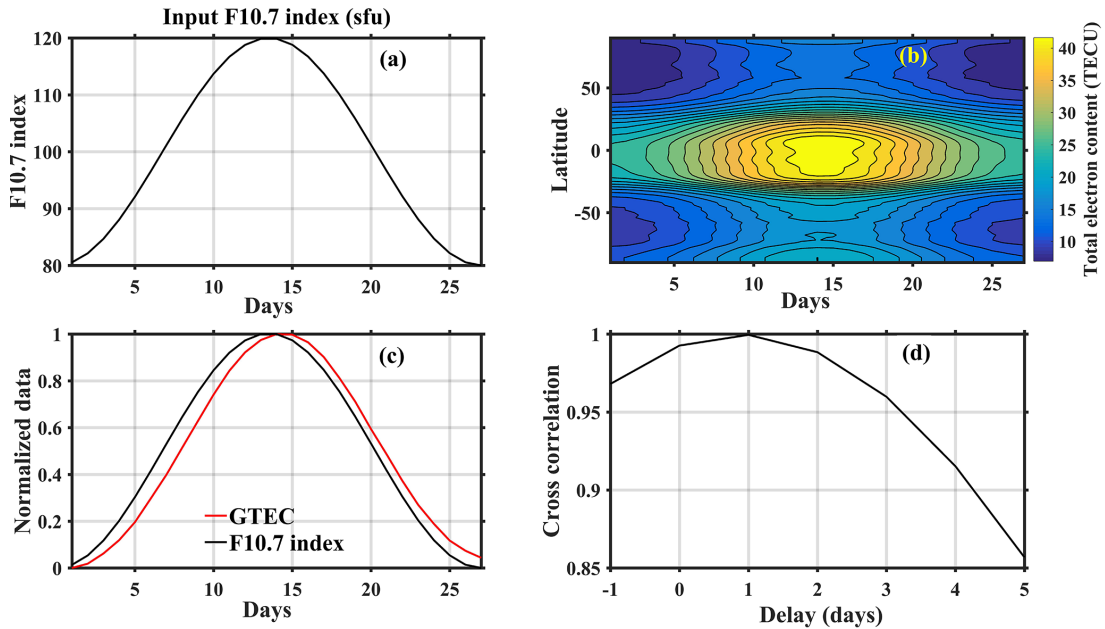

Figure 4. (a) input F10.7 index values for CTIPe model simulation, **(b)** simulated zonal mean TEC, **(c)** normalized data of F10.7 index and modelled GTEC, and **(d)** cross-correlation between F10.7 index and modelled GTEC.
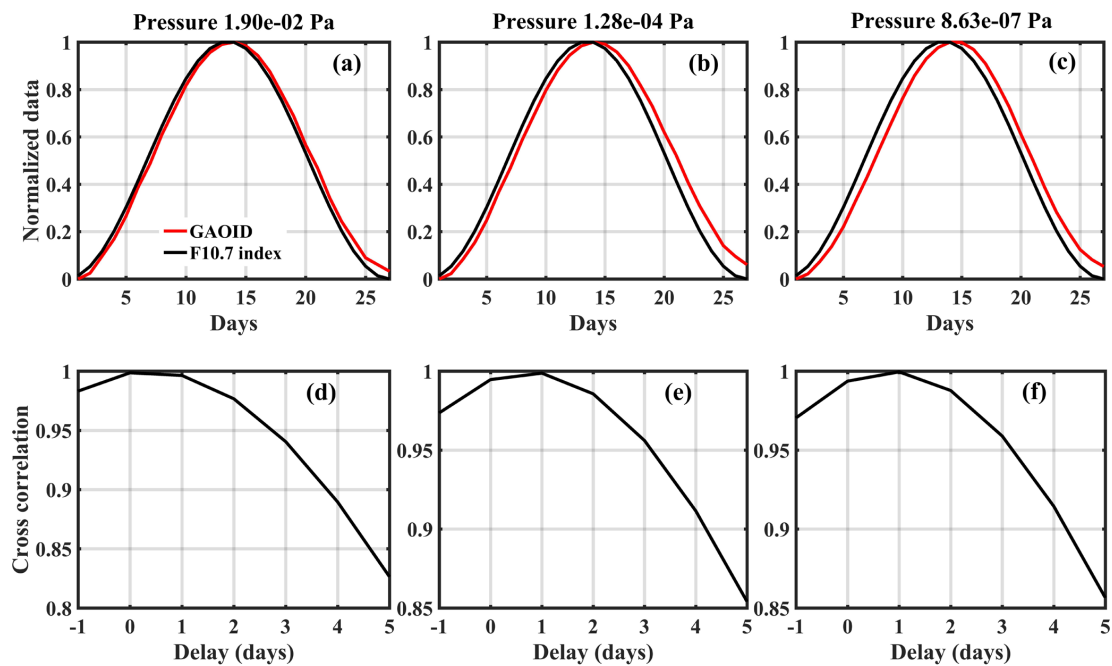
Figure 5. (a, b, c): Normalized modelled GAOID and input F10.7 data at three different pressure levels. **(d, e, f)**: Corresponding cross-correlations between F10.7 and modelled GAOID.

altitudes. The corresponding cross correlations between the F10.7 index and GAOID are shown in the lower panel. It is interesting to note that at pressure 1.9×10^{-2} Pascal in Fig. 5d there is only a small delay in GAOID with respect to F10.7, but Fig. 5b, e and c, f show a larger delay of ~ 1 day at greater altitudes. This preliminary analysis indicates that vertical transport processes might play a role in the delay.

4 Summary and Conclusions

To contribute to the understanding of the long-term ionospheric behaviour with respect to solar EUV variations we have analyzed data from 1 January 2003 to 31 December 2016. In this study, the strong correlation between GTEC and solar proxies has been observed at the 27 days solar rotation period. There is a particularly strong correlation between GTEC and integrated SEE-EUV flux and the Mg II index, while F10.7 correlates less strongly with TEC. We have also observed an ionospheric delay at the 27 days solar rotation period with the time scale of 1–2 days between GTEC and all the solar proxies considered, thereby confirming earlier results in the literature.

To gain more insight into the possible reasons for the delay, we have run the CTIPe model for 27 days and varied the input F10.7 index artificially while keeping all the other conditions constant. Preliminary results show that the model qualitatively reproduces the observed ionospheric delay of ~ 1–2 days in GTEC with respect to the F10.7 index. An attempt has been made to understand the delay process using

GAOID simulated by the CTIPe. The cross correlation analysis between the GAOID and the F10.7 indicates small delay at the lower pressure level and longer delay in higher pressure levels, which suggests that transport processes might play a role in the delay.

To conclude, in this first approach we have found that the CTIPe model is able to reproduce the observed ionospheric delay. The results, however, are only preliminary. In further studies with more realistic EUV changes, we will also analyse photodissociation and ionization processes of atomic oxygen, molecular oxygen, and molecular nitrogen in more detail to check the validity of the results by Jakowski et al. (1991). Furthermore, we will investigate the delay in the different ionospheric parameters on different timescales by varying various model components (dissociation, ionization) thereby investigating the physical processes responsible for the delay.

References

Afraimovich, E. L., Astafyeva, E. I., Oinats, A. V., Yasukevich, Yu. V., and Zhivetiev, I. V.: Global electron content: a new conception to track solar activity, Ann. Geophys., 26, 335–344, https://doi.org/10.5194/angeo-26-335-2008, 2008.

Akmaev, R. A.: Whole atmosphere modeling: Connecting terrestrial and space weather, Rev. Geophys., 49, RG4004, https://doi.org/10.1029/2011RG000364, 2011.

Appleton, E. V.: Two anomalies in the ionosphere, Nature, 157, 691, https://doi.org/10.1038/157691a0, 1946.

BenMoussa, A., Gissot, S., Schühle, U., Del Zanna, G., Auchère, F., Mekaoui, S., Jones, A. R., Walton, D., Eyles, C. J., Thuillier, G., Seaton, D., Dammasch, I. E., Cessateur, G., Meftah, M., Andretta, V., Berghmans, D., Bewsher, D., Bolsée, D., Bradley, L., Brown, D. S., Chamberlin, P. C., Dewitte, S., Didkovsky, L. V., Dominique, M., Eparvier, F. G., Foujols, T., Gillotay, D., Giordanengo, B., Halain, J. P., Hock, R. A., Irbah, A., Jeppesen, C., Judge, D. L., Kretzschmar, M., McMullin, D. R., Nicula, B., Schmutz, W., Ucker, G., Wieman, S., Woodraska, D., and Woods, T. N.: On-orbit degradation of solar instruments, Sol. Phys., 288, 389–434, https://doi.org/10.1007/s11207-013-0290-z, 2013.

Bilitza, D., McKinnell, L. A., Reinisch, B., and Fuller-Rowell, T.: The International Reference Ionosphere (IRI) today and in the future, J. Geodesy., 85, 909–920, https://doi.org/10.1007/s00190-010-0427-x, 2011.

CDDIS: GNSS Atmospheric Products, available at: http://cddis.nasa.gov/Data_and_Derived_Products/GNSS/atmospheric_products.html (last access: 29 June), 2017.

Chen, Y., Liu, L., and Wan, W.: Does the F10.7 index correctly describe solar EUV flux during the deep solar minimum of 2007–2009?, J. Geophys. Res., 116, A04304, https://doi.org/10.1029/2010JA016301, 2011.

Chen, Y., Liu, L., and Wan, W.: The discrepancy in solar EUV-proxy correlations on solar cycle and solar rotation timescales and its manifestation in the ionosphere, J. Geophys. Res., 117, A03313, https://doi.org/10.1029/2011JA017224, 2012.

Codrescu, M. V., Fuller-Rowell, T. J., Munteanu, V., Minter, C. F., and Millward, G. H.: Validation of the coupled thermosphere ionosphere plasmasphere electrodynamics model: CTIPe-Mass Spectrometer Incoherent Scatter temperature comparison, Adv. Space Res., 6, S09005, https://doi.org/10.1029/2007SW000364, 2008.

Codrescu, M. V., Negrea, C., Fedrizzi, M., Fuller-Rowell, T. J., Dobin, A., Jakowsky, N., Khalsa, H., Matsuo, T., and Maruyama, N.: A real-time run of the Coupled Thermosphere Ionosphere Plasmasphere Electrodynamics (CTIPe) model, Adv. Space Res., 10, S02001, https://doi.org/10.1029/2011SW000736, 2012.

DeWolfe, A. W., Wilson, A., Lindholm, D. M., Pankratz, C. K., Snow, M. A., and Woods, T. N.: Solar Irradiance Data Products at the LASP Interactive Solar Irradiance Datacenter (LISIRD), in: AGU Fall Meeting 2010, Abstract GC21B-0881, San Francisco, California, USA, 2010.

Dudok de Wit, T., Kretzschmar, M., Lilensten, J., and Woods, T.: Finding the best proxies for the solar UV irradiance, Geophys. Res. Lett., 36, L10107, https://doi.org/10.1029/2009GL037825, 2009.

Fedrizzi, M., Fuller-Rowell, T. J., and Codrescu, M. V.: Global Joule heating index derived from thermospheric density physics-based modeling and observations, Adv. Space Res., 10, S03001, https://doi.org/10.1029/2011SW000724, 2012.

Fitzmaurice, A., Kunznetsova, M., Shim, J. S., and Uritskey, V.: Impact of Solar Activity on the Ionosphere/Thermosphere during Geomagnetic Quiet Time for CTIPe and TIE-GCM, Arxiv, Physics eprint, arXiv:1701.06525, 2017.

Forbes, J. M., Palo, S. E., and Zhang, X.: Variability of the ionosphere, J. Atmos. Sol.-Terr. Phy., 62, 685–693, https://doi.org/10.1016/S1364-6826(00)00029-8, 2000.

Fuller-Rowell, T. J. and Rees, D.: A three-dimensional time-dependent global model of the thermosphere, J. Atmos. Sci., 37, 2545–2567, https://doi.org/10.1175/1520-0469(1980)037<2545:ATDTDG>2.0.CO;2, 1980.

Fuller-Rowell, T. J. and Rees, D.: Derivation of a conservation equation for mean molecular weight for a two-constituent gas within a three-dimensional, time-dependent model of the thermosphere, Planet. Space Sci., 31, 1209–1222, https://doi.org/10.1016/0032-0633(83)90112-5, 1983.

Grinsted, A., Moore, J. C., and Jevrejeva, S.: Application of the cross wavelet transform and wavelet coherence to geophysical time series, Nonlinear Proc. Geoph., 11, 561–566, https://doi.org/10.5194/npg-11-561-2004, 2004.

Hanson W. B. and Moffett, R. J.: Ionization transport effects in the equatorial F-region, J. Geophys. Res., 71, 5559–5572, https://doi.org/10.1029/JZ071i023p05559, 1966.

Hernandez-Pajares, M., Juan, J. M., Sanz, J., Orus, R., Garcia-Rigo, A., Feltens, J., Komjathy, A., Schaer, S. C., and Krankowski, A.: The IGS VTEC maps: a reliable source of ionospheric information since 1998, J. Geodyn., 83, 263–275, https://doi.org/10.1007/s00190-008-0266-1, 2009.

Hinteregger, H. E., Fukui, K., and Gilson, B. R.: Observational, reference and model data on solar EUV, from mea-

surements on AE-E, Geophys. Res. Lett., 8, 1147–1150, https://doi.org/10.1029/GL008i011p01147, 1981.

Hocke, K.: Oscillations of global mean TEC, J. Geophys. Res., 113, 1–13, A04302, https://doi.org/10.1029/2007JA012798, 2008.

IUP: Mg-II index, available at: http://www.iup.uni-bremen.de/UVSAT/Datasets/mgii, last access: 30 June 2017.

Jacobi, C., Jakowski, N., Schmidtke, G., and Woods, T. N.: Delayed response of the global total electron content to solar EUV variations, Adv. Radio Sci., 14, 175–180, https://doi.org/10.5194/ars-14-175-2016, 2016.

Jakowski, N., Fichtelmann, B., and Jungstand, A.: Solar activity control of Ionospheric and thermospheric processes, J. Atmos. Terr. Phys., 53, 1125–1130, https://doi.org/10.1016/0021-9169(91)90061-B, 1991.

LASP (2017): LASP Interactive Solar Irradiance Data Center, available at: http://lasp.colorado.edu/lisird, last access: 30 June 2017.

Lean, J. L., White, O. R., Livingston, W. C., and Picone, J. M.: Variability of a composite chromospheric irradiance index during the 11-year activity cycle and over longer time periods, J. Geophys. Res., 106, 10645–10658, https://doi.org/10.1029/2000JA000340, 2001.

Lean, J. L., Woods, T. N., Eparvier, F. G., Meier, R. R., Strickland, D. J., Correira, J. T., and Evans, J. S.: Solar extreme ultraviolet irradiance: Present, past, and future, J. Geophys. Res., 116, A01102, https://doi.org/10.1029/2010JA015901, 2011.

Lee, C. K., Han, S. C., Bilitza, D., and Seo, K. W.: Global characteristics of the correlation and time lag between solar and ionospheric parameters in the 27-day period, J. Atmos. Sol-Terr. Phy., 77, 219–224, https://doi.org/10.1016/j.jastp.2012.01.010, 2012.

Liu, L., Wan, W., Ning, B., Pirog, O. M., and Kurkin V. I.: Solar activity variations of the ionospheric peak electron density, J. Geophys. Res., 111, A08304, https://doi.org/10.1029/2006JA011598, 2006.

Maruyama, T.: Solar proxies pertaining to empirical ionospheric total electron content models, J. Geophy. Res., 15, A04306, https://doi.org/10.1029/2009JA014890, 2010.

McNamara, L. F. and Smith, D. H.: Total electron content of the ionosphere at 31 S, 1967–1974, J. Atmos. Terr. Phys., 44, 227–239, https://doi.org/10.1016/0021-9169(82)90028-9, 1982.

Millward, G. H., Moffett, R. J., Quegan, S., and Fuller-Rowell, T. J.: A coupled thermosphere-ionosphere-plasmasphere model (CTIP), in: Solar-Terrestrial Energy Program: Handbook of Ionospheric Models, edited by: Schunk, R. W., Cent. for Atmos. and Space Sci., Utah State Univ., Logan, Utah, USA, 239–279, 1996.

Millward, G. H., Müller-Wodarg, I. C. F., Aylward, A. D., Fuller-Rowell, T. J., Richmond, A. D., and Moffett, R. J.: An investigation into the influence of tidal forcing on F region equatorial vertical ion drift using a global ionosphere-thermosphere model with coupled electrodynamics, J. Geophys. Res., 106, 24733–24744, https://doi.org/10.1029/2000JA000342, 2001.

Min, K., Park, J., Kim, H., Kim, V., Kil, H., Lee, J., Rentz, S., Lühr, H., and Paxton, L.: The 27-day modulation of the low-latitude ionosphere during a solar maximum, J. Geophys. Res., 114, A04317, https://doi.org/10.1029/2008JA013881, 2009.

Negrea, C., Codrescu, M. V., and Fuller-Rowell, T. J.: On the validation effort of the Coupled Thermosphere Ionosphere Plasmasphere Electrodynamics model, Adv. Space Res., 10, S08010, https://doi.org/10.1029/2012SW000818, 2012.

Noll, C.: The Crustal Dynamics Data Information System: A resource to support scientific analysis using space geodesy, Adv. Space Res., 45, 1421–1440, https://doi.org/10.1016/j.asr.2010.01.018, 2010.

Oinats, A. V., Ratovsky, K. G., and Kotovich, G. V.: Influence of the 27-day solar flux variations on the ionosphere parameters measured at Irkutsk in 2003–2005, Adv. Space Res., 42, 639–644, https://doi.org/10.1016/j.asr.2008.02.009, 2008.

Pesnell, W. D., Thompson, B. J., and Chamberlin, P. C.: The Solar Dynamics Observatory (SDO), Solar Phys., 275, 3–15, https://doi.org/10.1007/s11207-011-9841-3, 2012.

Quegan, S., Bailey, G. J., Moffett, R. J., Heelis, R. A., Fuller-Rowell, T. J., Rees, D., and Spiro, R. W.: A theoretical study of the distribution of ionization in the high-latitude ionosphere and the plasmasphere: First results on the mid-latitude trough and the light-ion trough, J. Atmos. Terr. Phys., 44, 619–640, https://doi.org/10.1016/0021-9169(82)90073-3, 1982.

Rawer, K., Bilitza, D., and Ramakrishnan, S.: Goals and status of the International Reference Ionosphere, Rev. Geophys., 16, 177–181, https://doi.org/10.1029/RG016i002p00177,1978.

Richmond, A. D., Ridley, E. C., and Roble, R. G.: A thermosphere/ionosphere general circulation model with coupled electrodynamics, Geophys. Res. Lett., 19, 601–604, https://doi.org/10.1029/92GL00401, 1992.

Rishbeth, H.: Day-to-day ionospheric variations in a period of high solar activity, J. Atmos. Terr. Phys., 55, 165–171, https://doi.org/10.1016/0021-9169(93)90121-E, 1993.

Roble, R. G., Ridley, E. C., Richmond, A. D., and Dickinson, R. E.: A coupled thermosphere/ionosphere general circulation model, Geophys. Res. Lett., 15, 1325–1328, https://doi.org/10.1029/GL015i012p01325, 1988.

Sterling, D. L., Hanson, W. B., Moffett, R. J., and Baxter, R. G.: Influence of electromagnetic drift and neutral air winds on some features of the F2-region, Radio Sci., 4, 1005–1023, https://doi.org/10.1029/RS004i011p01005, 1969.

Su, Y. Z., Bailey, G. J., and Fukao, S.: Altitude dependencies in the solar activity variations of the ionospheric electron density, J. Geophys. Res., 104, 14879–14891, https://doi.org/10.1029/1999JA900093, 1999.

Tapping, K. F.: Recent solar radio astronomy at centimeter wavelengths: The temporal variability of the 10.7 cm flux, J. Geophys. Res., 92, 829–838, https://doi.org/10.1029/JD092iD01p00829, 1987.

Unglaub, C., Jacobi, C., Schmidtke, G., Nikutowski, B., and Brunner, R.: EUV-TEC proxy to describe ionospheric variability using satellite-borne solar EUV measurements: First results, Adv. Space Res., 47, 1578–1584, https://doi.org/10.1016/j.asr.2010.12.014, 2011.

Unglaub, C., Jacobi, Ch., Schmidtke, G., Nikutowski, B., and Brunner, R.: EUV-TEC proxy to describe ionospheric variability using satellite-borne solar EUV measurements, Adv. Radio Sci., 10, 259–263, https://doi.org/10.5194/ars-10-259-2012, 2012.

Viereck, R., Puga, L., McMullin, D., Judge, D., Weber, M., and Tobiska, W. K.: The Mg II index: A proxy for solar EUV, Geophys. Res. Lett., 28, 1343–1346, https://doi.org/10.1029/2000GL012551, 2001.

Wintoft, P.: The variability of solar EUV: A multiscale comparison between sunspot number, 10.7 cm flux, LASP MgII index,

and SOHO/SEM EUV flux, J. Atmos. Sol. Terr. Phys., 73, 1708–1714, https://doi.org/10.1016/j.jastp.2011.03.009, 2011.

Woods, T. N. and Eparvier, F. G.: Solar ultraviolet variability during the TIMED mission, Adv. Space Res., 37, 219–224, https://doi.org/10.1016/j.asr.2004.10.006, 2006.

Woods, T. N. and Rottman, G.: Solar ultraviolet variability over time periods of aeronomic interest, in: Atmospheres in the Solar System: Comparative Aeronomy, Geophys. Monogr. Ser., vol. 130, edited by: Mendillo, M., Nagy, A., and Waite, J. H., 221–234, AGU, Washington, DC, https://doi.org/10.1029/130GM14, 2002.

Woods, T. N., Bailey, S., Eparvier, F., Lawrence, G., Lean, J., McClintock, B., Roble, R., Rottmann, G. J., Solomon, S. C., Tobiska, W. K., and White, O. R.: TIMED Solar EUV Experiment, Phys. Chem. Earth Pt. C, 25, 393–396, https://doi.org/10.1016/S1464-1917(00)00040-4, 2000.

Woods, T. N., Eparvier, F., Bailey, S., Chamberlin, P., Lean, J., Rottmann, G. J., Solomon, S. C., Tobiska, W. K., and Woodraska, D. L.: Solar EUV Experiment (SEE): Mission overview and first results, J. Geophys. Res., 110, A01312, https://doi.org/10.1029/2004JA010765, 2005.

Woods, T. N., Eparvier, F. G., Hock, R., Jones, A. R., Woodraska, D., Judge, D., Didkovsky, L., Lean, J., Mariska, J., Warren, H., McMullin, D., Chamberlin, P., Berthiaume, G., Bailey, S., Fuller-Rowell, T., Sojka, J., Tobiska, W. K., and Viereck, R.: Extreme Ultraviolet Variability Experiment (EVE) on the Solar Dynamics Observatory (SDO): Overview of Science Objectives, Instrument Design, Data Products, and Model Developments, Sol. Phys., 275, 115–143, https://doi.org/10.1007/s11207-009-9487-6, 2012.

3 Paper 2: Long term trends of ionospheric response to solar EUV variations

In this paper, the relation between GTEC and different solar EUV proxies during the period from January 1999 to December 2017 is investigated and evaluated. The purpose of using different proxies (F10.7, F1.8, F3.2, F8, F15, F30, He II, Mg II index, Ly-α, Ca II K, daily SSA, and SSN) is to estimate the respective correlation and ionospheric lag in order to identify proxies best suited to describe the solar-ionosphere relationship on different time scales and under different solar activity conditions. Cross-wavelet and Lomb-Scargle-periodogram (LSP) analyzes are used to evaluate the different solar proxies in terms of their relation with the GTEC, which is important for improved ionospheric modeling and prediction. Therefore, the ionospheric delay at the different solar irradiance oscillation periods is addressed to investigate the response of the GTEC to solar variations as indicated by different solar proxies. To understand the variability in the ionosphere, we use the empirical orthogonal functions (EOFs) method to classify the temporal and spatial variability in the ionosphere.

This paper has discussed long-term ionospheric changes due to solar EUV and UV, which is important for improved ionospheric modeling and prediction. Our main findings are:

- The cross-wavelet analysis represents the period from 16 to 32 d in all solar proxies and GTEC.

- The maximum correlation with GTEC is observed between the He II index, Mg II index, and F30 in the period range from 16 to 32 d along with a time lag of about 1 day.

- Wavelet variance estimation shows that GTEC variance is high in the interval of

64 to 128 d followed by 16 to 32 d, while F10.7 index shows high variance in the interval of 16 to 32 d.

- The most suitable proxy to represent the solar activity on the time scales of 16 to 32 and 32 to 64 d during low, medium, and high solar activity is He II.

- The Mg II index, Ly-α, and F30 can be placed second, as these indices show a strong correlation with GTEC, but with some differences between solar maximum and minimum.

- The F1.8 and the daily SSA poorly represent the influence of solar activity on TEC.

- The first EOF component captures more than 86 % of the variability, and the first three EOF components explain 99 % of the variance. EOF analysis suggests that the first component is associated with solar flux and the third EOF component captures geomagnetic activity as well as the remaining part of EOF1. EOF2 captures 11 % of the total variability and shows hemispheric asymmetry.

- The spatial and temporal distribution of the cross-correlation was estimated using the Mg II index. The results show significant temporal and spatial variations.A stronger correlation is observed near the equatorial region, with a time lag of about 1-2 d. The correlation is more pronounced in the equatorial region. The magnetospheric inputs probably affect both the high and low latitude regions, but with different sign.

The analysis compares the solar proxies for representing solar activity on different time scales and suggests the best solar proxy based on correlation and delay. Therefore, an in-depth analysis on different time scales is required to find out the best solar proxy for representing solar activity in T-I model.

This paper, **Vaishnav et al., 2019** is committed to finding the best solar proxy to represent solar activity on different time scales with respect to GTEC.

Research paper

[**Vaishnav et al., 2019**] Vaishnav, R., Jacobi, C., and Berdermann, J. (2019). Long-term trends in the ionospheric response to solar extreme-ultraviolet variations, Annales Geophysicae, 37, 1141–1159, https://doi.org/10.5194/angeo-37-1141-2019.

Author contributions statement

The doctoral student performed the following tasks independently for this paper: Conceptualizing the approach, analyzing the data, compiling and creating graphs, interpretation and conclusion, and writing the first draft of the paper.

Annales
Geophysicae

Long-term trends in the ionospheric response to solar extreme-ultraviolet variations

Rajesh Vaishnav[1], Christoph Jacobi[1], and Jens Berdermann[2]

[1]Leipzig Institute for Meteorology, Universität Leipzig, Stephanstr. 3, 04103 Leipzig, Germany
[2]German Aerospace Center, Kalkhorstweg 53, 17235 Neustrelitz, Germany

Correspondence: Rajesh Vaishnav (rajesh_ishwardas.vaishnav@uni-leipzig.de)

Abstract. The thermosphere–ionosphere system shows high complexity due to its interaction with the continuously varying solar radiation flux. We investigate the temporal and spatial response of the ionosphere to solar activity using 18 years (1999–2017) of total electron content (TEC) maps provided by the international global navigation satellite systems service and 12 solar proxies (F10.7, F1.8, F3.2, F8, F15, F30, He II, Mg II index, Ly-α, Ca II K, daily sunspot area (SSA), and sunspot number (SSN)). Cross-wavelet and Lomb–Scargle periodogram (LSP) analyses are used to evaluate the different solar proxies with respect to their impact on the global mean TEC (GTEC), which is important for improved ionosphere modeling and forecasts. A 16 to 32 d periodicity in all the solar proxies and GTEC has been identified. The maximum correlation at this timescale is observed between the He II, Mg II, and F30 indices and GTEC, with an effective time delay of about 1 d. The LSP analysis shows that the most dominant period is 27 d, which is owing to the mean solar rotation, followed by a 45 d periodicity. In addition, a semi-annual and an annual variation were observed in GTEC, with the strongest correlation near the equatorial region where a time delay of about 1–2 d exists. The wavelet variance estimation method is used to find the variance of GTEC and F10.7 during the maxima of the solar cycles SC 23 and SC 24. Wavelet variance estimation suggests that the GTEC variance is highest for the seasonal timescale (32 to 64 d period) followed by the 16 to 32 d period, similar to the F10.7 index. The variance during SC 23 is larger than during SC 24. The most suitable proxy to represent solar activity at the timescales of 16 to 32 d and 32 to 64 d is He II. The Mg II index, Ly-α, and F30 may be placed second as these indices show the strongest correlation with GTEC, but there are some differences in correlation during solar maximum and minimum years, as the behavior of proxies is not always the same. The indices F1.8 and daily SSA are of limited use to represent the solar impact on GTEC. The empirical orthogonal function (EOF) analysis of the TEC data shows that the first EOF component captures more than 86 % of the variance, and the first three EOF components explain 99 % of the total variance. EOF analysis suggests that the first component is associated with the solar flux and the third EOF component captures the geomagnetic activity as well as the remaining part of EOF1. The EOF2 captures 11 % of the total variability and demonstrates the hemispheric asymmetry.

1 Introduction

The interaction of solar radiation with the ionosphere is complicated due to several mechanisms with the potential to modulate the thermosphere–ionosphere (T-I) system at different timescales ranging from the 11-year solar cycle down to minutes (e.g., Liu et al., 2003; Afraimovich et al., 2008; Liu and Chen, 2009; Chen et al., 2012). The ionosphere plasma response to solar EUV and UV variations has been widely studied using ground- and space-based observations (e.g., Jakowski et al., 1991; Jacobi et al., 2016; Schmölter et al., 2018; Jakowski et al., 1999), as well as by numerical and empirical modeling (e.g., Ren et al., 2018; Vaishnav et al., 2018a, b). These studies have shown that the response of the ionosphere to solar EUV radiation variations is delayed by 1–2 d at the 27 d solar rotation period (e.g., Jakowski et al., 1991; Afraimovich et al., 2008; Jakowski et al., 2002; Min et al., 2009; Jacobi et al., 2016; Lee et al., 2012).

To understand the underlying mechanisms of the delay observed in the ionospheric plasma, Jakowski et al. (1991) used a one-dimensional numerical model to explain the ionospheric delay of about 1–2 d. They concluded that the ionospheric delay could be attributed to the delayed atomic oxygen density variation at 180 km height produced via O_2 photodissociation. Ren et al. (2018) performed multiple numerical experiments using the Thermosphere–Ionosphere Electrodynamics General Circulation Model (TIE-GCM) to investigate the potential physical mechanisms responsible for the ionospheric delay. Their simulation results revealed that photochemical, dynamic, and electrodynamic processes, as well as the geomagnetic activity, can be associated with the ionosphere response time. Vaishnav et al. (2018b) performed CTIPe model simulations to explore the dominant mechanisms and suggested that transport might be the leading process responsible for the ionospheric delay.

Apart from solar radiation, the T-I system is also influenced by different external forces, which include lower atmosphere forcing, particle precipitation, geomagnetic, and solar wind conditions (e.g., Min et al., 2009; Jakowski et al., 1999). As a result, the ionospheric plasma behavior is continuously varying depending particularly on the solar activity conditions. Lean et al. (2016) constructed a statistical model and characterized the spatial patterns of the ionospheric behavior at different timescales arising from the solar and geomagnetic conditions and showing annual and seasonal oscillations. Medium-term and long-term ionospheric variability, ionospheric storm time response, solar activity, and geomagnetic response were discussed by Kutiev et al. (2013).

The mean solar rotation period is approximately 27 d, and therefore similar periodic variations are expected in the ionospheric parameters, such as total electron content (TEC, measured in TECU: 1 TEC unit $= 10^{16}$ electrons m^{-2}), NmF2, etc. (e.g., Min et al., 2009). Hocke (2008) studied oscillations in the global mean TEC (GTEC) and solar EUV (Mg II index) and reported dominant periodicity at the timescale of the solar rotation and the annual, semi-annual, and solar cycles. These oscillations observed in GTEC could be related to the ionizing radiation changes. Kutiev et al. (2012) studied the middle- and low-latitude ionospheric response to solar activity. They suggested that the 27 d periodicity is the main dominant oscillation during the study period.

In order to understand the variability of the T-I system, the knowledge of solar EUV variations is essential. Since direct EUV measurements before the space age were not available due to atmospheric absorption, solar proxies have been frequently used to represent solar variability. The most widely used proxies for ionospheric applications are the F10.7 index (solar radio flux at 10.7 cm, measured in solar flux units, sfu; see Tapping, 1987, Maruyama, 2010), the Mg II index (the core-to-wing ratio of the Magnesium K line; Maruyama, 2010), and indices based on direct EUV measurements (e.g., Schmidtke, 1976; Unglaub et al., 2011; Jacobi et al., 2016) such as the Solar EUV Experiment (SEE, Woods et al., 2000)

onboard the Thermosphere Ionosphere Mesosphere Energetics and Dynamics (TIMED) satellite. Using the latter poses the potential problem of satellite degradation (BenMoussa et al., 2013; Schmidtke et al., 2015), which may be overcome by repeated calibration or in-flight calibration as was applied during the SolACES experiment on board the ISS (Schmidtke et al., 2014, 2015). The understanding and realistic estimation of solar irradiance have been an open issue for long times, but in recent times the EUV datasets (either direct measurements, composite datasets, or models) have considerably improved (e.g., Haberreiter et al., 2017).

This paper investigates and evaluates the correlation between GTEC and different solar EUV proxies in the time period January 1999 to December 2017. The purpose of utilizing several proxies is to estimate the respective correlation and the ionospheric delay to identify proxies which are most suitable for describing the solar–ionosphere relationship at different timescales and under different solar activity conditions. Therefore, the ionospheric delay at the different oscillation periods of solar irradiance is addressed to investigate GTEC response to solar variations as indicated by various solar proxies. To understand the variability in the ionosphere, we use the method of empirical orthogonal functions (EOFs) in order to classify the temporal and spatial variability in the ionosphere.

2 Datasets

Global TEC maps for the period 1999 to 2017 are available from the International Global Navigation Satellite Systems (GNSS) Service (IGS, Hernández-Pajares et al., 2009). We used NASA's 2-hourly global TEC maps, which are available in IONEX format from the CDDIS (ftp://cddis.gsfc.nasa.gov/gnss/products/ionex/, last access: 15 August 2018; Noll, 2010) data archive service (CDDIS, 2018). These maps are available at a spatial resolution of 2.5° in latitude and 5° in longitude. We selected 12 solar proxies for GTEC correlation analysis, namely the F10.7 index; the Bremen composite Mg II index (IUP, 2018); the Ca II K index; the daily sunspot area (SSA); the He II (Dudok de Wit, 2011); and the F1.8, F3.2, F8, F15, and F30 solar radio flux emission at five wavelengths (Dudok de Wit et al., 2014; Haberreiter et al., 2017) as well as Ly-α and SSN (sunspot number, Wolf, 1856) indices, which are available from NASA's Goddard Space Flight Center through the OMNIWeb Plus database (http://omniweb.gsfc.nasa.gov/, last access: 15 August 2018; King and Papitashvili, 2005). The F10.7 index data were taken from the LISIRD (Dewolfe et al., 2010) database, whereas F1.8, F3.2, F8, F15, F30, Ca II K index and daily SSA proxies are available from the SOLID database (http://projects.pmodwrc.ch/solid/, last access: 15 August 2018; Schöll et al., 2016; Haberreiter et al., 2017). SOLID data were only available for the time interval 1999–2012 and all other data cover the full period from 1999 to 2017. The daily

TEC and GTEC values were calculated from the gridded 2-hourly TEC maps to obtain a time resolution corresponding to those of the solar proxies. Further, to investigate the relation between GTEC and geomagnetic activity, we have used daily Kp, Dst, and Ap indices, which were taken from the OMNIWeb Plus database. To calculate the cross-correlation between solar proxies and GTEC, we used the wavelet cross-correlation analysis, cross-correlation sequence, and Pearson cross-correlation method.

3 Results and discussion

3.1 Long-term variations of TEC and EUV flux

In the following, we analyze the long-term variations of GTEC and EUV flux for the period 1999 to 2017, which partially covers the solar cycles (SCs) 23 and 24. The temporal variation of the zonal mean TEC is shown in Fig. 1a.

In SC 23, the TEC values at low latitudes reach up to 80 TECU, while during SC 24 TEC was considerably smaller, which confirms that the zonal mean TEC behavior is strongly dependent on the solar activity, as the solar activity was very low during SC 24 compared to SC 23. The amount of free electrons in the ionosphere mainly depends on the photoionization of atomic and molecular neutrals due to solar EUV radiation along with the recombination at different heights and solar zenith angles. The lowest TEC values are observed in the years 2008 and 2009 during the extended solar minimum of SC 23 (Nikutowski et al., 2011). From the zonal mean plot (Fig. 1a), temporal variations are visible, which result from annual and semi-annual variations in the ionosphere. Figure 1b shows the normalized time series of GTEC and 12 solar proxies for the available data in the analyzed time period 1999–2017. Note that Emmert et al. (2017) showed that GTEC values before 2001 are lower than values observed later. This effect should, however, be of minor importance for our analyses below. As the ionosphere response to solar radiation varies for different wavelengths, we used 12 solar proxies based on different measurement techniques and spectral characteristics. Hocke (2008) analyzed GTEC and Mg II index observations and showed that 1 % change in Mg II index results in about 22 % change in GTEC. The time series in Fig. 1 show a similar overall variation during the 11-year solar cycle. The fundamental behavior of solar radiation emission is not identical at all wavelengths and thus for all solar proxies, as the plasma heating and atomic processes are different (Dudok de Wit et al., 2014) but the long-term trends and variations look similar for all the proxies shown here.

Figure 2 shows the spatial variation of TEC averaged over the period 1999 to 2017, where the superimposed white contour lines show the standard deviation calculated from the daily TEC data. The magnetic equator is indicated by a dashed black line. A similar analysis has been shown by Guo et al. (2015) using the same TEC dataset within the period 1999 to 2013, finding a comparable spatial distribution. The maximum TEC values are distributed along the equator around ±20° and decrease towards the poles. Maximum values of the standard deviation are observed in the low-latitude region with about 15 TECU. The spatial distribution of TEC depends on the ionization of neutrals, transport processes, and recombination, which varies with latitude and longitude.

Note that the T-I system is not only influenced by the solar electromagnetic radiation but also by changing solar energetic particles and geomagnetic conditions due to solar wind variations or coronal mass ejections reaching the Earth (e.g., Abdu, 2016; Tsurutani et al., 2009). The response to solar forcing is higher during solar maximum when the interaction of the solar wind with Earth's upper atmosphere causes ionospheric disturbances at high latitudes along magnetic field lines visible in enhanced TEC values. During solar maxima, the T-I regime can partially be controlled by the solar wind activity superseding the solar radiation impact. However, during periods of low solar activity, the local variability in the ionosphere is also not only regulated by the solar radiation but can be influenced by lower atmospheric forcing (e.g., Forbes et al., 2000; Knížová et al., 2015) and by the solar wind, in particular from coronal holes (e.g., Zurbuchen et al., 2012; Verkhoglyadova et al., 2013).

3.2 Spectra of GTEC and solar proxies

The datasets mentioned above are used to analyze the oscillatory behavior of the T-I system. The periodicities in the solar proxies have been studied by various authors to explore the response of the terrestrial atmosphere and especially the T-I region to solar variability. Here we will investigate and compare the different temporal patterns of GTEC and multiple solar proxies, since proxies may differ in their periodicity depending on the underlying source mechanism.

The cross-wavelet technique from Grinsted et al. (2004) was applied, where Morlet wavelets were used as mother functions. The cross-wavelet technique allows common high-power regions between two time series to be indicated. This allows us to determine the dominant correlated oscillations of the ionosphere and important solar proxies. The cross-wavelet analyses of GTEC with four selected solar proxies (F10.7, Mg II, SSN, and Ly-α) are shown in Fig. 3. The most dominant periods observed are in the 16 to 32 d interval visible in all GTEC solar proxy relations during solar maxima. This is, however, not the case during solar minimum when the solar-driven ionospheric variation is lower due to lower solar activity, and the influence of other dynamical processes in the ionosphere (e.g., lower atmospheric forcing) is stronger. Another high-power region is visible in the 128 to 256 d period, representing the semi-annual oscillations in both GTEC and solar parameters. The semi-annual oscillation is mostly dominant during the solar maximum years 2001–2002 and 2011–2012. The black arrows in Fig. 3 indicate the phase relationship between solar proxies and
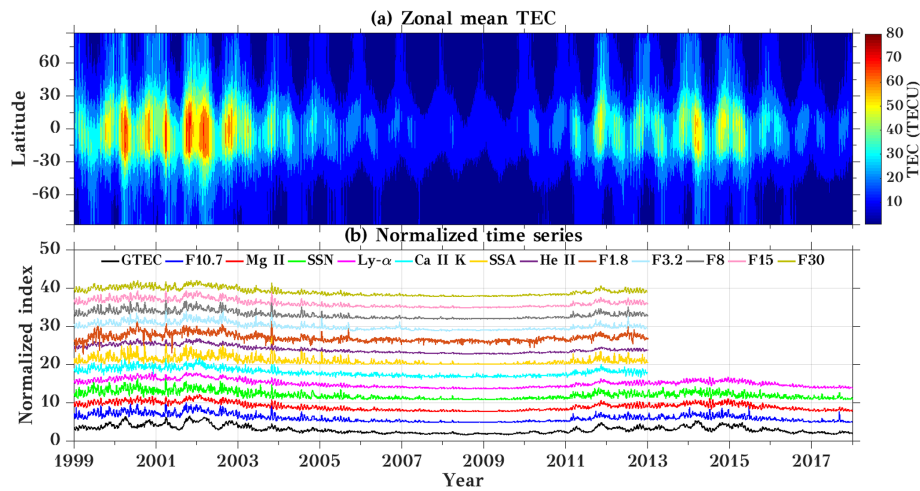
Figure 1. Time series of **(a)** zonal mean TEC and **(b)** smoothed normalized datasets of GTEC and different solar proxies for the years 1999 to 2017. The curves in **(b)** are vertically offset by 3 each. *x* axis labels refer to 1 January of the respective year.
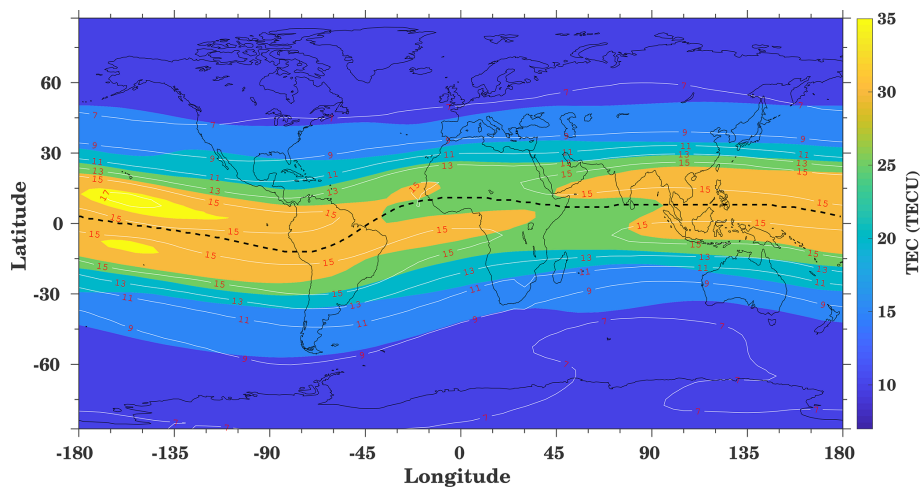

Figure 2. Long-term diurnal and annual mean TEC distribution during the years 1999 to 2017. The white contour lines indicate the standard deviation based on daily data. The black dashed line represents the magnetic equator.

GTEC, with in-phase (anti-phase) relation shown by arrows pointing to the right (left), while a downward (upward) direction means that GTEC is leading (lagging). As expected, in the region of 16 to 32 d GTEC is broadly in phase with the solar proxies, whereas this behavior is not consistent in the semi-annual (128 to 256 d) and annual (256 to 512 d) period ranges. The most dominant joint annual oscillations are observed between GTEC and Ly-α. The annual oscillation can be found mostly during solar maximum.

To examine the oscillatory behavior of GTEC and solar proxies more precisely, the Lomb–Scargle periodogram (LSP, Lomb, 1976; Scargle, 1982) technique was used. The corresponding spectral analysis is shown in Fig. 4. Here, the power was normalized and converted into a logarithmic scale, and the 95 % confidence level is added to each spectrum as a dashed blue line. The curves have been vertically

offset by 15. In this analysis, data from 1999 to 2012–2017 were used. The dominant frequencies observed in GTEC are 27 d, annual, and semi-annual, which is in line with Hocke (2008). Clearly visible in all the solar proxies as well as in GTEC is the mean solar rotation period of about 27 d. Pancheva et al. (1991) showed that the 27 d variation in the lower ionosphere (D region) is often predominantly caused by dynamical forcing (planetary waves), not by direct solar forcing, particularly in winter under low solar activity. However, the D region ionization contributes only weakly to TEC. A 45 d periodicity is observed GTEC, F10.7, Mg II, and SSN. A 45 d periodicity was reported in various solar proxies (Lou et al., 2003; Kilcik et al., 2016, 2018; Chowdhury et al., 2015) using LSP and wavelet analysis. Lou et al. (2003) reported a period of about 42 d in X-Ray solar flares during SC 23. Kilcik et al. (2018) analyzed sunspot counts in
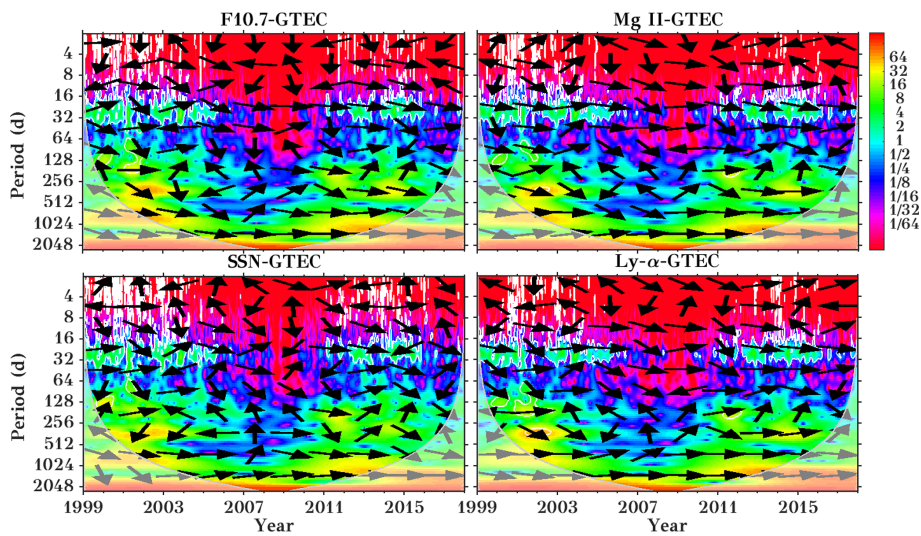
Figure 3. Cross-wavelet spectra for GTEC and different solar proxies during the years 1999 to 2017. The thin gray line shows the cone of influence, where a white line surrounds significant values. The arrows indicate the phase relationship, with in-phase and anti-phase relation shown by arrows pointing to the right and left, respectively, while a downward or upward direction means that GTEC is leading or lagging, respectively. *x* axis labels refer to 1 January of the respective year.
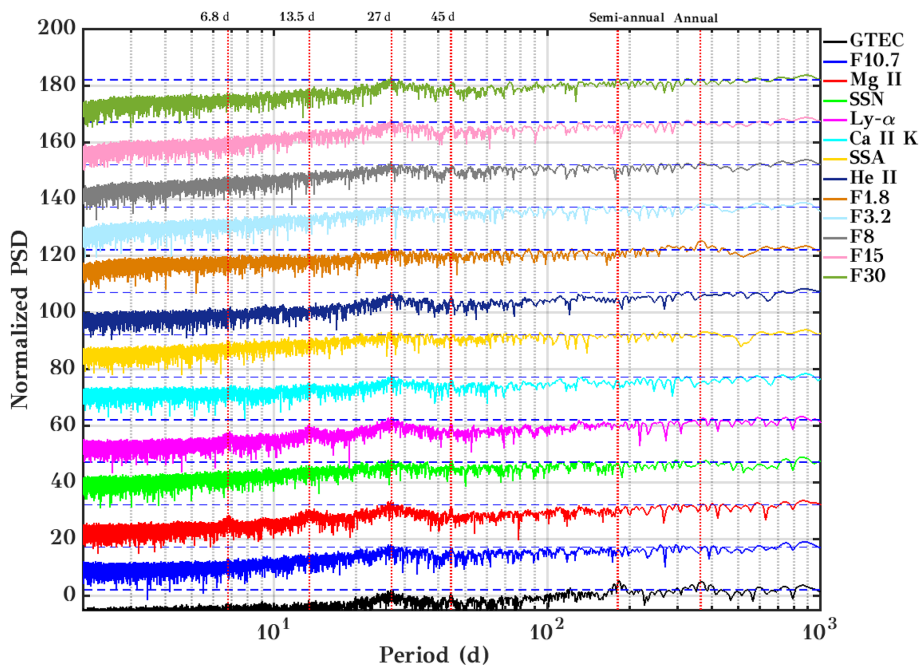

Figure 4. Lomb–Scargle periodogram for GTEC and multiple solar proxies with a 95 % confidence line (dashed blue color line). The curves are vertically offset by a factor of 15 each.

flaring and non-flaring active regions for SCs 23 and 24 and observed a 45 d periodicity in flaring active regions. They concluded that a 45 d period is one of the fundamental periods of flaring active regions. A similar periodicity was observed during SC 24 by Chowdhury et al. (2015) in SSA, SSN, and the F10.7 index.

In the Mg II index, which is widely used to represent the solar variability, the dominant periods observed are 27 d, and its second harmonic 13.5 d also described by Hocke (2008). Here the same oscillation is also visible in the Ly-α spectrum. In the F1.8 index, the annual frequency is observed. A semi-annual oscillation is seen in GTEC. This variation is associated with a dynamical effect of the at-

mosphere (Liu et al., 2006). Note that the wavelet spectra show some periodicity at the half-year timescale for GTEC and F30, but with variable phase so that they extinguish in the periodogram. 128 and 256 d periodicities were reported by various authors (Lou et al., 2003; Kilcik et al., 2014, 2018; Chowdhury et al., 2009). Lou et al. (2003) reported a 259 ± 24 d variation in M5 class X-ray flares during the solar maximum of SC 23. This periodicity may be attributed to non-flaring active regions and developed sunspot groups (Kilcik et al., 2018). Further, Kilcik et al. (2014, 2018) confirmed that the 128 d periodicity is one of the characteristic periodicities of solar flares and also flaring active regions.

3.3 Wavelet cross-correlation

To evaluate the relation between the solar proxies and GTEC, we analyzed the wavelet cross-correlation for the different periods 8 to 16, 16 to 32, 32 to 64, and 64 to 128 d using the wavelet cross-correlation sequence method based on the maximal overlap discrete wavelet transform (MODWT) technique (Percival and Walden, 2000). The MODWT technique is a modified version of the discrete wavelet transform from Mallat (1989).

In Fig. 5 these cross-correlation coefficients are indicated by the background color, while the inserted numbers show the ionospheric delay in days. The delay is mostly positive, which means that TEC is following the solar proxies. On the 8 to 16 d timescale, maximum correlation is found for He II with a correlation coefficient of about 0.62, and the second maximum correlation is observed for the F15 index, both with a lag of about 1 d. The lowest correlation of about 0.25 is found for the F1.8 index. Compared to the 8 to 16 d period range, the 16 to 32 d period shows a much stronger correlation, with more than about 0.6 for all the proxies. Here a maximum correlation of about 0.9 is observed for the He II and Mg II index, with a GTEC delay of about 1 d. The F30 index and the Ly-α index also shows a strong correlation. The lowest correlation of 0.59 is seen for the daily SSA. A similar result can be observed in the 32 to 64 d period range. Here, maximum correlation is observed again for the He II and Mg II indices, which have a correlation coefficient of 0.9 and a delay of about 2 d. Another particular strong correlation of about 0.8 is observed with Ly-α and Ca II K having a GTEC delay of about 1 and 2 d, respectively. Only a weak correlation of about 0.5 with small GTEC lag time is seen for the daily SSA. The similar behavior in the 16 to 32 and 32 to 64 d intervals is owing to the fact that the 27 d periodicity is only a mean value of the solar differential rotation. It also strongly depends on the lifetime and proper motion of the observed active regions. This results in strong correlations, also observable in the 32 to 64 d interval. In the 64 to 128 d interval, a longer time lag is reached with above 5 d for several proxies. Here the maximum correlation is found for the He II index with about 0.6 and the weakest correlation is seen with about 0.4 for the F1.8 index. Generally, the Mg II and

He II proxies show the strongest correlation with GTEC for all period intervals. A strong correlation is also seen for Ly-α and F30, while the weakest correlation is seen for F1.8 and the daily SSA. Figure A1 in the Appendix shows the correlation between solar proxies and GTEC at zero lag at different timescales. Like Fig. 5 it shows strong correlation for Ly-α and F30.

Figure 6 shows the wavelet variance estimated for GTEC and F10.7 using the MODWT technique with the Daubechies 2 (db2) wavelet filter. Here we have selected the time series from the years 2000 to 2002 (maximum of SC 23) and 2012 to 2014 (maximum of SC 24). The red (black) color in the plot represents the SC 23 (SC 24) maximum. In GTEC, maximum variance appears in the 64 to 128 d interval, which is about a quarterly annual oscillation and belongs to the seasonal cycle, during SC 23. The second strongest variance is observed at the 16 to 32 d interval. A generally stronger variance can be observed in SC 23 compared to SC 24 for all the analyzed period intervals. In the case of the F10.7 index, the maximum variance is visible at the 16 to 32 d interval, which here shows a predominant variance for the solar rotation period. As expected, no significant semi-annual cycle is visible. Here again, the observed variance during SC 23 is stronger compared to SC 24.

3.4 Influence of the solar activity on GTEC

This work aims to understand the interaction between solar radiation and the T-I system, especially at the timescale of the solar rotation. To scrutinize the consequence of different solar activity levels on the T-I system for short and intra-annual (including all variability) timescales, we evaluate the running cross-correlation analysis between GTEC and solar proxies as shown in Fig. 7.

Figure 7a shows the running correlation for the short timescale. To calculate the short-term variation at the solar rotation period, the 27 d residual has been calculated by subtracting the 27 d running average values from corresponding datasets of GTEC and solar proxies (Mg II, SSN, and Ly-α). The running correlation is calculated using the filtered time series at the solar rotation period by using a 365 d running window. The 365 d running mean Mg II index is added to show the overall solar activity in Fig. 7a and b. The correlation is likely to vary with respect to solar activity. Lower correlation is observed during low solar activity. A similar kind of analysis was shown by Chen et al. (2012).

Furthermore, to understand the relation between GTEC and solar proxies at longer timescales, we calculate the cross-correlation between the annual means. The maximum correlation observed is about 0.93 (figure not shown) between the solar proxies and GTEC. Hence in comparison to short timescales variations, solar proxies are strongly correlated with GTEC.

Figure 7b shows correlation at the intra-annual timescale, which includes all the variations, i.e., seasonal, daily, and so-
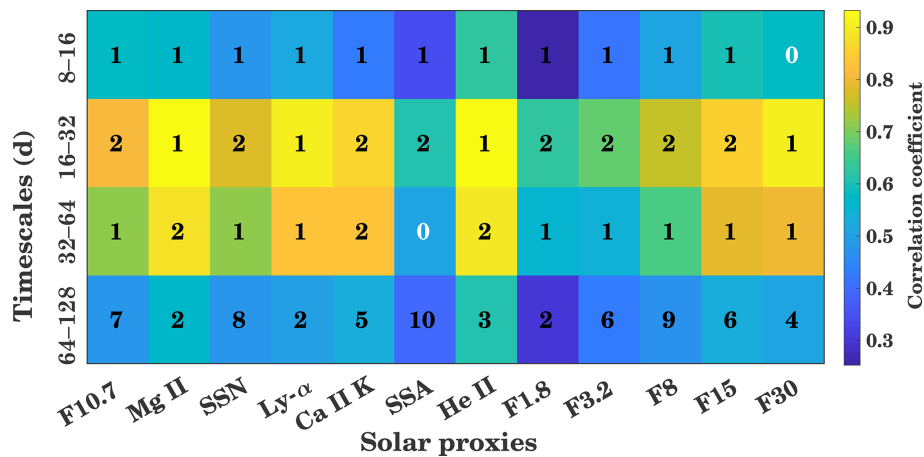
Figure 5. Wavelet cross-correlation sequence estimates for the maximal overlap discrete wavelet transform for GTEC and multiple solar proxies for different timescales (8 to 16, 16 to 32, 32 to 64, and 64 to 128 d). The background color shows the correlation coefficient, and the inserted number shows the delay in days.
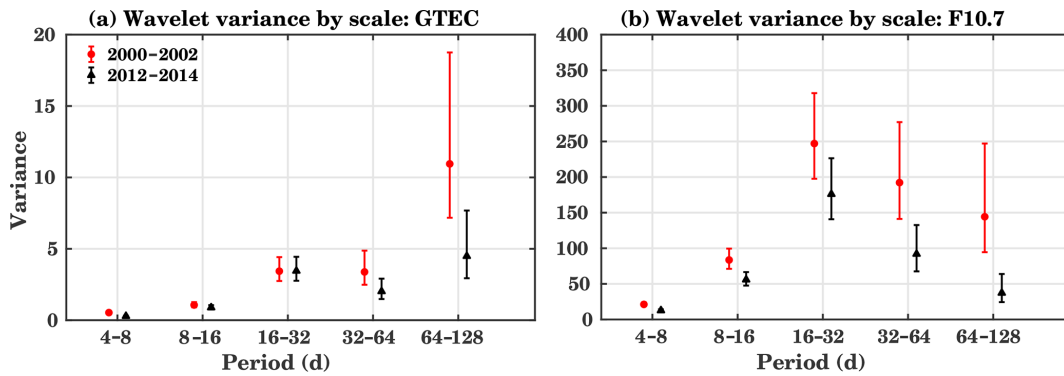

Figure 6. Wavelet variance for the maximums of SC 23 (2000–2002, red) and 24 (2012–2014, black) for **(a)** GTEC and **(b)** F10.7. Error bars show the 95 % coverage probability of the confidence interval obtained from the "Chi2Eta3" confidence method.

lar rotation. Here, a 365 d running window is used to calculate the running correlations based on unfiltered data. The correlation with all the solar proxies is smallest during the extended low solar activity phase during the solar minimum in 2008–2009. All solar proxies show similar behavior during low activity conditions: while the temporal variation of the correlation coefficient for Mg II and Ly-α is largely similar, the SSN (blue curve) shows significantly different behavior. The strongest correlation is observed during the rising part of solar cycle 24. In comparison to all the other solar proxies, Mg II and Ly-α show a stronger correlation with GTEC, while the lowest correlation is given for SSN at short and intra-annual timescales.

Solar EUV variations can be well described by the solar proxies (e.g., F10.7, SSN) at the 11-year solar cycle variations but they show weak correlation at short timescales (daily, 27 d solar rotation period) (e.g., Chen et al., 2012; Floyd et al., 2005) as shown in Fig. 7. At longer timescales, solar EUV and solar proxies are mainly controlled by solar magnetic activity. But at short timescales, these parameters

vary differently as they originate from different excitation mechanisms in the solar surface (e.g., Chen et al., 2012; Lean et al., 2001).

Figure 8 shows the cross-correlation analysis of (a) F10.7 and (b) Mg II with the global, Northern Hemisphere (NH), Southern Hemisphere (SH), low-latitude (LL, ±30°), midlatitude (ML, ±(30–60°)), and high-latitude (HL, ±(60–90°)) mean TEC. Generally, the correlation coefficients and the lag for the global, NH, SH, LL, and ML are very close to each other. The maximum correlation is found for GTEC and LL TEC with correlation coefficients of about 0.7 (F10.7) and 0.82 (Mg II) for a time delay of about 2 and 1 d, respectively. Generally, GTEC variability is mainly determined by the LL electron content, so that it is expected that the correlation coefficients for GTEC and LL are similar. The weakest correlation is observed for HL with a maximum correlation coefficient of 0.42 (F10.7) and 0.53 (Mg II) and a corresponding ionosphere response time of about 2 and 1 d, respectively (marked with a red star). NH and SH are comparable with slightly smaller correlations for SH. There is a weaker cor-
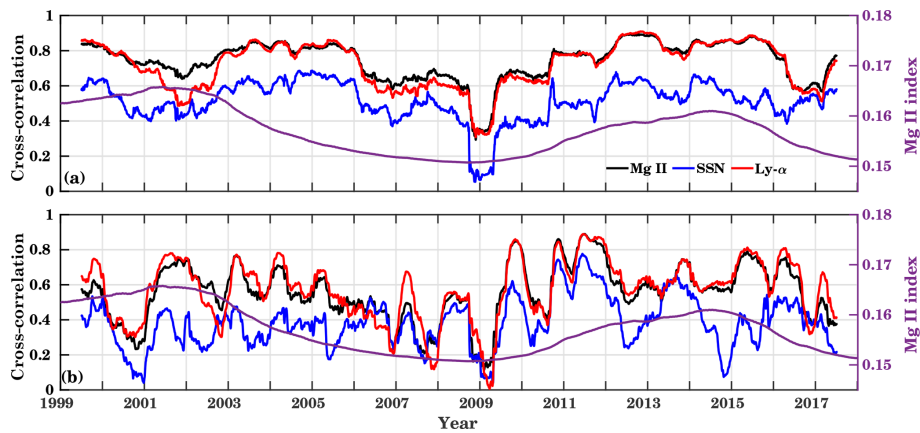
Figure 7. Running cross-correlations between GTEC and different solar proxies for **(a)** short (27 d residual), and **(b)** intra-annual timescales (original time series). For the short timescale the 27 d residuals have been calculated by removing the 27 d running mean from the original datasets. A 365 d running window is used to calculate the correlation. The second y axis shows 365 d (**a** and **b**) running mean time series of Mg II index. Here Mg II, SSN, and Ly-α are marked by black, blue, and red colors, respectively.
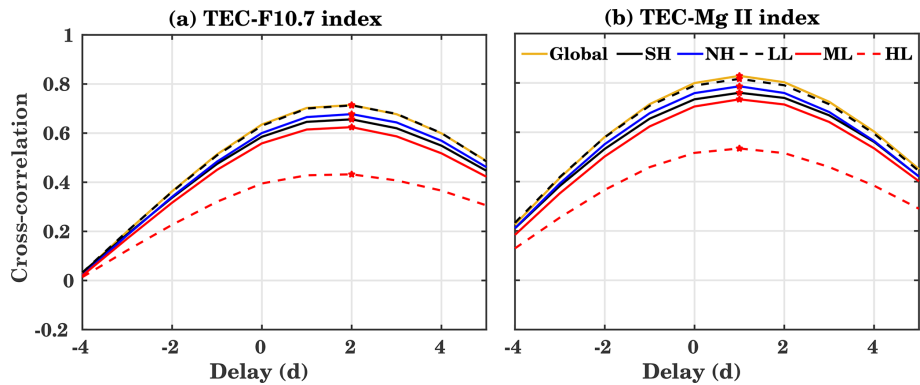
Figure 8. Cross-correlation coefficients and time delays between the global, Northern Hemisphere (NH), and Southern Hemisphere (SH) as well as low-latitude (LL, $\pm30°$), midlatitude (ML, $\pm(30\text{–}60°)$), and high-latitude (HL, $\pm(60\text{–}90°)$) TEC with **(a)** F10.7 and **(b)** Mg II index during the years 1999 to 2017 for a different lag. A positive lag means that solar flux variations are heading TEC ones. The maximum correlation is indicated by a red star.

relation for ML compared to LL, but the difference is not as large as the one for HL. Running correlations at intra-annual timescales, similar to Fig. 7, are shown in Fig. A6 in the Appendix.

Figure 9 shows the cross-correlation analysis between GTEC and solar proxies separately for each year at the timescale of 16 to 32 d. To calculate the wavelet cross-correlation, the data are filtered for different timescales using the MODWT. Figure 9a shows the 365 d running mean F10.7. The delay is given as numbers inserted on the color-coded cross-correlation for the different solar proxies and time periods. As in Fig. 7, the overall trend shows that the correlation is weak during solar minimum and strong during high solar activity periods. The time delay ranges between 0 and 3 d for all solar proxies, but without obvious regularity with respect to the proxies or the time. As in Fig. 5, a generally strong correlation is found for He II and Mg II, while

daily SSA and F1.8 indices show the weakest correlation. During the years of low solar activity 2007–2010, an especially weak correlation is visible for F3.2, F1.8, and Ca II K. The maximum F10.7 index is observed during 2001 with about 181 sfu. During the high solar activity years from 1999 to 2003 and from 2012 to 2014 a strong correlation of about 0.85 is observed for Mg II, He II, F30 (1999–2003, 2012), and Ly-α except for 2001, when the maximum annual mean F10.7 index is observed. During the maximum of SC 23, the cross-correlation between Mg II, He II, Ly-α, F3.2, F15, and GTEC is about 0.7 with a delay of about 1–2 d. A weak correlation is observed for F1.8 and Ca II K. During low solar activity (years 2006–2010, 2016) when the average F10.7 index is below 75 sfu, a stronger correlation is observed between He II and Mg II and GTEC, with a correlation coefficient of more than 0.6. Only a weak correlation during low solar activity is observed for F1.8, Ca II K, F3.2, and daily SSA. Dur-
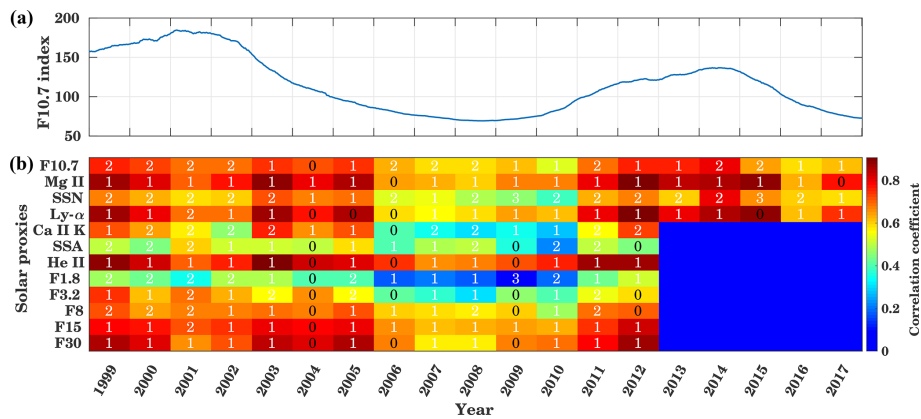
Figure 9. In panel **(a)**, the 365 d running mean time series of F10.7 is shown. Panel **(b)** displays yearly cross-correlations and time delays between GTEC and different solar proxies for the years 1999 to 2017 at the timescale of 16 to 32 d. The background colors give the maximum correlation coefficient, and the inserted numbers show the delay in days corresponding to maximum correlation.

ing moderate solar activity years (2004–2005, 2011, 2015), when the average F10.7 index is about 90–120 sfu, Mg II, He II, F30, and Ly-α show stronger correlation with GTEC with a delay of about 1 d. In summary, during low solar activity, most of the solar proxies show a weak correlation with GTEC but strong correlation is found for high solar activity. In comparison to other solar proxies, F1.8 and SSA are weakly correlated with GTEC. Figure A2 in the Appendix shows the correlation at a 16 to 32 d timescale between solar proxies and GTEC at zero lag. It shows a similar correlation to Fig. 9. In comparison to the 16 to 32 d timescales, we further analyzed the cross-correlation and delay at 32 to 64 d timescales (Fig. A3 in the Appendix).

In summary, the most suitable proxy to represent the solar activity at the timescale of 16 to 32 and 32 to 64 d during low, moderate, and high solar activity is He II. The Mg II index, Ly-α, and F30 also show a strong correlation with GTEC, but there are some differences in correlation during solar maximum and minimum years, as the behavior of proxies is not always the same. The F1.8 and daily SSA cannot adequately represent the solar activity at the solar rotation (16 to 32 d) timescale. As discussed above, solar proxies are more weakly correlated at shorter timescales than at longer timescales.

3.5 Spatial distribution of the ionospheric response time

Here we investigate the inter-annual spatial variability of the ionospheric response to solar variations. Figure 10 shows correlation and time lag between TEC and Mg II globally for a TEC map resolution of 2.5° in latitude and 5° in longitude. The left column shows yearly zonal means, while the right column shows 1999 to 2017 means with longitudinal resolution. The contour maps in Fig. 10a (b) show the cross-correlation (time delay) where the inserted contour lines represent the standard deviation.

Maximum correlation of about 0.9 is observed during high solar activity years at low latitudes. Figure 10a, b show that the correlation decreases from low to high latitudes. In the NH, the correlation is the weakest south of the auroral oval, probably due to the fact that particle precipitation also changes with solar wind dynamics. Figure 10c shows the zonal mean time delay for the year 1999 to 2017, which is about 1 d in the low and middle latitudes. The delay generally increases towards high latitudes with a few exceptions occurring during low solar activity. There is a tendency that during high solar activity, the delay is increased slightly at low latitudes, but strongly (up to 3 d) in the high-latitude region. A negative delay is observed during low solar activity, presumably associated with the meteorological effects as suggested by Ren et al. (2018). Another possible reason is ionospheric saturation, which might reduce the transport process during high solar activity due to lower recombination rates. Transport is one of the most critical parameters that control the behavior of the ionosphere. These results suggest that interannual variability depends not only on the solar activity but also on several other physical processes such as geomagnetic activity (Rich et al., 2003) and local ionospheric parameters such as neutral wind and lower atmospheric forcing through the vertical coupling. Lee et al. (2012) analyzed electron density measurements from CHAMP and GRACE along with Global Ionosphere Maps (GIM) TEC maps in relation to the F10.7 index and showed the spatial distribution of delay and correlation coefficient during the years 2003 to 2007. They found a strong (weak) correlation between GIM TEC and F10.7 in the midlatitude (high-latitude) region, with a time delay of about 1–2 (2–4) d which qualitatively confirms our results. Figure 10d shows the spatial distribution of the time delay, where an overall time delay of about 1 d with a standard deviation of less than 1 d is visible. The time delay is longer for the high-latitude region, whereas the cross-
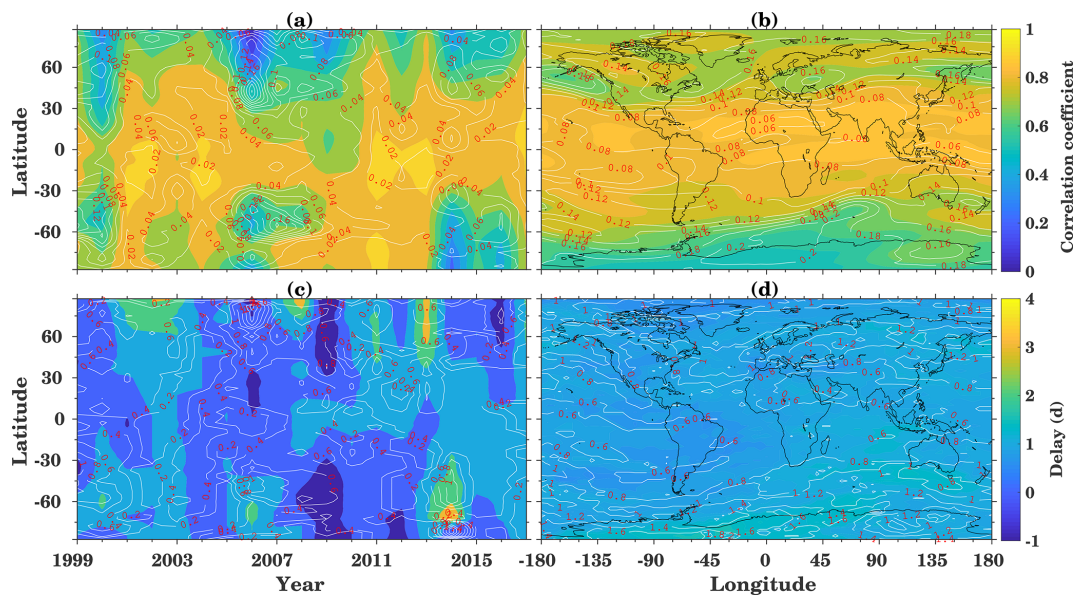
Figure 10. (a, c) Zonal mean and **(b, d)** long-term mean correlation coefficients **(a, b)** and time delay **(c, d)** between TEC and Mg II index for the years 1999 to 2017. The white contour lines indicate the respective standard deviations.

correlation is weaker, as can be seen in Fig. 10b. In this region, the standard deviation is more than 1 d.

3.6 EOF analysis of ionospheric TEC

Ionospheric TEC is varying diurnally, daily, and seasonally, on a decadal scale, as well as in latitude and longitude. To examine the spatial variability of TEC, we applied the principal component (PC) analysis for signal decomposition (Preisendorfer, 1988; Björnsson and Venegas, 1997) using EOFs, which decompose data into orthogonal modes of variability caused by solar and geomagnetic activity. The method is used to decompose the spatial–temporal field of TEC (time, longitude, latitude) into EOF components. To this end, we first calculate the data covariance matrix by using the TEC datasets, followed by finding the eigenvalues and corresponding eigenvectors (the EOFs). The explained variance of the kth EOF is the corresponding eigenvalue divided by the sum of all eigenvalues. The PC is found by projecting the TEC anomalies onto the EOF. This method has been used to represent the variability in the T-I system and for T-I modeling (e.g., Zhao et al., 2005; Matsuo et al., 2012; Ercha et al., 2012; Anderson and Hawkins, 2016; Talaat and Zhu, 2016).

We analyzed the TEC datasets in a spatial grid of $71° \times 72°$ (latitude and longitude) and a temporal length of 6940 d. Figure 11 shows the first four EOF maps in the upper panels followed by the PCs (middle panels) and the corresponding wavelet spectra (lower panels). The first three EOFs are similar to those presented by Talaat and Zhu (2016). The first EOF component explains approximately 86 % of the variance. A high variability in the low-latitude region and a smaller one at higher latitudes is shown. EOF1

shows the spatial distribution of TEC variance in general and is positive everywhere. This indicates a joint in-phase variability of the entire ionosphere, which is larger at low latitudes. Consequently, as is shown in the middle panel of Fig. 11, its temporal amplitude varies from positive to negative following the solar activity and the annual and semiannual cycle. In the lower panel of Fig. 11, the wavelet analyses for the EOFs are shown. To get clear periodicity from the wavelet, we have used log2 of the power. Negative (positive) values indicate low (high) power. The wavelet analysis of EOF1 shows a 27 d periodicity associated with the solar rotation period. Annual and semi-annual oscillations are observed, especially during the high solar activity years. The EOF2 captures 11 % of the total variability and demonstrates a hemispheric asymmetry. The corresponding PC and wavelet analysis show a strong annual variability connected with seasonal variability and larger TEC during winter.

EOF3 captures about 1.79 % of the total variability. EOF3 might be associated with non-solar effects and fine structures of the solar activity response, which is not captured by the first EOF as suggested by Talaat and Zhu (2016). Note that EOF3 essentially shows a semi-annual and a relatively strong 27 d variability. EOF4 contributes with only 0.4 % of the total estimated variability. Its shape is strongly non-zonal and reflects variations in longitudinal differences of the equatorial ionization anomaly. In the wavelet analysis, weak semi-annual and annual oscillations are visible. Note that the PC4 displays a possible long-term trend, which may indicate an effect of the secular change of the main magnetic field of the Earth. The oscillating structure of the EOF4 over the Atlantic resembles the results from numerical simulations by Cnossen and Richmond (2013).
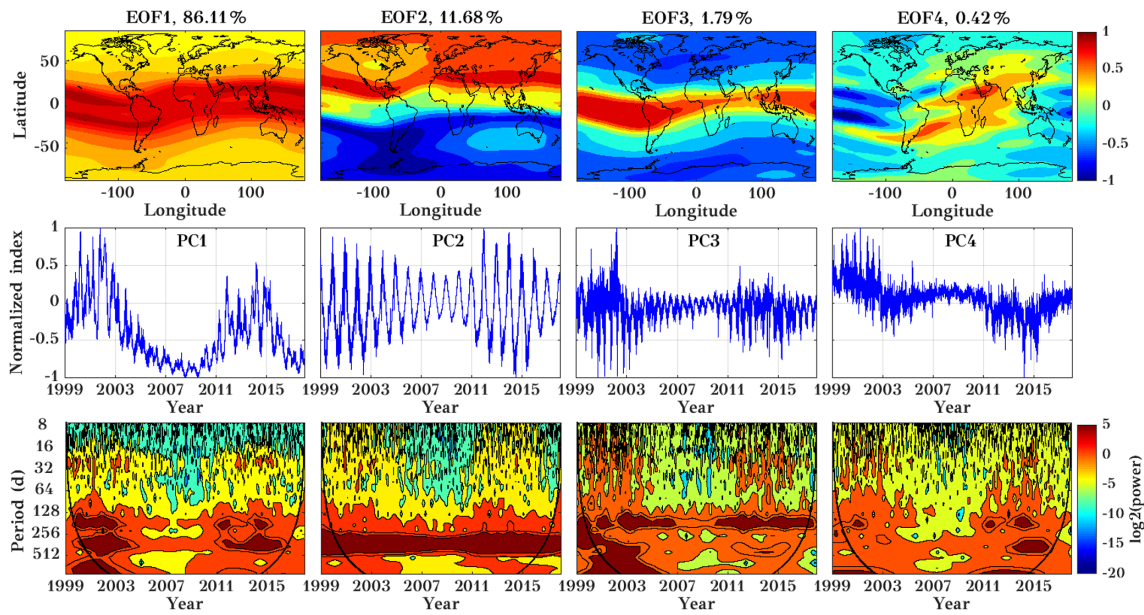
Figure 11. The first four EOFs (top row) of normalized TEC during the years 1999 to 2017, corresponding principal components (middle row), and their corresponding wavelet transform (bottom row, wavelet power in log2 scale). Please note that EOFs are dimensionless.

In summary, the first two components capture almost 98 % of the TEC variance, while the third and fourth components only contribute about 2 %. This is similar to results of Zhao et al. (2005), Anderson and Hawkins (2016), and Talaat and Zhu (2016), who reported that more than 95 % of the variance is explained by the first three EOFs.

In order to check the relation between solar proxies and geomagnetic parameters (daily Kp, Dst, and Ap indices) with PCs corresponding to EOFs, the wavelet cross-correlation and delay are shown in Fig. 12. In Fig. 12 the color indicates the maximum correlation coefficient, and the numerical values indicate the corresponding time delay in days. A strong correlation between PC1 and Mg II (F10.7) is observed with a coefficient of about 0.87 (0.8) and a time delay of 1 d (2 d). This represents the strong correlation between global TEC and solar variability as PC1 is associated with solar variability. The geomagnetic parameters are generally more loosely connected with ionospheric variability, indicating the relatively fast ionospheric storm reaction compared to the longer-lasting equatorial magnetic field depletion. PC3 shows a relatively strong correlation with the geomagnetic parameters, which indicates that this component (apart from the remaining part of solar variability not included in EOF1) captures the geomagnetic activity effect on TEC. Here the Kp and Ap indices show a positive correlation of about 0.6 with a delay of about 2 d. In comparison to this, a negative correlation of about 0.7 is observed in the Dst. Figure A4 in the Appendix shows the correlation between PCs and solar and geomagnetic proxies at zero lag. Furthermore, running correlations at interannual timescales, similar to Fig. 7 are

shown in Fig. A7 in the Appendix using PCs and solar and geomagnetic parameters.

To assess the variability on the timescale of the solar rotation period, we filtered the GTEC time series in a period range of 25 to 35 d using a digital bandpass filter. The filtered time series is then used to compute EOFs. Figure 13 shows the first four EOF components in the upper row and their corresponding wavelet transforms in the lower row. The first component captures almost 85.50 % of total variability, and it seems to be associated with solar activity. EOF1 shows high variability in the equatorial region. EOF2 captures 8.91 % of variability, and it is partly associated with hemispheric variability. EOF3 captures the variability of 4.92 %, which is not captured in the EOF2 component (in particular the hemispheric asymmetry). EOF2 does not show a clear hemispheric signal anymore, while EOF3 now does. The lower panels show the corresponding wavelet spectra of PCs. Wavelet analysis clearly shows the expected periodicity in the 16 to 32 d period in all the PCs, with a response to the 11-year solar cycle.

Furthermore, wavelet cross-correlation analysis has been performed to understand the relation between solar proxies and geomagnetic parameters (with PCs corresponding to EOFs of the filtered data, as shown in Fig. 13) and shown in Fig. 14 (Fig. A5 in the Appendix for zero lag). It shows a similar kind of result to in Fig. 12 in the case of PC1. PC2 and PC3 are associated with geomagnetic activity. As compared to Fig. 12, PC2 shows strong correlation with magnetic indices. So, the distribution of variance is different here. This is because the coupled low-latitude–high-latitude magnetically forced variability, which is mainly represented by PC3
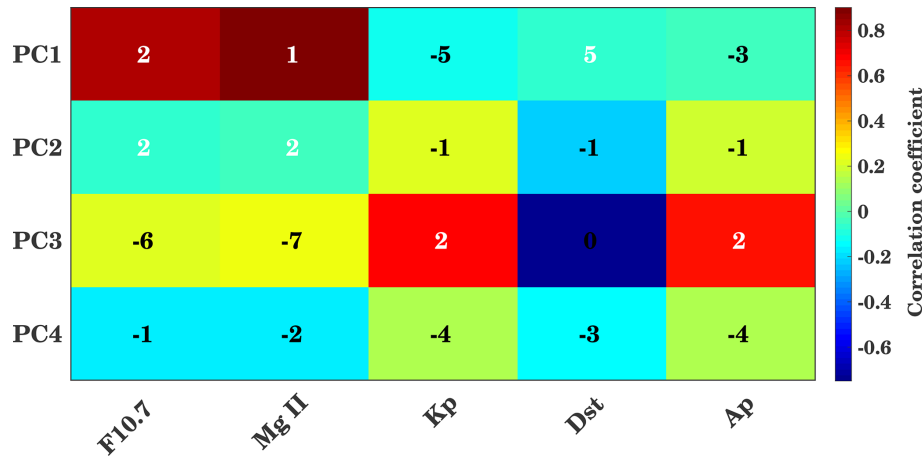
Figure 12. Correlation coefficients and time lag between the PCs and solar and geomagnetic proxies. Background colors show the maximum correlation coefficients, and the inserted numbers show the delay in days corresponding to maximum correlation.
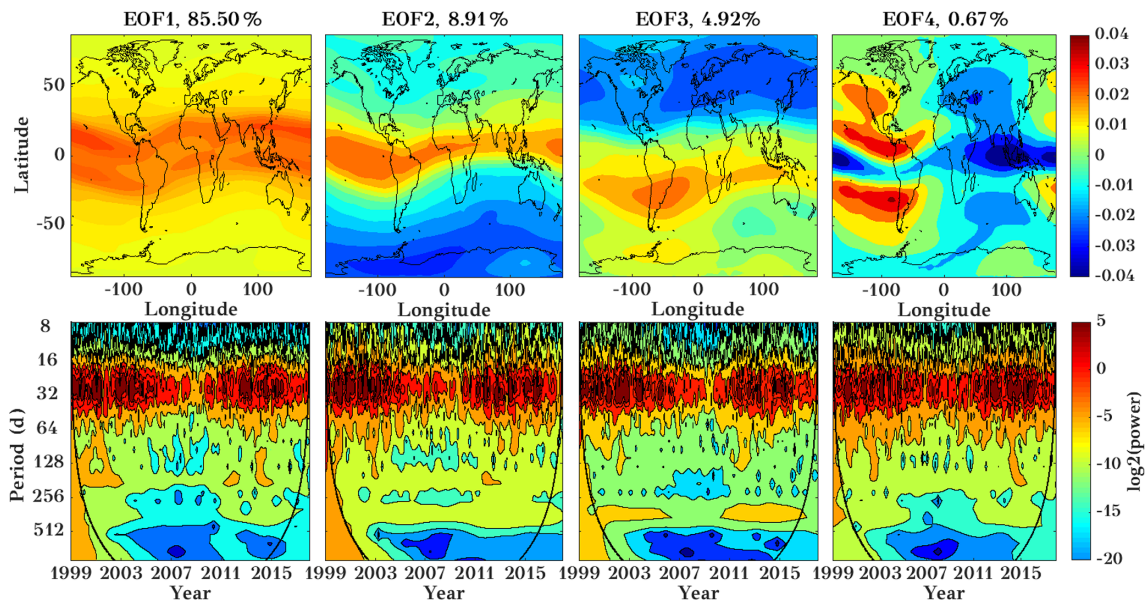

Figure 13. Spatial distribution map of first four EOFs (upper panels) of IGS TEC during the years 1999 to 2017, and their corresponding wavelet transform (lower panels, wavelet power in log2 scale) using a 25–35 d filtered dataset. The EOFs are dimensionless.

in the case of unfiltered data, is now distributed among PC2 and PC3 for the solar rotation period.

4 Conclusions

We have investigated the long-term ionospheric response during different solar activities, timescales, and spatial variations using 12 solar proxies (F10.7, F1.8, F3.2, F8, F15, F30, He II, Mg II index, Ly-α, Ca II K, daily SSA, and SSN) and 18 years (1999–2017) of IGS TEC data. The cross-wavelet and LSP methods were used to examine the oscillatory behavior. The cross-wavelet analysis represents the 16 to 32 d period in all the solar proxies and GTEC. The maximum cor-

relation with GTEC is observed between the He II index, Mg II index, and F30 in the period range of 16 to 32 d along with a time delay of about 1 d. Wavelet variance estimation suggests that GTEC variance is high for the 64 to 128 d interval followed by 16 to 32 d, while the F10.7 index is showing high variance for the 16 to 32 d interval.

Interannual variation of the cross-correlation analysis suggests that the correlation is varying with the solar activity. The most suitable proxy to represent the solar activity at the timescales of 16 to 32 and 32 to 64 d during low, middle, and high solar activity is He II. The Mg II index, Ly-α, and F30 may be placed at the second as these indices show a strong correlation with GTEC, but with some differences
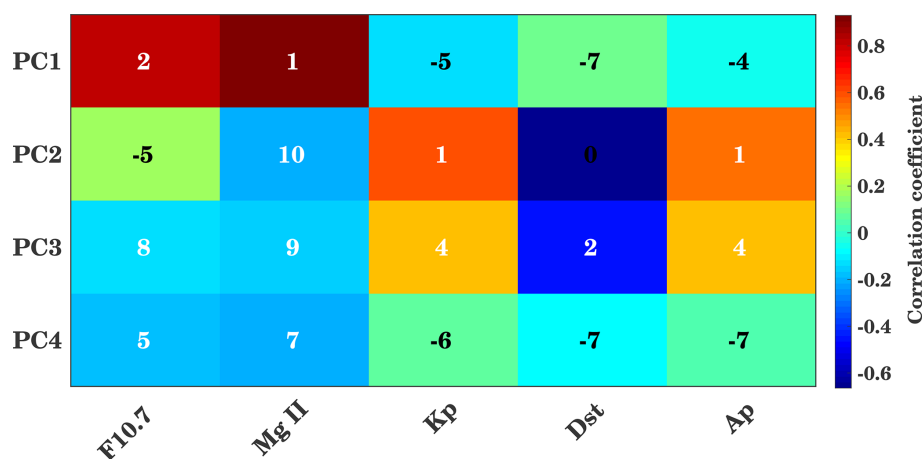
Figure 14. Maximum correlation coefficients and the time lag between the PCs and solar and magnetic proxies for the 25–35 d interval. Background colors show the maximum correlation coefficients, and the inserted numbers show the delay in days corresponding to maximum correlation.

between solar maximum and minimum. The F1.8 and daily SSA poorly represent the solar activity effect on TEC. The spatial distribution of cross-correlation and time was estimated using the Mg II index. The results show significant temporal and spatial variations. Stronger correlation is observed near the equatorial region with a time delay of about 1–2 d. The magnetospheric inputs probably strongly influence both high- and low-latitude regions, but with a different sign.

TEC datasets also have been decomposed using EOFs along with the principal component analysis method to signify the spatial and temporal variation. The first EOF component captures more than 86 % of the variability, and the first three EOF components explain 99 % of the variance. EOF analysis suggests that the first component is associated with the solar flux and the third EOF component captures the geomagnetic activity as well as the remaining part of EOF1. EOF2 captures 11 % of the total variability and demonstrates the hemispheric asymmetry.

Appendix A

Additional figures are shown in order to complete the presentation. Figure A1 is similar to Fig. 5 but shows the correlation between solar proxies and GTEC at zero lag at different timescales. Figure A2 shows the correlation at 16 to 32 d timescale between solar proxies and GTEC, similar to Fig. 9, but again at zero lag. Figure A3 is similar to Fig. 9 but shows the cross-correlation and delay at the timescale of 32 to 64 d. Figure A4 is similar to Fig. 12 and shows the correlation between PCs and solar and geomagnetic proxies, but at zero lag, while Fig. A5 shows the same for the 25–35 d interval. Running correlations at the intra-annual timescales, similar to Fig. 7 but also for different latitude ranges, are shown in Fig. A6. Figure A7 shows running cross-correlations between the PCs and different solar proxies and geomagnetic activity parameters.
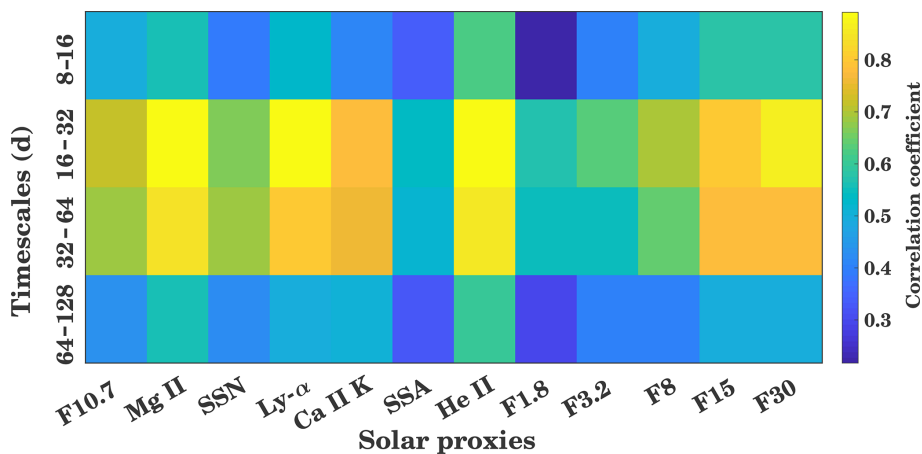

Figure A1. Wavelet cross-correlation sequence estimates for the maximal overlap discrete wavelet transform for GTEC and multiple solar proxies for different timescales (8 to 16, 16 to 32, 32 to 64, and 64 to 128 d). The colors represent the correlation coefficient at lag 0.
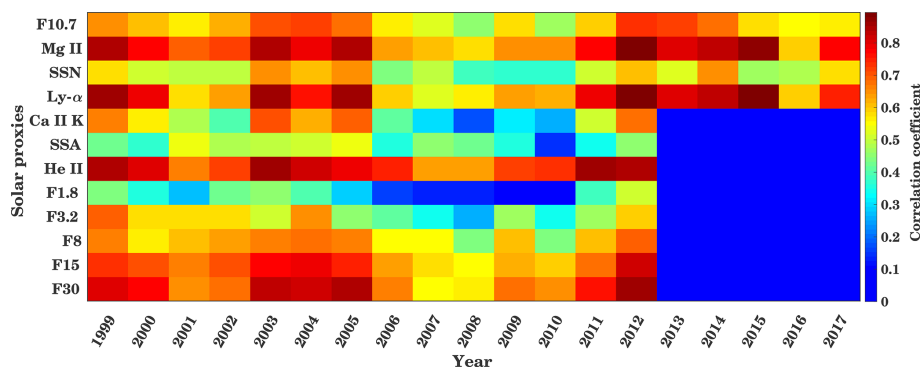

Figure A2. Correlation coefficient between GTEC and different solar proxies for the years 1999 to 2017 at the timescale of 16 to 32 d at lag 0.
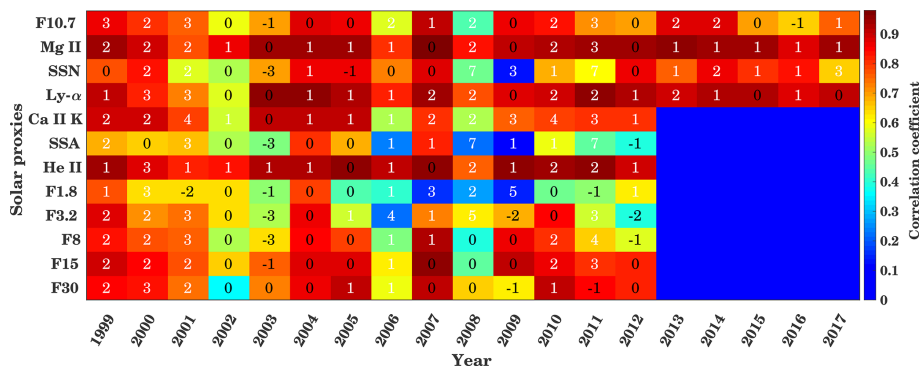
Figure A3. Cross-correlation and time delay between GTEC and different solar proxies for the years 1999 to 2017 at the timescale of 32 to 64 d. Background colors show the maximum correlation coefficients, and the inserted numbers show the delay in days corresponding to maximum correlation.
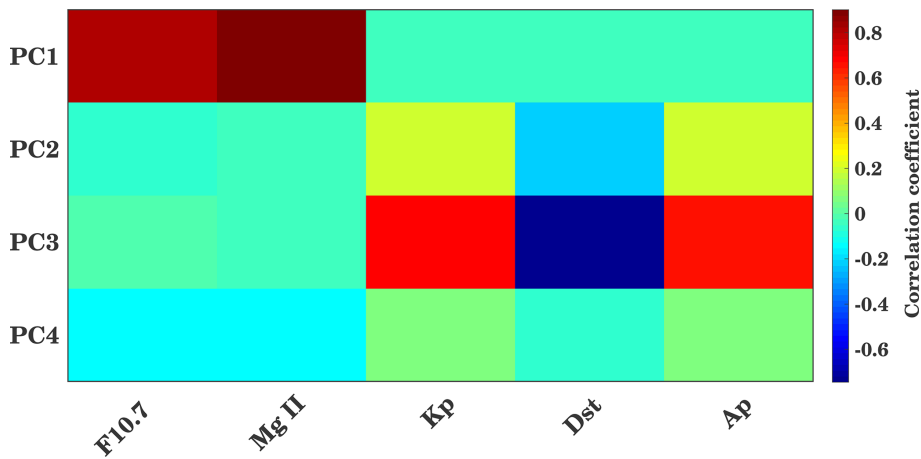

Figure A4. Correlation coefficients between the PCs and solar and geomagnetic proxies at lag 0.
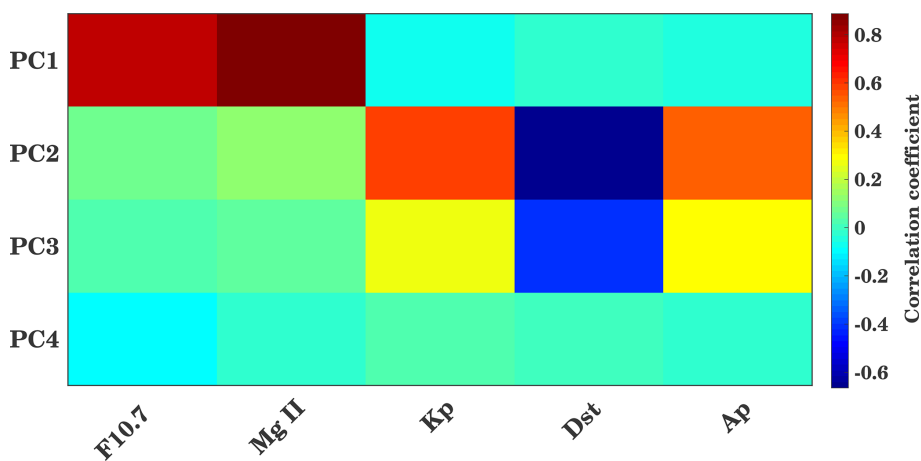

Figure A5. Correlation coefficients between the PCs and solar and magnetic proxies for the 25–35 d interval for zero lag.
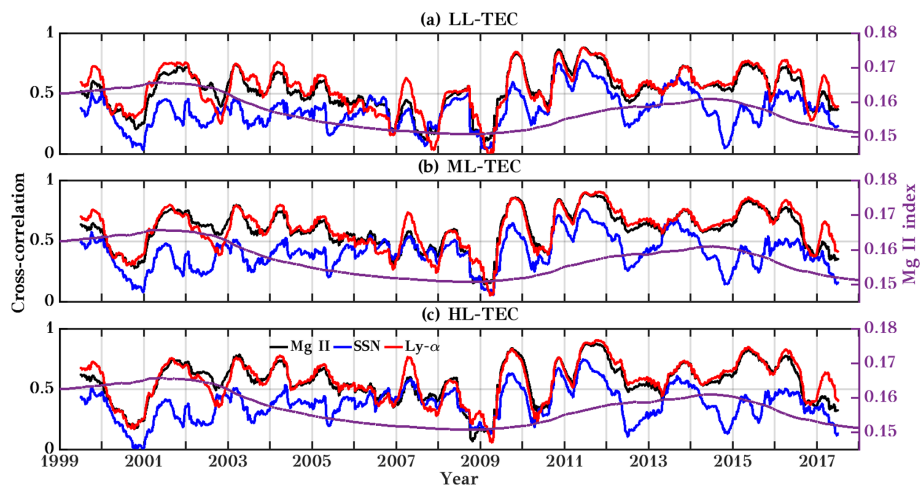
Figure A6. Running cross-correlation between the TEC and different solar proxies using a 365 d running window for LL, ML, and HL. The second y axis shows the 365 d running mean time series of the Mg II index. Here Mg II, SSN, and Ly-α are marked by black, blue, and red colors, respectively. Correlation coefficients between the PCs and solar and geomagnetic proxies at lag 0.
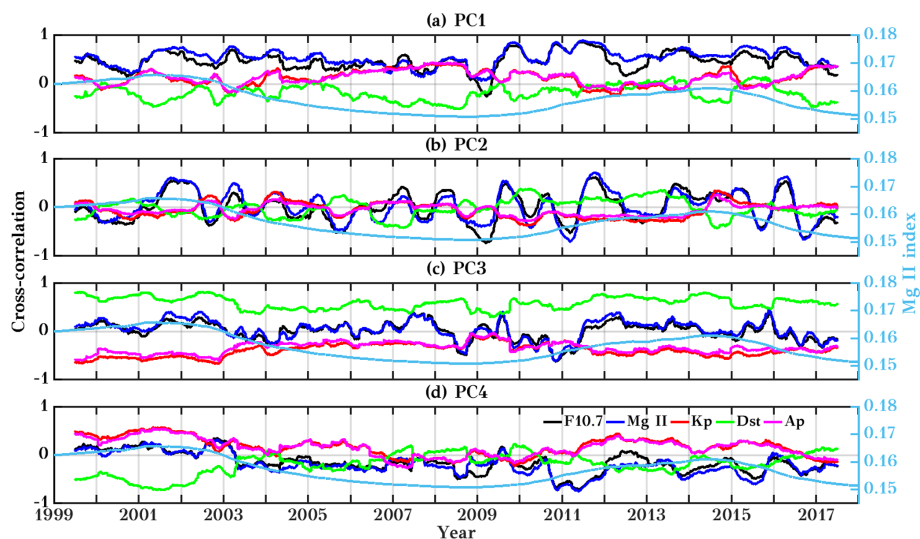

Figure A7. Running cross-correlation between the PCs and different solar proxies and geomagnetic activity parameters using a 365 d running window. The second y axis shows the 365 d running mean time series of the Mg II index. Here F10.7, Mg II, Kp, Dst, and Ap are marked by black, blue, red, green, and magenta colors, respectively.

References

Abdu, M. A.: Electrodynamics of ionospheric weather over low latitudes, Geosci. Lett., 3, 11, https://doi.org/10.1186/s40562-016-0043-6, 2016.

Afraimovich, E. L., Astafyeva, E. I., Oinats, A. V., Yasukevich, Yu. V., and Zhivetiev, I. V.: Global electron content: a new conception to track solar activity, Ann. Geophys., 26, 335–344, https://doi.org/10.5194/angeo-26-335-2008, 2008.

Anderson, P. C. and Hawkins, J. M.: Topside ionospheric response to solar EUV variability, J. Geophys. Res., 121, 1518–1529, https://doi.org/10.1002/2015ja021202, 2016.

BenMoussa, A., Gissot, S., Schühle, U., Zanna, G. D., Auchère, F., Mekaoui, S., Jones, A. R., Walton, D., Eyles, C. J., Thuillier, G., Seaton, D., Dammasch, I. E., Cessateur, G., Meftah, M., Andretta, V., Berghmans, D., Bewsher, D., Bolsée, D., Bradley, L., Brown, D. S., Chamberlin, P. C., Dewitte, S., Didkovsky, L. V., Dominique, M., Eparvier, F. G., Foujols, T., Gillotay, D., Giordanengo, B., Halain, J. P., Hock, R. A., Irbah, A., Jeppesen, C., Judge, D. L., Kretzschmar, M., McMullin, D. R., Nicula, B., Schmutz, W., Ucker, G., Wieman, S., Woodraska, D., and Woods, T. N.: On-Orbit Degradation of Solar Instruments, Sol.

Phys., 288, 389–434, https://doi.org/10.1007/s11207-013-0290-z, 2013.

Björnsson, H. and Venegas, S.: A manual for EOF and SVD analyses of climatic data, CCGCR Report, 97, 112–134, 1997.

CDDIS: GNSS Atmospheric Products, available at: http://cddis.nasa.gov/Data_and_Derived_Products/GNSS/atmospheric_products.html, last accessed: 15 August 2018.

Chen, Y., Liu, L., and Wan, W.: The discrepancy in solar EUV-proxy correlations on solar cycle and solar rotation timescales and its manifestation in the ionosphere, J. Geophys. Res., 117, A03313, https://doi.org/10.1029/2011ja017224, 2012.

Chowdhury, P., Khan, M., and Ray, P. C.: Intermediate-term periodicities in sunspot areas during solar cycles 22 and 23, Mon. Not. Roy. Astron. Soc., 392, 1159–1180, https://doi.org/10.1111/j.1365-2966.2008.14117.x, 2009.

Chowdhury, P., Choudhary, D. P., Gosain, S., and Moon, Y.-J.: Short-term periodicities in interplanetary, geomagnetic and solar phenomena during solar cycle 24, Astrophys. Space Sci., 356, 7–18, https://doi.org/10.1007/s10509-014-2188-0, 2015.

Cnossen, I. and Richmond, A. D.: Changes in the Earth's magnetic field over the past century: Effects on the ionosphere-thermosphere system and solar quiet (Sq) magnetic variation, J. Geophys. Res., 118, 849–858, https://doi.org/10.1029/2012ja018447, 2013.

Dewolfe, A. W., Wilson, A., Lindholm, D. M., Pankratz, C. K., Snow, M. A., and Woods, T. N.: Solar Irradiance Data Products at the LASP Interactive Solar Irradiance Datacenter (LISIRD), AGU Fall Meeting Abstracts, GC21B-0881, San Francisco, California, 13–17 December 2010.

Dudok de Wit, T.: A method for filling gaps in solar irradiance and solar proxy data, Astron. Astrophys., 533, A29, https://doi.org/10.1051/0004-6361/201117024, 2011.

Dudok de Wit, T., Bruinsma, S., and Shibasaki, K.: Synoptic radio observations as proxies for upper atmosphere modelling, J. Space Weather Space Clim., 4, A06, https://doi.org/10.1051/swsc/2014003, 2014.

Emmert, J. T., Mannucci, A. J., McDonald, S. E., and Vergados, P.: Attribution of interminimum changes in global and hemispheric total electron content, J. Geophys. Res., 122, 2424–2439, https://doi.org/10.1002/2016ja023680, 2017.

Ercha, A., Zhang, D., Ridley, A. J., Xiao, Z., and Hao, Y.: A global model: Empirical orthogonal function analysis of total electron content 1999-2009 data, J. Geophys. Res., 117, A03328, https://doi.org/10.1029/2011ja017238, 2012.

Floyd, L., Newmark, J., Cook, J., Herring, L., and McMullin, D.: Solar EUV and UV spectral irradiances and solar indices, J. Atmos. Sol.-Terr. Phy., 67, 3–15, https://doi.org/10.1016/j.jastp.2004.07.013, 2005.

Forbes, J. M., Palo, S. E., and Zhang, X.: Variability of the ionosphere, J. Atmos. Sol.-Terr. Phy., 62, 685–693, https://doi.org/10.1016/s1364-6826(00)00029-8, 2000.

Grinsted, A., Moore, J. C., and Jevrejeva, S.: Application of the cross wavelet transform and wavelet coherence to geophysical time series, Nonlin. Processes Geophys., 11, 561–566, https://doi.org/10.5194/npg-11-561-2004, 2004.

Guo, J., Li, W., Liu, X., Kong, Q., Zhao, C., and Guo, B.: Temporal-Spatial Variation of Global GPS-Derived Total Electron Content, 1999–2013, PloS one, 10, e0133378, https://doi.org/10.1371/journal.pone.0133378, 2015.

Haberreiter, M., Schöll, M., Dudok de Wit, T., Kretzschmar, M., Misios, S., Tourpali, K., and Schmutz, W.: A new observational solar irradiance composite, J. Geophys. Res., 122, 5910–5930, https://doi.org/10.1002/2016ja023492, 2017.

Hernández-Pajares, M., Juan, J. M., Sanz, J., Orus, R., Garcia-Rigo, A., Feltens, J., Komjathy, A., Schaer, S. C., and Krankowski, A.: The IGS VTEC maps: a reliable source of ionospheric information since 1998, J. Geodyn., 83, 263–275, https://doi.org/10.1007/s00190-008-0266-1, 2009.

Hocke, K.: Oscillations of global mean TEC, J. Geophys. Res., 113, A04302, https://doi.org/10.1029/2007ja012798, 2008.

IUP: Bremen composite Mg II index, available at: http://www.iup.uni-bremen.de/UVSAT/Datasets/mgii, last access: 15 August 2018.

Jacobi, C., Jakowski, N., Schmidtke, G., and Woods, T. N.: Delayed response of the global total electron content to solar EUV variations, Adv. Radio Sci., 14, 175–180, https://doi.org/10.5194/ars-14-175-2016, 2016.

Jakowski, N., Fichtelmann, B., and Jungstand, A.: Solar activity control of ionospheric and thermospheric processes, J. Atmos. Terr. Phys., 53, 1125–1130, https://doi.org/10.1016/0021-9169(91)90061-b, 1991.

Jakowski, N., Hocke, K., Schlüter, S., and Heise, S.: Space weather effects detected by GPS based TEC monitoring, in: Workshop on Space Weather, WPP-155, ESTEC, Noordwijk, pp. 241–244, 1999.

Jakowski, N., Heise, S., Wehrenpfennig, A., Schlüter, S., and Reimer, R.: GPS/GLONASS-based TEC measurements as a contributor for space weather forecast, J. Atmos. Terr. Phys., 64, 729–735, https://doi.org/10.1016/s1364-6826(02)00034-2, 2002.

Kilcik, A., Ozguc, A., Yurchyshyn, V., and Rozelot, J. P.: Sunspot Count Periodicities in Different Zurich Sunspot Group Classes Since 1986, Sol. Phys., 289, 4365–4376, https://doi.org/10.1007/s11207-014-0580-0, 2014.

Kilcik, A., Yurchyshyn, V., Clette, F., Ozguc, A., and Rozelot, J.-P.: Active Latitude Oscillations Observed on the Sun, Sol. Phys., 291, 1077–1087, https://doi.org/10.1007/s11207-016-0890-5, 2016.

Kilcik, A., Yurchyshyn, V., Donmez, B., Obridko, V. N., Ozguc, A., and Rozelot, J. P.: Temporal and Periodic Variations of Sunspot Counts in Flaring and Non-Flaring Active Regions, Sol. Phys., 293, https://doi.org/10.1007/s11207-018-1285-6, 2018.

King, J. H. and Papitashvili, N. E.: Solar wind spatial scales in and comparisons of hourly Wind and ACE plasma and magnetic field data, J. Geophys. Res., 110, A02104, https://doi.org/10.1029/2004ja010649, 2005.

Knížová, P. K., Mošna, Z., Kouba, D., Potužníková, K., and Boška, J.: Influence of meteorological systems on the ionosphere over Europe, J. Atmos. Sol.-Terr. Phy., 136, 244–250, https://doi.org/10.1016/j.jastp.2015.07.017, 2015.

Kutiev, I., Otsuka, Y., Pancheva, D., and Heelis, R.: Response of low-latitude ionosphere to medium-term changes of solar and geomagnetic activity, J. Geophys. Res., 117, A08330, https://doi.org/10.1029/2012ja017641, 2012.

Kutiev, I., Tsagouri, I., Perrone, L., Pancheva, D., Mukhtarov, P., Mikhailov, A., Lastovicka, J., Jakowski, N., Buresova, D., Blanch, E., Andonov, B., Altadill, D., Magdaleno, S., Parisi, M., and Torta, J. M.: Solar activity impact on the Earth's upper atmosphere, J. Space Weather Space, 3, A06, https://doi.org/10.1051/swsc/2013028, 2013.

LASP: LASP Interactive Solar Irradiance Data Center, available at: http://lasp.colorado.edu/lisird/data/noaa_radio_flux/, last access: 15 August 2018.

Lean, J. L., White, O. R., Livingston, W. C., and Picone, J. M.: Variability of a composite chromospheric irradiance index during the 11-year activity cycle and over longer time periods, J. Geophys. Res., 106, 10645–10658, https://doi.org/10.1029/2000ja000340, 2001.

Lean, J. L., Meier, R. R., Picone, J. M., Sassi, F., Emmert, J. T., and Richards, P. G.: Ionospheric total electron content: Spatial patterns of variability, J. Geophys. Res., 121, 10367–10402, https://doi.org/10.1002/2016ja023210, 2016.

Lee, C.-K., Han, S.-C., Bilitza, D., and Seo, K.-W.: Global characteristics of the correlation and time lag between solar and ionospheric parameters in the 27-day period, J. Atmos. Sol.-Terr. Phy., 77, 219–224, https://doi.org/10.1016/j.jastp.2012.01.010, 2012.

Liu, J. Y., Chen, Y. I., and Lin, J. S.: Statistical investigation of the saturation effect in the ionospheric foF2 versus sunspot, solar radio noise, and solar EUV radiation, J. Geophys. Res., 108, 1067, https://doi.org/10.1029/2001ja007543, 2003.

Liu, L. and Chen, Y.: Statistical analysis of solar activity variations of total electron content derived at Jet Propulsion Laboratory from GPS observations, J. Geophys. Res., 114, A10311, https://doi.org/10.1029/2009ja014533, 2009.

Liu, L., Wan, W., Ning, B., Pirog, O. M., and Kurkin, V. I.: Solar activity variations of the ionospheric peak electron density, J. Geophys. Res., 111, A08304, https://doi.org/10.1029/2006ja011598, 2006.

Lomb, N. R.: Least-squares frequency analysis of unequally spaced data, Astrophys. Space Sci., 39, 447–462, https://doi.org/10.1007/bf00648343, 1976.

Lou, Y.-Q., Wang, Y.-M., Fan, Z., Wang, S., and Wang, J. X.: Periodicities in solar coronal mass ejections, Mon. Not. R. Astron. Soc., 345, 809–818, https://doi.org/10.1046/j.1365-8711.2003.06993.x, 2003.

Mallat, S. G.: A theory for multiresolution signal decomposition: the wavelet representation, IEEE T. Pattern Anal., 7, 674–693, 1989.

Maruyama, T.: Solar proxies pertaining to empirical ionospheric total electron content models, J. Geophys. Res., 115, A04306, https://doi.org/10.1029/2009ja014890, 2010.

Matsuo, T., Fedrizzi, M., Fuller-Rowell, T. J., and Codrescu, M. V.: Data assimilation of thermospheric mass density, Space Weather, 10, S05002, https://doi.org/10.1029/2012sw000773, 2012.

Min, K., Park, J., Kim, H., Kim, V., Kil, H., Lee, J., Rentz, S., Lühr, H., and Paxton, L.: The 27-day modulation of the low-latitude ionosphere during a solar maximum, J. Geophys. Res., 114, A04317, https://doi.org/10.1029/2008ja013881, 2009.

Nikutowski, B., Brunner, R., Erhardt, C., Knecht, S., and Schmidtke, G.: Distinct EUV minimum of the solar irradiance (16–40 nm) observed by SolACES spectrometers onboard the International Space Station (ISS) in August/September 2009, Adv. Space Res., 48, 899–903, https://doi.org/10.1016/j.asr.2011.05.002, 2011.

Noll, C. E.: The crustal dynamics data information system: A resource to support scientific analysis us-

ing space geodesy, Adv. Space Res., 45, 1421–1440, https://doi.org/10.1016/j.asr.2010.01.018, 2010.

OMNIWeb: OMNIWeb Plus database, available at: http://omniweb. gsfc.nasa.gov/, last access: 15 August 2018.

Pancheva, D., Schminder, R., and Laštovička, J.: 27-day fluctuations in the ionospheric D-region, J. Atmos. Terr. Phys., 53, 1145–1150, https://doi.org/10.1016/0021-9169(91)90064-e, 1991.

Percival, D. B. and Walden, A. T.: Wavelet methods for time series analysis, Cambridge University Press, Cambridge, UK, 2000.

Preisendorfer, R.: Principal component analysis in meteorology and oceanography, Elsevier Sci. Publ., 17, 1–425, 1988.

Ren, D., Lei, J., Wang, W., Burns, A., Luan, X., and Dou, X.: Does the Peak Response of the Ionospheric F2 Region Plasma Lag the Peak of 27-Day Solar Flux Variation by Multiple Days?, J. Geophys. Res., 123, 7906–7916, https://doi.org/10.1029/2018ja025835, 2018.

Rich, F. J., Sultan, P. J., and Bruke, W. J.: The 27-day variations of plasma densities and temperatures in the topside ionosphere, J. Geophys. Res., 108, 1297, https://doi.org/10.1029/2002ja009731, 2003.

Scargle, J. D.: Studies in astronomical time series analysis. II – Statistical aspects of spectral analysis of unevenly spaced data, Astrophys. J., 263, 835, https://doi.org/10.1086/160554, 1982.

Schmidtke, G.: EUV indices for solar-terrestrial relations, Geophys. Res. Lett., 3, 573–576, https://doi.org/10.1029/gl003i010p00573, 1976.

Schmidtke, G., Nikutowski, B., Jacobi, C., Brunner, R., Erhardt, C., Knecht, S., Scherle, J., and Schlagenhauf, J.: Solar EUV Irradiance Measurements by the Auto-Calibrating EUV Spectrometers (SolACES) Aboard the International Space Station (ISS), Sol. Phys., 289, 1863–1883, https://doi.org/10.1007/s11207-013-0430-5, 2014.

Schmidtke, G., Avakyan, S., Berdermann, J., Bothmer, V., Cessateur, G., Ciraolo, L., Didkovsky, L., de Wit, T. D., Eparvier, F., Gottwald, A., Haberreiter, M., Hammer, R., Jacobi, C., Jakowski, N., Kretzschmar, M., Lilensten, J., Pfeifer, M., Radicella, S., Schäfer, R., Schmidt, W., Solomon, S., Thuillier, G., Tobiska, W., Wieman, S., and Woods, T.: Where does the Thermospheric Ionospheric GEospheric Research (TIGER) Program go?, Adv. Space Res., 56, 1547–1577, https://doi.org/10.1016/j.asr.2015.07.043, 2015.

Schmölter, E., Berdermann, J., Jakowski, N., Jacobi, C., and Vaishnav, R.: Delayed response of the ionosphere to solar EUV variability, Adv. Radio Sci., 16, 149–155, https://doi.org/10.5194/ars-16-149-2018, 2018.

Schöll, M., Dudok de Wit, T., Kretzschmar, M., and Haberreiter, M.: Making of a solar spectral irradiance dataset I: observations, uncertainties, and methods, J. Space Weather Space Clim., 6, A14, https://doi.org/10.1051/swsc/2016007, 2016.

SOLID: SSI and Proxy Datasets, available at: http://projects. pmodwrc.ch/solid/, last access: 15 August 2018.

Talaat, E. R. and Zhu, X.: Spatial and temporal variation of total electron content as revealed by principal component analysis, Ann. Geophys., 34, 1109–1117, https://doi.org/10.5194/angeo-34-1109-2016, 2016.

Tapping, K. F.: Recent solar radio astronomy at centimeter wavelengths: The temporal variability of the 10.7-cm flux, J. Geophys. Res., 92, 829, https://doi.org/10.1029/jd092id01p00829, 1987.

Tsurutani, B. T., Verkhoglyadova, O. P., Mannucci, A. J., Lakhina, G. S., Li, G., and Zank, G. P.: A brief review of "solar flare effects" on the ionosphere, Radio Sci., 44, 1–14, https://doi.org/10.1029/2008rs004029, 2009.

Unglaub, C., Jacobi, C., Schmidtke, G., Nikutowski, B., and Brunner, R.: EUV-TEC proxy to describe ionospheric variability using satellite-borne solar EUV measurements: First results, Adv. Space Res., 47, 1578–1584, https://doi.org/10.1016/j.asr.2010.12.014, 2011.

Vaishnav, R., Jacobi, C., Berdermann, J., Codrescu, M., and Schmölter, E.: Ionospheric response during low and high solar activity, Rep. Inst. Meteorol. Univ. Leipzig, 56, 1–10, 2018a.

Vaishnav, R., Jacobi, C., Berdermann, J., Schmölter, E., and Codrescu, M.: Ionospheric response to solar EUV variations: Preliminary results, Adv. Radio Sci., 16, 157–165, https://doi.org/10.5194/ars-16-157-2018, 2018b.

Verkhoglyadova, O. P., Tsurutani, B. T., Mannucci, A. J., Mlynczak, M. G., Hunt, L. A., and Runge, T.: Variability of ionospheric TEC during solar and geomagnetic minima (2008 and 2009): external high speed stream drivers, Ann. Geophys., 31, 263–276, https://doi.org/10.5194/angeo-31-263-2013, 2013.

Wolf, R.: Mittheilungen über die Sonnenflecken, Vierteljahresschrift der Naturforschenden Gesellschaft in Zürich, 1, 151–161, 1856.

Woods, T., Bailey, S., Eparvier, F., Lawrence, G., Lean, J., McClintock, B., Roble, R., Rottman, G., Solomon, S., Tobiska, W., and White, O.: TIMED Solar EUV experiment, Phys. Chem. Earth Pt. C, 25, 393–396, https://doi.org/10.1016/s1464-1917(00)00040-4, 2000.

Zhao, B., Wan, W., Liu, L., Yue, X., and Venkatraman, S.: Statistical characteristics of the total ion density in the topside ionosphere during the period 1996-2004 using empirical orthogonal function (EOF) analysis, Ann. Geophys., 23, 3615–3631, https://doi.org/10.5194/angeo-23-3615-2005, 2005.

Zurbuchen, T. H., von Steiger, R., Gruesbeck, J., Landi, E., Lepri, S. T., Zhao, L., and Hansteen, V.: Sources of Solar Wind at Solar Minimum: Constraints from Composition Data, Space Sci. Rev., 172, 41–55, https://doi.org/10.1007/s11214-012-9881-5, 2012.

4 Paper 3: Comparison between CTIPe model simulations and satellite measurements

In this paper, the TEC provided by the IGS, and the CTIPe model simulated TEC have been used to investigate the delayed ionospheric response to the solar EUV flux measured by the SDO satellite and its trend from 2011 to 2013.

This study aims to analyze the ionospheric TEC variations both in the Northern and at Southern Hemisphere during moderate solar activity during the inclining phase of solar cycle 24 (2011-2013). We use GNSS data from 70°S to 70°N latitude at 15°E longitude due to better coverage with ground measurements in TEC maps. The observed TEC is compared with the model-simulated TEC using different solar EUV flux models. The ionospheric delay against the solar EUV flux has been investigated by Schmölter et al. (2020) using TEC observations. Therefore, the focus of the present study is laid on the ability to reproduce the ionospheric delay with the CTIPe model at 15°E.

Furthermore, the observed TEC is compared with the modeled TEC simulated with the SOLAR2000 and EUVAC flux models within CTIPe over Northern and Southern Hemispheric grid points. The analysis suggests that TEC, simulated using the SOLAR2000 flux model, overestimates the observed TEC, which is not the case when using the EUVAC flux model.

Our main contributions to scientific understanding of ionospheric delay:

- The periodicity estimates over the low, mid, and high latitudes show that the 16-32 d periodicity was dominant in 2012. Compared to the periodicity observed in model-simulated TEC, the 64-128 d periodicity was absent in the observations at all latitudes considered.

- When comparing TEC with the F10.7 index, the correlation in 2011 and 2013 is higher over Southern Hemisphere than over Northern Hemisphere, i.e., there is a hemispheric asymmetry. A similar characteristic was observed by Romero-Hernandez et al. (2018). The lowest correlation is observed in 2012.

- The ionospheric delay was investigated using the modeled and observed TEC against the solar EUV flux. The ionospheric delay estimated with the model-simulated TEC is in good agreement with the delay estimated for the observed TEC. The average delay for the observed (modeled) TEC is about 17 (16) h. The study confirms the capabilities of the model to reproduce the delayed ionospheric response against the solar EUV flux. These results are in close agreement with Schmölter et al. (2020).

- The average difference between the northern and southern hemispheric delay estimated for observed (modeled) TEC is about 1 (2) h. The average delay is higher in the Northern Hemisphere than in the Southern Hemisphere.

- In addition, the observed TEC is compared with the modeled TEC simulated with the SOLAR2000 and EUVAC flux models within CTIPe at the northern and southern hemispheric grid points. The analysis shows that TEC, simulated with the SOLAR2000 flux model, overestimates the observed TEC, which is not the case when using the EUVAC flux model. The large bias observed in the physics- based model is mainly due to the solar EUV flux input and grid resolution. Our results indicate that the model needs to be further improved with respect to the solar flux input to further reduce the presented bias to TEC measurements.

The analysis has a few limitations that need to be considered in future research. Our analysis suggests that there is a large bias in the physics-based model, mainly due to the input of the solar EUV flux and the grid resolution. Therefore, the model needs to be further improved with respect to the solar flux input to further reduce the observed deviation from the TEC measurements.

This paper, **Vaishnav et al., 2021a**, is committed to the precise estimation of the ionospheric delayed response using the modeled and observed TEC versus solar EUV flux.

Research paper

[Vaishnav et al., 2021a] Vaishnav, R., Schmölter, E., Jacobi, C., Berdermann, J., and Codrescu, M. (2021). Ionospheric response to solar extreme ultraviolet radiation variations: comparison based on CTIPe model simulations and satellite measurements, Annales Geophysicae, 39, 341–355, https://doi.org/10.5194/angeo-39-341-2021.

Author contributions statement

The doctoral student performed the following tasks independently for this paper: Conceptualizing the approach, analyzing the data together with E. Schmölter, compiling and creating graphs, perform CTIPe model run, interpretation and conclusion, and writing the first draft of the paper.

Annales
Geophysicae

Ionospheric response to solar extreme ultraviolet radiation variations: comparison based on CTIPe model simulations and satellite measurements

Rajesh Vaishnav[1], **Erik Schmölter**[2], **Christoph Jacobi**[1], **Jens Berdermann**[2], and **Mihail Codrescu**[3]

[1]Leipzig Institute for Meteorology, Universität Leipzig, Stephanstr. 3, 04103 Leipzig, Germany
[2]German Aerospace Center, Kalkhorstweg 53, 17235 Neustrelitz, Germany
[3]Space Weather Prediction Centre, National Oceanic and Atmospheric Administration, Boulder, Colorado, USA

Correspondence: Rajesh Vaishnav (rajesh_ishwardas.vaishnav@uni-leipzig.de)

Abstract. The ionospheric total electron content (TEC) provided by the International GNSS Service (IGS) and the TEC simulated by the Coupled Thermosphere Ionosphere Plasmasphere Electrodynamics (CTIPe) model have been used to investigate the delayed ionospheric response against solar flux and its trend during the years 2011 to 2013. The analysis of the distinct low-latitude and midlatitude TEC response over 15° E shows a better correlation of observed TEC and the solar radio flux index F10.7 in the Southern Hemisphere compared to the Northern Hemisphere. Thus, a significant hemispheric asymmetry is observed.

The ionospheric delay estimated using model-simulated TEC is in good agreement with the delay estimated for observed TEC against the flux measured by the Solar Dynamics Observatory (SDO) extreme ultraviolet (EUV) Variability Experiment (EVE). The average delay for the observed (modeled) TEC is 17(16) h. The average delay calculated for observed and modeled TEC is 1 and 2 h longer in the Southern Hemisphere compared to the Northern Hemisphere.

Furthermore, the observed TEC is compared with the modeled TEC simulated using the SOLAR2000 and EUVAC flux models within CTIPe over northern and southern hemispheric grid points. The analysis suggests that TEC simulated using the SOLAR2000 flux model overestimates the observed TEC, which is not the case when using the EUVAC flux model.

1 Introduction

The ionospheric day-to-day variations are mainly controlled by fluctuations of solar extreme ultraviolet/ultraviolet (EUV/UV) radiation responsible for photoionization and photo-dissociation processes, lower atmospheric forcing, and space weather events such as geomagnetic storms. During geomagnetically and meteorologically quiet conditions, the electron density gradually increases after sunrise, with a maximum around 14:00 LT due to photochemical processes, and starts decreasing thereafter due to the combined effect of production and strong recombination, continuing after sunset due to recombination processes.

The solar radiation flux varies at different timescales, including the diurnal cycle, the 27 d solar rotation period, and the prominent 11-year solar cycle. This results in corresponding variations in composition and dynamics of the thermosphere–ionosphere (T–I) system (Hedin, 1984). The T–I system is highly variable with location and time, depending on the solar activity and geomagnetic disturbances.

The photoionization processes in the ionosphere cause different variations, including short-term variability at the timescale of the 27 d solar rotation or seasonal variations. Past studies on the effect of solar radiation variations at different timescales have been based on the total electron content (TEC, frequently given in TECU; 1 TECU= 10^{16} electrons m^{-2}), peak electron density (NmF2, cm^{-3}), and the corresponding height (HmF2, km) (e.g., Jakowski et al., 1991; Afraimovich et al., 2008; Lee et al., 2012; Jacobi

et al., 2016; Schmölter et al., 2018, 2020; Vaishnav et al., 2018, 2019; Ren et al., 2018, and references therein).

The annual contributions to the mean TEC variability have a stronger impact on the Southern Hemisphere, whereas the semi-annual contributions have similar phase and amplitude at conjugate points, suggesting close coupling between the ionosphere and thermosphere (Liu et al., 2009). Mendillo et al. (2002) suggested that both annual and semi-annual variations of NmF2 are largely caused by changes in the neutral composition, which are driven by the global thermospheric circulation.

Solar proxies are frequently used to represent the solar activity. Among them are the F10.7 index, the Mg-II index, and the He-II index. Furthermore, attempts have been made to determine simple proxies for global TEC variability based on these indices (e.g., Unglaub et al., 2011). These proxies have been compared to the ionospheric parameters at the timescale of the 27 d solar rotation. An ionospheric delay of about 1–2 d has been reported (e.g., Jakowski et al., 1991; Jacobi et al., 2016). Using a more precise and higher temporal resolution solar flux, an ionospheric delay of about 17–19 h has been reported by Schmölter et al. (2018). The spatial and seasonal effects on the ionospheric delay have been further investigated in detail by Schmölter et al. (2020) using European and Australian locations. Their study highlighted the role of geomagnetic activity in the ionospheric delay.

To investigate the process associated with the ionospheric delay, Jakowski et al. (1991) used a one-dimensional numerical model between 100 and 250 km altitude with simplifying assumptions. They suggested that a delay of approximately 2 d arises in atomic oxygen at 180 km due to photodissociation and transport processes. This hypothesis has yet to be confirmed with comprehensive ionospheric models such as CTIPe (Coupled Thermosphere Ionosphere Plasmasphere Electrodynamics). Ren et al. (2018) investigated the ionospheric delay using observations and modeling. They emphasized the role of the $[O]/[N_2]$ ratio in the ionospheric delay. Vaishnav et al. (2018) suggested the possible role of transport processes in the ionospheric delay.

During the past decades, more improved physics-based T–I models have been developed which are able to characterize ionospheric dynamics. Among them are the Coupled Thermosphere Ionosphere Plasmasphere Electrodynamics model (CTIPe; Fuller-Rowell and Rees, 1983; Codrescu et al., 2012), the Thermosphere–Ionosphere–Electrodynamics General Circulation Model (TIE-GCM; Richmond et al., 1992), and the Global Ionosphere Thermosphere Model (GITM; Ridley et al., 2006). Furthermore, some extended Earth system models like WACCM-X (Liu et al., 2018) and the Ground-to-topside model of Atmosphere and Ionosphere for Aeronomy (GAIA; Jin et al., 2012; Liu et al., 2020) include T–I dynamics. Based on the results of the T–I model, an ionospheric lag against variations of the solar EUV could be identified, whereby the EUV entry in the

model was represented by the F10.7 index (Ren et al., 2018; Vaishnav et al., 2018).

The most commonly used solar proxy for ionizing irradiance is the solar radio flux at 10.7 cm (F10.7 index, given in solar flux units (sfu); $1\,\mathrm{sfu} = 10^{-22}\,\mathrm{Wm^{-2}\,Hz^{-1}}$) (Tapping, 1987). Most of the T–I models use a modified F10.7 index (e.g., the average of daily and 41 or 81 d averages) to calculate the model EUV spectra based on reference spectra. Several authors have reported that a modified F10.7 index, which includes both short-term and long-term variability, is a better proxy for ionizing irradiance than F10.7 directly (Richards et al., 1994). There are several empirical models available, such as the SOLAR2000 (Tobiska et al., 2000) and EUVAC flux model (Richards et al., 1994), to calculate the irradiance.

Profiles of the delayed ionospheric response dependent on latitude have been calculated in previous studies (Lee et al., 2012; Ren et al., 2018), and the influence of seasonal variations and geomagnetic activity on both hemispheres has also been characterized (Schmölter et al., 2020). The complexity of the seasonal variations and associated anomalies has been investigated in other studies for ionospheric parameters like TEC (Romero-Hernandez et al., 2018). Such seasonal anomalies were observed in the F2 region associated with higher electron density in winter than in summer during daytime (the so-called winter or seasonal anomaly), during equinoxes than during solstices (semi-annual anomaly), and in December than in June (annual or non seasonal anomaly) (Balan et al., 1998; Zou et al., 2000; Romero-Hernandez et al., 2018). However, seasonal variations have not yet been analyzed for the ionospheric delay.

The ionospheric electron density (or ion density) is mainly controlled by the photoionization, the loss through recombination, and transport processes. Transport processes play a significant role in the T–I composition and are responsible for the plasma distribution, possibly leading to the observed ionospheric anomalies. Fuller-Rowell (1998) suggests a possible mechanism associated with the seasonal anomaly through the neutral wind.

This study aims to analyze the ionospheric TEC variations in both the Northern and Southern Hemisphere during a moderate solar activity during the inclining phase of solar cycle 24 (2011–2013). We use GNSS data from 70° S to 70° N latitude at 15° E longitude due to better coverage with ground measurements in TEC maps. The observed TEC is compared with the model-simulated TEC using different solar EUV flux models. The ionospheric delay against solar EUV flux has been investigated by Schmölter et al. (2020) using TEC observations. Therefore, the focus of the present study is laid on the ability to reproduce the ionospheric delay using the CTIPe model at 15° E.

In Sect. 2, we introduce the data sources and the CTIPe model. In Sect. 3, we investigate the TEC variability and a possible relationship with F10.7 index variations and compare TEC simulated with the different solar EUV flux models. In Sect. 4, we summarize our conclusions.
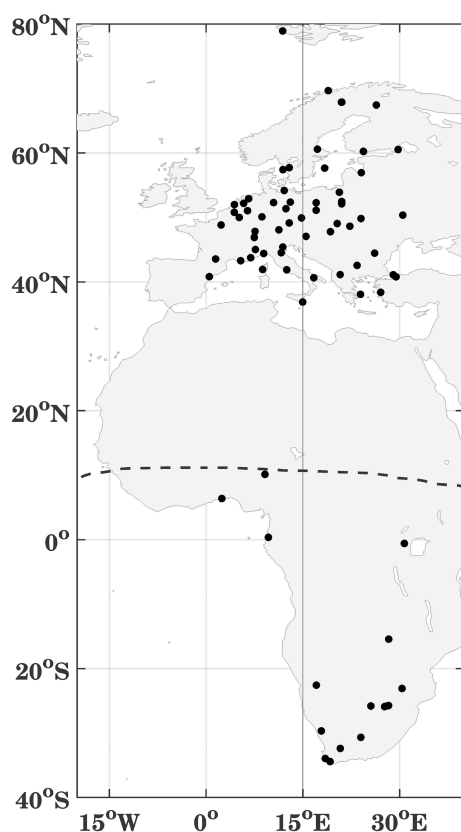
Figure 1. IGS stations around 15° E. The dashed black line represents the geomagnetic equator.

2 Observations and model

2.1 TEC observations

In this paper, we use TEC data from 70° S to 70° N latitude at 15° E from the International GNSS Service (IGS) provided by NASA's CDDIS (Noll, 2010), which are available at 1 h time resolution and with a latitude–longitude resolution of 2.5° × 5° (Hernández-Pajares et al., 2009). The accuracy of IGS TEC maps is given with 2–8 TECU (Chen et al., 2020). There are only few IGS stations in the Southern Hemisphere, but in the Northern Hemisphere (European region), there are several ground stations located around 15° E, as shown in Fig. 1.

2.2 Solar EUV radiation

Several solar proxies are available that have frequently been used in previous studies to represent the solar activity level compared to the ionospheric parameters before the space age and due to the unavailability of direct solar EUV measurements. Continuous time series of the solar EUV spectrum itself, however, have been available since the launch of the NASA Thermosphere Ionosphere Mesosphere Energetics and Dynamics (TIMED) satellite mission in 2001. Solar ir-

radiance measurements from the TIMED Solar Extreme Ultraviolet Experiment (SEE) instrument have been available since 22 January 2002 (Woods et al., 2005). The SEE instrument is designed to measure the soft X-rays and EUV radiation from 0.1 to 194 nm, with resolution and accuracy of 0.1 nm and approximately 10 %–20 %. SEE includes two instruments, the EUV grating spectrograph and the soft X-ray (XUV) photometer system (Woods et al., 2000). Here we use daily values of solar irradiance integrated from 1 to 105 nm wavelength. The TIMED SEE observations are used for comparison with the empirical solar flux models, SOLAR2000 and EUVAC.

Furthermore, the Solar Dynamics Observatory (SDO) EUV Variability Experiment (EVE) provides a continuous high-resolution spectrum with a wavelength range from 0.1 to 120 nm, a spectral resolution of 0.1 nm, and a temporal resolution of 20 s. (Woods et al., 2010; Pesnell et al., 2011). The high-resolution EUV observations provided by the SDO EVE satellite have been used to calculate an ionosphere delay in TEC.

Solar proxies are mostly used as a solar activity representation in thermosphere–ionosphere models. Hence, we also use the daily F10.7 index for our analysis.

2.3 CTIPe model

The CTIPe model is a global, first-principle, three-dimensional numerical, physics-based coupled thermosphere–ionosphere–plasmasphere model, which self-consistently solves the primitive equations of continuity, momentum, and energy to calculate wind components, global temperature, and the composition of neutrals, which is further used to calculate plasma production, loss, and transport. The model consist of four components, namely a neutral thermosphere model (Fuller-Rowell and Rees, 1980), a midlatitude and high-latitude ionosphere convection model (Quegan et al., 1982), a plasmasphere and low-latitude ionosphere model (Millward et al., 1996), and an electrodynamics model (Richmond et al., 1992). The calculations are performed with 2°/18° latitude/longitude resolution. In the vertical direction, the atmosphere is divided into 15 levels in logarithmic pressure at an interval of one scale height, starting from a lower boundary at 1 Pa (about 80 km altitude) to above 500 km altitude at pressure level 15. The high-latitude ionosphere (above 55° N or S) and the midlatitude–low-latitude ionosphere–plasmasphere components have been implemented as separate modules.

The numerical solution of the composition equation and the energy and momentum equations describe transport, turbulence, and diffusion of atomic oxygen, molecular oxygen, and nitrogen (Fuller-Rowell and Rees, 1983). To run the model, external inputs are required like solar UV and EUV, Weimer electric field, TIROS/NOAA auroral precipitation, and tidal forcing from the Whole Atmosphere Model (WAM). The F10.7 index is used as an input solar proxy to

calculate ionization, heating, and oxygen dissociation processes in the ionosphere. The CTIPe ionosphere results include the major ion species H^+ and O^+ for all altitudes and other molecular and atomic ions, N_2, O_2, NO^+, and N^+, below 400 km. Detailed information on the CTIPe model is available in Codrescu et al. (2008, 2012) and Fernandez-Gomez et al. (2019).

2.4 EUV representation in the CTIPe model

2.4.1 SOLAR2000 model

The SOLAR2000 model is the most recent EUV model version in a series of iterations by Tobiska et al. (2000). SOLAR2000 incorporates multiple satellite and rocket measurements, including the AE-E satellite observations, to specify both a reference spectrum and solar variability. The EUV is calculated using the Lyman-α flux and the F10.7 index with the set of modeling equations. SOLAR2000 determines the EUV irradiance for 809 emission lines and also for 39 wavelength bands.

2.4.2 EUVAC solar flux model

Within CTIPe, a reference solar spectrum based on the EUVAC model (Richards et al., 1994) and the Woods and Rottman (2002) model, driven by variations of input F10.7, is used. The EUVAC model is used between 5 and 105 nm and the Woods and Rottman (2002) model for 105 to 175 nm. Solar flux is obtained from the reference spectra using the following equation:

$$f(\lambda) = f_{\text{ref}}(\lambda)\,[1 + A(\lambda)(P - 80)], \tag{1}$$

where f_{ref} and A are the reference spectrum and solar variability factor, respectively, and $P = 0.5 \times$ (F10.7 + F10.7A), where F10.7A is the average of F10.7 over 81 d.

The EUVAC model includes solar flux in 37 wavelength bins based on the measured F74113 solar EUV reference spectrum (Hinteregger et al., 1981) and the solar cycle variation of the flux.

2.4.3 Comparisons between empirical EUV irradiance variability models and observations

We compare TIMED SEE observations with the two empirical models constructed from direct proxy parameterizations of the EUV irradiance database, which are used to represent EUV in the CTIPe model.

Figure 2 shows the modeled integrated irradiance spectra from 5 to 105 nm calculated by both models, together with the TIMED SEE irradiance from 2011 to 2013. The second y axis shows the F10.7 index used to calculate the spectra in empirical models. In comparison to the SOLAR2000 model flux and TIMED SEE, flux values calculated by the EUVAC model are smaller. There is a significant difference between

the flux models and the observed irradiance. The flux calculated by the SOLAR2000 model overestimates the observed flux mostly during the Northern Hemisphere winter months, whereas it is in good agreement during Northern Hemisphere summer months. The observed EUV irradiance during moderate solar activity is comparable to the SOLAR2000 flux, with a difference of about 10 % and 23 % higher than the EUVAC model. The EUVAC flux is about 30 % lower than the SOLAR2000 model. The correlation coefficient of EUV from both the EUV flux models with the observed EUV flux is approximately 0.90 during the study period. In summary, the SOLAR2000 model is in relatively good agreement with the observed flux, while the EUVAC model underestimates SOLAR2000 and the TIMED SEE flux. These results agree with earlier comparisons (Lean et al., 2003; Woods et al., 2005; Lean et al., 2011, and references therein).

Woods et al. (2005) compared the TIMED SEE observations with the flux calculated from different empirical models for 8 February 2002. They reported that the empirical models are within 40 % of the SEE measurement at wavelengths above 30 nm. The EUVAC and SOLAR2000 models agreed best with TIMED SEE, compared to the other models.

Lean et al. (2003) validated the NRLEUV model with different empirical models such as SOLAR2000, HFG (Hinteregger et al., 1981), and EUVAC. In absolute scales, NRLEUV, HFG, and EUVAC have total energies that agree within 15 %, but the SOLAR2000 absolute scale is more than 50 % higher. Their study reveals that long EUV wavelength (70 to 105 nm) energy contributions (about 46 % of the whole flux from 5 to 105 nm) are the main reason for the higher EUV flux in the SOLAR2000 model compared to other empirical models.

3 Results and discussion

In the following sections, we show the results and discuss the TEC observations and their comparison with the modeled TEC at 15° E. Furthermore, relations with solar radiation and the delayed response over both the Northern and Southern Hemispheres are presented. Schmölter et al. (2020) have reported on a detailed investigation of the delayed ionospheric response over European and Australian regions. Here, we analyze the delayed response at 15° E covering the latitudes from 70° S to 70° N and compare the response over the southern African region with the European region.

In this study we have addressed the following points:

1. The TEC variations at moderate solar activity of solar cycle 24 are analyzed to compare the input for the delay analysis. A characterization of these differences between observed and modeled TEC is important to derive further relations.
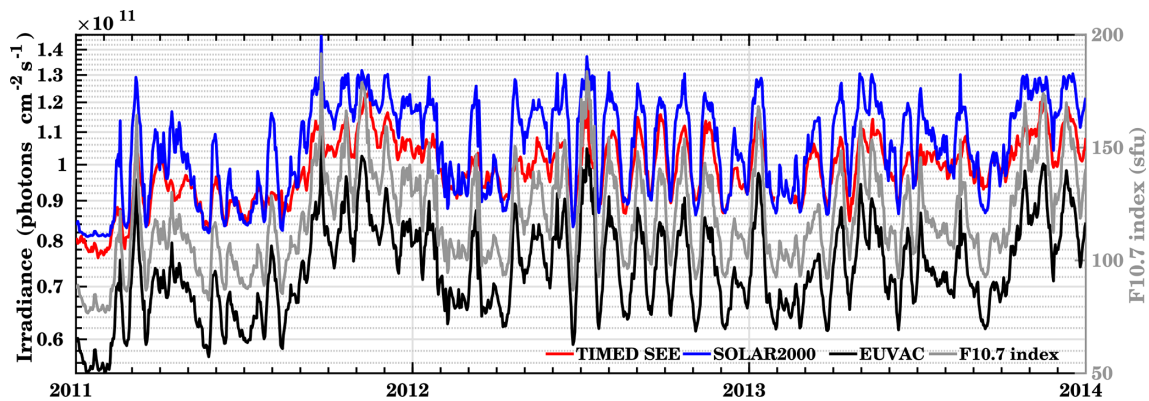
Figure 2. Time series of 0.5 to 105 nm integrated daily irradiance from 2011 to 2013 estimated from TIMED SEE observations, SOLAR2000, and EUVAC. The right y axis represents the F10.7 index.

2. We used the periodicity estimation (frequency analysis) to study observed and modeled TEC characteristics in detail.

3. The relation between the F10.7 index and hemispheric TEC has been used to analyze the solar and ionospheric inputs of delay estimation.

4. In our study we focus on the ionospheric delay estimation as a main point of our analysis.

5. The comparison of observed TEC variations with simulated TEC is done by using different flux models. In previous work it has already be shown that the solar activity has the strongest impact on TEC under nominal conditions and is therefore significant for the derived delay.

3.1   TEC variation at moderate solar activity of solar cycle 24

The ionospheric electron density strongly varies from day to night depending on the daily variations of solar radiation.

Figure 3 depicts the 11:00–13:00 LT averaged midday variations in TEC for the moderate solar activity conditions from 2011 to 2013. The figure shows the comparison between the observed TEC and modeled TEC simulated using the EUVAC flux model at 15° E longitude. Note that at this longitude, climatological hemispheric differences in TEC are expected due to peculiarities of the magnetic field, in particular the South Atlantic Anomaly, which causes low ionization in the Southern Hemisphere.

The TEC variations highly depend on the level of ionization due to the solar radiation flux. The observed TEC shows such variations compared to the SDO EVE-integrated flux (1–120 nm), as shown on the second y axis of Fig. 3. During 2012, there are continuous 27 d cycles. This kind of regular variation in solar observations enables us to explore the respective ionospheric variations, which are clearly driven by the ionization and recombination processes.

The maximum TEC is observed at the Equator and in low-latitude regions. The TEC level reduces towards the high-latitude regions. In general, the TEC values vary latitudinally depending on the northern and southern hemispheric season. At the Equator, the plasma moves upward and redistributes along the Equator, causing the fountain effect (Appleton, 1946). The thermospheric wind circulations firmly control the plasma movement. The plasma moves from the summer hemisphere to the winter one, causing a decrease in the F peak height, further decreasing the O/N_2 ratio. The TEC values in the Southern Hemisphere are higher than in the Northern Hemisphere.

Figure 3a shows maximum TEC around the Equator during the December solstice, and a minimum of TEC is observed during the June solstice of 2011, which coincides with the minimum solar EUV flux. There are local minima during equinoxes in 2013.

In comparison to observed TEC, the modeled TEC (Fig. 3b) is lower during the spring and summer period in the Southern Hemisphere, while it is in better agreement during the winter season. The bias between the modeled and observed TEC is higher during the spring and summer season in the Southern Hemisphere. In general, the modeled TEC is lower than the observed TEC.

The variations in TEC are not only controlled by the solar radiation, but there are also other factors such as local dynamics or geomagnetic activities due to solar wind variations, which also influence the ionospheric state (Abdu, 2016). Fang et al. (2018) studied day-to-day ionospheric variability and suggested that absolute values in TEC variability at low latitudes are largely controlled by solar activity, while for midlatitudes and high latitudes, however, solar and geomagnetic activities contribute roughly equally to the absolute TEC variability.

A detailed comparison between the observed TEC and modeled TEC simulated using the different solar flux models (SOLAR2000 and EUVAC) during January, June, and December is presented and discussed in Sect. 3.6.
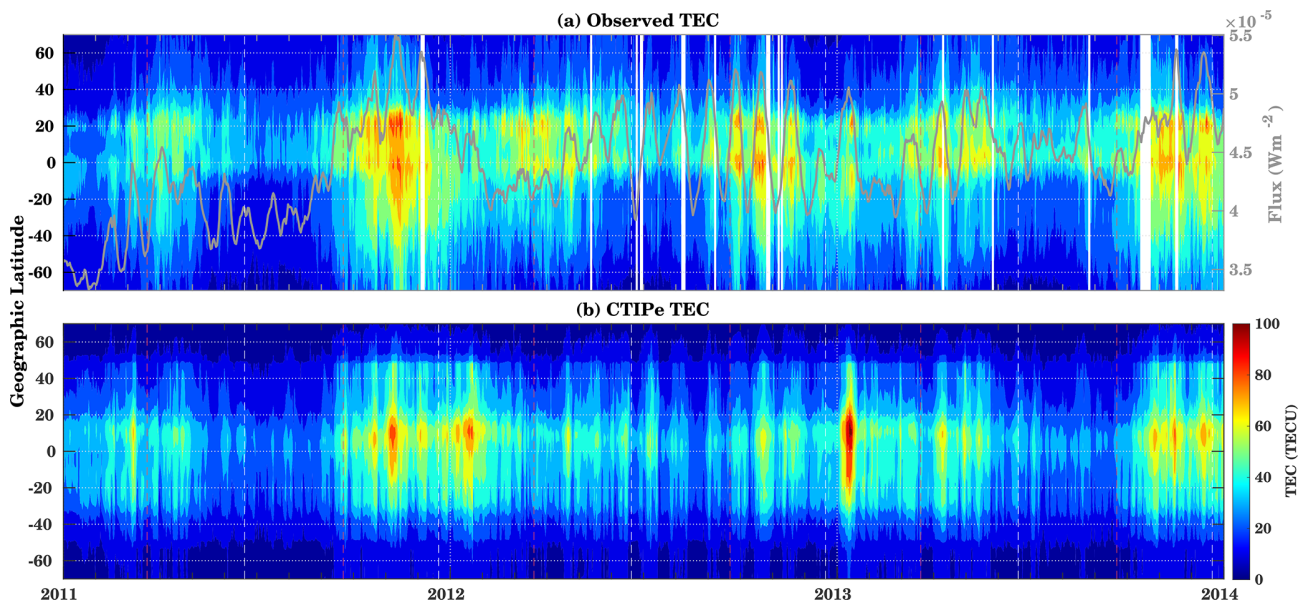
Figure 3. Latitudinal variation of **(a)** observed TEC and **(b)** model-simulated TEC around noon (11:00–13:00 LT) at 15° E longitude. The gray curve in panel **(a)** represents the SDO EVE-integrated flux (1–120 nm).

3.2 Periodicity estimation

Solar activity varies at different timescales from minutes to years or even centuries. The periodic behavior in the solar proxies has been studied by various authors to explore the response of the terrestrial atmosphere and especially the T–I region and to investigate the connection between solar variability and ionospheric parameters (Jacobi et al., 2016; Vaishnav et al., 2019). A widely used method to analyze periodicities in time series is the continuous wavelet transform (CWT). The CWT captures the impulsive events when they occur in the time series (Percival and Walden, 2000; Mallat, 2009). However, the CWT also reveals lower frequency features of the data hidden in the time series.

Here, we will investigate and compare the different temporal patterns of observed and modeled TEC. The daily TEC and F10.7 index from 2011 to 2013 are used to analyze the periodic behavior of the T–I system. Figure 4 shows the continuous wavelet spectra of the model-simulated TEC, observed TEC, and F10.7 for low latitudes [±30°], midlatitudes [± (30–60°)], and high latitudes [± (60–70°)] from 2011 to 2013. Here averaged TEC is used for the low latitudes, midlatitudes, and high latitudes.

The upper panels (a)–(c) of Fig. 4 show the CWT of modeled TEC, while the middle panels (d)–(f) show the observed TEC, respectively, over the different latitude bands mentioned in the figure title. The lower panel (g) shows the CWT of F10.7.

The CWT of modeled TEC shows the dominant 16–32 d oscillations during 2012. This is, however, not the case during 2011 and 2013. During these periods, the influence of other dynamical processes in the ionosphere (e.g., lower at-

mospheric forcing) is stronger. During these years, very weak 27 d periodicity is observed. The 27 d period is stronger during December and January. Pancheva et al. (1991) showed that the 27 d variation in the lower ionosphere (D region) is often caused by dynamical forcing (planetary waves), particularly in the winter season under low solar activity. A similar 16–32 d periodicity is observed in the F10.7 index. It is well known that the 27 d periodicity is one of the major and dominant modes of variations in the solar proxies.

As an advantage, the CWT also shows small-scale features. Over low latitudes and midlatitudes, 8–16 d oscillations are observed to be dominant. Furthermore, another high-power region is visible in the 128–256 d period, representing the semi-annual oscillations in both modeled and observed TEC and in the F10.7 index. The semi-annual oscillation is mostly dominant during the period of investigation. Apart from it, in model-simulated TEC, a 64–128 d period is observed during 2012 and 2013. The oscillations are stronger at low-latitude and midlatitude stations compared to high latitudes.

The second row of Fig. 4 shows the oscillations in the observed TEC. Here, a weak 27 d cycle is observed during December, and the 128–256 d period is mostly dominant during 2011 and 2012. There is a weak signature of semi-annual oscillations during 2013. As compared to the periodicity observed in model-simulated TEC, the 64–128 d periodicity is missing in the observations over all the latitudes. Furthermore, shorter period fluctuations can be seen, especially at high latitudes (Fig. 4f), with a preference for the winter season. These may be connected with planetary wave effects from below (e.g. Altadill et al., 2001, 2003).

Figure 4g shows the CWT spectra of the F10.7 index. Here the dominant period is 16–32 d during 2012, and a weak 16–32 d period oscillation is observed during 2011 and 2013.

In general, from the above investigation, it can be seen that 16–32 d periodicity was dominant during 2012. Vaishnav et al. (2019) used cross-wavelet and Lomb–Scargle periodogram techniques to estimate the periodicity of various solar proxies and global TEC during long time series from 2000–2016. They found that the semi-annual oscillation is mostly dominant during the solar maximum years 2001–2002 and 2011–2012.

3.3 Relation between F10.7 index and hemispheric TEC

Solar activity has the strongest effect on ionospheric variations, especially during enhanced solar activity. The last solar minimum was extremely extended, and the following solar cycle was quite weak (e.g., Huang et al., 2016), so that meteorological influences become more relevant. To examine the effect of solar activity on TEC variations during a weak solar cycle, we analyzed the relationship between F10.7 and midday TEC (11:00–13:00 LT). Figure 5 shows the correlation between TEC and F10.7 during 2011–2013 for the Northern Hemisphere (NH; upper panels) and Southern Hemisphere (SH; lower panels), indicating the correlation coefficient (R). In order to represent the NH and SH, daily data of 40° N and 40° S latitudes at 15° E longitude have been used respectively. The mean root mean square (rms) at 40° N is 6.92 TECU, and the mean rms at 40° S is 7.54 TECU for the whole period.

We have calculated correlations using the observed TEC over the NH and SH. During 2011, the maximum correlation for all the years is observed, which amounts to $R = 0.71/0.79$ for the NH/SH. This suggests that midday TEC values are mainly controlled by solar EUV radiation.

From the current study and past publications (Romero-Hernandez et al., 2018), it is well known that during high solar activity, weak correlations are observed compared to the moderate solar activity conditions. But during the year 2012, the lowest correlation of about 0.06 was observed in the SH, while the correlation was about 0.36 in the NH region. During the year 2013, the correlation is weaker than during 2011, namely about 0.42 for the NH and 0.60 for the SH.

In general, the correlation coefficient is higher in the southern hemispheric region as compared to the Northern Hemisphere during 2011 and 2013, whereas lower correlations are observed during the year 2012. The analysis for 2012 shows some unexpected behavior over these study regions. This unusual behavior could be due to physical and chemical processes that have an impact on the ionospheric state.

3.4 Cross-correlation and delay estimation

The possible relations between solar activity, geomagnetic activity, and ionospheric parameters have been studied by several authors (e.g., Abdu, 2016; Fang et al., 2018; Vaishnav et al., 2019). However, several past studies, due to the unavailability of high-resolution datasets, used only daily resolution. To estimate the ionospheric delay, different ionospheric parameters have been considered using daily resolution data; an ionospheric delay of about 1–2 d against solar proxies has been reported (Jakowski et al., 1991; Jacobi et al., 2016; Vaishnav et al., 2019). Only recently, Schmölter et al. (2020) used SDO EVE and GOES EUV fluxes to calculate the ionospheric delay of about 17 h as a mean value based on hourly time resolution data. This observed delay was also confirmed by numerical physics-based models (Ren et al., 2018; Vaishnav et al., 2018).

Here, we investigate the ionospheric delay using hourly resolution observations and compare it with the model-simulated TEC. Figure 6 shows the cross-correlation and a corresponding ionospheric delay calculated using SDO EVE-observed integrated flux from the 1 to 120 nm wavelength region in comparison with modeled TEC at 15° E longitude. The modeled TEC used for these analyses has been simulated using the EUVAC solar flux model and the F10.7 index as a solar input proxy to calculate the input spectra. The cross-correlation was applied on independent monthly datasets from 2011–2013, as the maximum correlation is expected during the solar rotation period. If longer periods are selected, the periodicity is a mixture of lower and higher solar activity. Then the appearance of sunspots at different locations on the solar disk shifts the maximum EUV emissions in relation to coherence with one another, for which the correlation is expected to decrease. Even shorter periods can result in lower correlations due to the reduced sampling size, i.e., a stronger impact of smaller deviations as well. Similar results have been shown by Vaishnav et al. (2019). They studied correlation analysis between TEC and multiple solar proxies for different time periods. Their study revealed that the correlation is lower during shorter and longer periods. Better correlations are only expected during the solar rotation period.

The upper panels of Fig. 6 show the (a) cross-correlation and (c) the ionospheric delay using the observed TEC. The maximum correlation is observed during the year 2012 with about 0.5, while in 2011 and 2013 the correlation is weaker. The lowest correlation is observed during the winter months of 2011–2012. Further, latitudinal variations are also seen in the correlation coefficient.

Figure 6c shows the cross-correlation coefficient calculated using the modeled TEC and SDO-EVE flux. The correlation coefficient is higher than the one seen in the observed TEC. There are several processes that can influence the behavior of the ionosphere and the real observations such as lower atmospheric forcing or geomagnetic activity. But in the model, lower atmospheric variability is not included, except
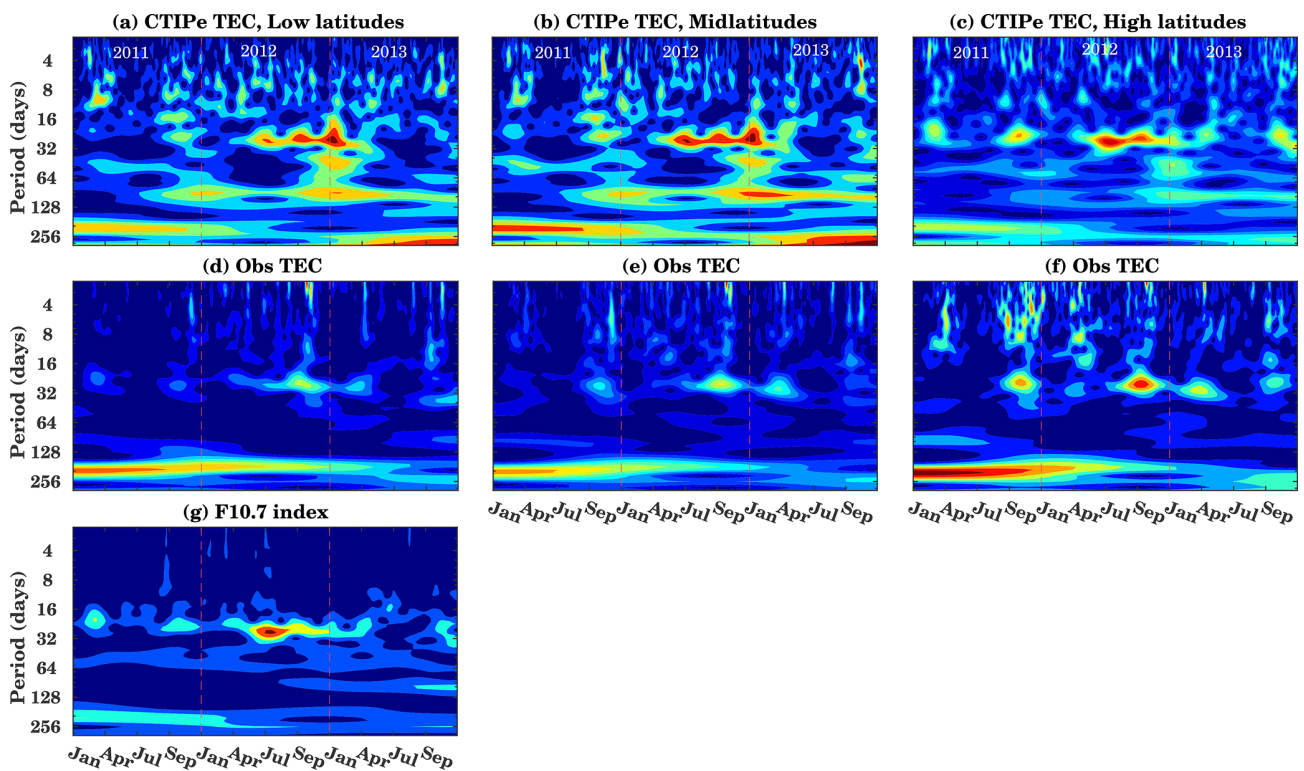
Figure 4. Wavelet continuous spectra of daily modeled TEC **(a–c)**, observed TEC **(d–f)** for different low latitudes [$\pm30°$], midlatitudes [$\pm(30° - 60°)$], and high latitudes [$\pm(60° - 70°)$], and **(g)** F10.7 index.

in a statistical sense, which affects the total variability; hence higher correlation is observed in modeled TEC compared to observed TEC.

The analysis suggests that the model can reproduce similar trends and features to those shown in the observations. The overall correlation coefficient in the Southern Hemisphere is higher than in the Northern Hemisphere.

Figure 6b shows the ionospheric delay calculated from the observed TEC against the SDO flux. The ionospheric delay varies strongly with latitude and time. A shorter ionospheric delay is observed during January as compared to other months. For January, the ionospheric delay is about 13–16 h. The maximum delay is about 22 h in the low-latitude region during 2011 and 2012 but about 22–23 h during 2013 in low latitudes and midlatitudes. During 2011 the ionospheric delay is maximum for the winter period at the Equator with about 22 h, while it decreases towards high latitudes. A very low ionospheric delay of about 5–10 h is observed during August 2012 for midlatitudes. An interesting feature that can be noted here is that the ionospheric delay increases with increasing solar activity from 2011 to 2013.

A similar analysis for the estimation of the ionospheric delay has been performed for the model-simulated TEC, as shown in Fig. 6d. The CTIPe model is able to reproduce features seen in the observed TEC (Fig. 6b). The ionospheric delay is higher during December and follows the solar activity.

In the higher latitude region (above 60° latitude in both hemispheres), the ionospheric delay in the model is smaller than in the observations and amounts to about 5–10 h. Simultaneously, the correlation coefficient is high at the high-latitude regions in the Southern Hemisphere and is about 0.4, as shown in Fig. 6c. This bias is due to the model limitations such as model input, grid resolution, and insufficient physical descriptions (Negrea et al., 2012).

Generally, the ionospheric delay calculated from the modeled TEC is in good agreement with the observed one, and it is about 17 h. Furthermore, the ionospheric delay is always higher in the Northern Hemisphere as compared to the Southern Hemisphere. Partly negative correlation has been observed in both the model and the observations. This negative correlation might be possible due to additional heating sources or unknown factors such as the state of the ionosphere and its dominant physical processes. Another more important factor is lower atmospheric forcing, such as gravity or planetary wave. Gravity waves can influence the upper atmosphere's thermal and compositional structures. These sources might lead to changes in the ionosphere's local dynamics and contribute to additional increase and decrease in the electron density, irrespective of actual solar activity conditions.
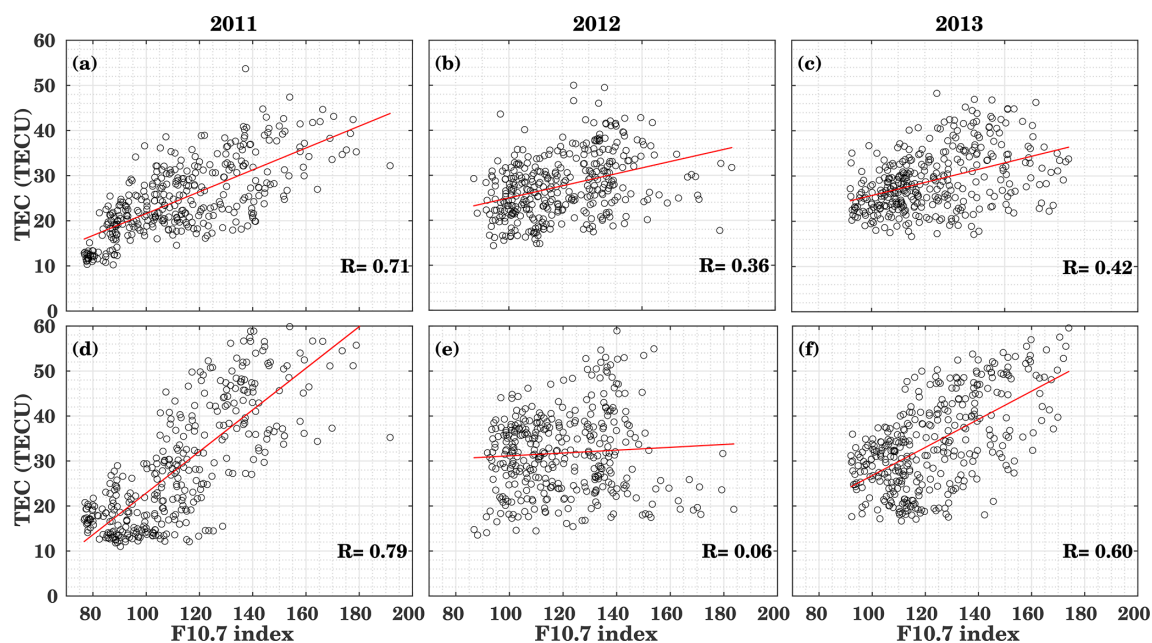
Figure 5. Relation between F10.7 index and midday-observed TEC (11:00–13:00 LT) at 40° N, 15° E (**a, b, c**) and 40° S, 15° E (**d, e, f**) for 2011, 2012, and 2013. The red line is the linear fit.

The correlation coefficients in the Southern Hemisphere are generally higher than in the Northern Hemisphere.

Furthermore, to understand the mean variations of TEC and its connection with the ionospheric delay, we calculated the latitudinal mean observed TEC with the standard deviations and compare it with the model-simulated TEC from 2011 to 2013 as shown in Fig. 7a. The model-simulated TEC underestimates the observed TEC at all latitudes. As expected, the maximum TEC of about 50 TECU is observed at low latitudes, while model-simulated TEC is about 45 TECU. The maximum bias is observed poleward of 35° S and 45° N, and this bias increases towards high latitudes. As discussed in the previous sections, there are several problems such as providing inputs for the model, grid resolution effects, and insufficient physical descriptions that need to be addressed in the future to reduce the bias in the model.

To see the mean latitudinal variations of ionospheric delay, we used the monthly delay calculated from 2011 to 2013. The mean ionospheric delay is about 17–18 h in the observations at low latitudes and midlatitudes, while it is about 15 h in the high-latitude regions. As compared to the delay in observations, the model-simulated delay is 1–2 h less in the low latitudes and midlatitudes, but the difference strongly increases in the high-latitude regions. Poleward of 55°, the ionospheric delay reduces to less than 10 h.

This analysis shows that the model can reproduce the ionospheric delay as seen in the observations and generally produces a delay of about 18 h at middle latitudes.

3.5 Observed TEC variations and its comparison to TEC simulated using different EUV flux models

To further visualize the observed daily TEC and its comparison with the modeled TEC at different latitudes, the results are presented in the box-and-whisker plot in Fig. 8 for June and December 2011 to 2013. The box has lines at the lower quartile, median (red line), and upper quartile values. Whiskers extend from each end of the box to the adjacent values in the data. Outliers beyond the whiskers are displayed using the "+" sign.

To analyze the TEC variations at the grid point 40° S and 40° N, for 15° E each in both hemispheres during June and December (left panels, a–d), we compare the observed TEC (O) with the modeled TEC simulated using the SOLAR2000 (S) and the EUVAC (E) flux model for different years. The F10.7 index is used as the primary solar input to calculate the spectra in the model. The box plots have been generated using the daily data of June and December, respectively. The right panels (e–h) show the differences between observed and modeled TEC at different corresponding locations and months (e–h).

The median of modeled TEC using the SOLAR2000 flux model overestimates the observed TEC by about 10, 11, and 7 TECU during June 2011, 2012, and 2013, respectively, at 40° S as shown in Fig. 8a, e. A slightly smaller overestimation can be seen using the EUVAC flux model, with a difference of less than about 5 TECU during 2011 and 2013 and 6 TECU during 2012. Hence, both models generally show overestimation of TEC at this latitude and month.
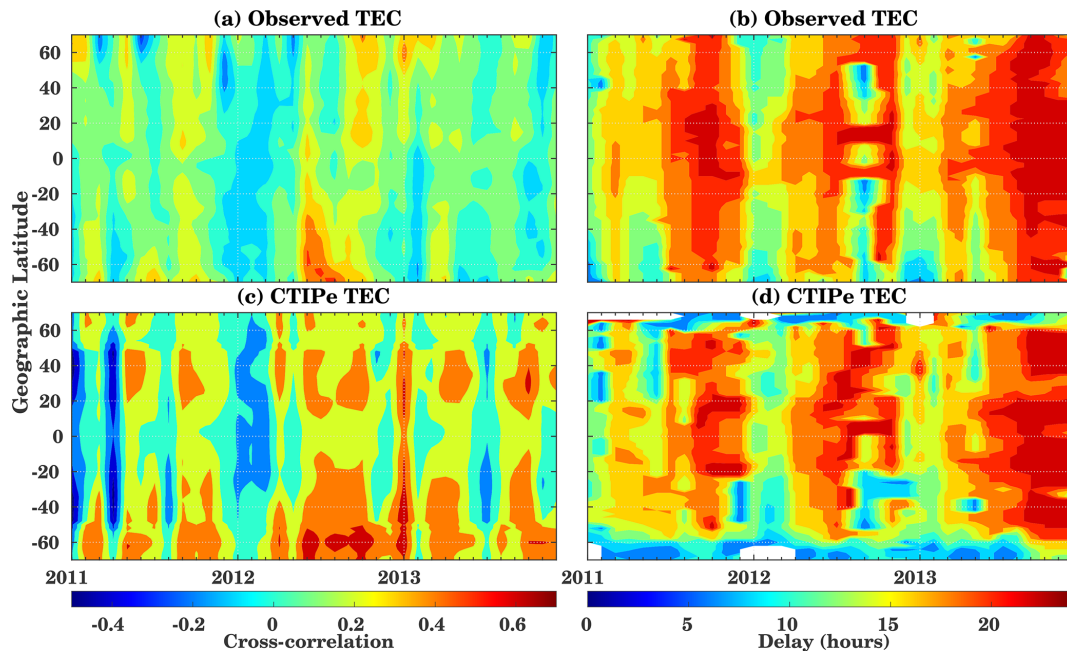
Figure 6. Correlation coefficient **(a, c)** and delay estimation **(b, d)** using observed **(a, b)** and model-simulated **(c, d)** hourly TEC and SDO EVE-integrated flux (1–120 nm).
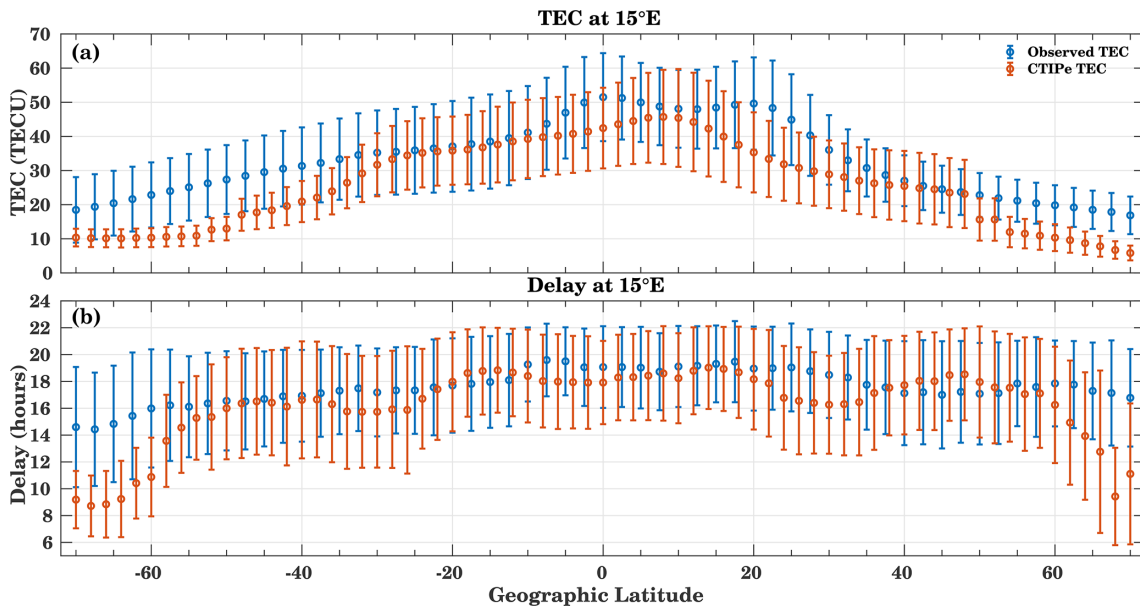

Figure 7. (a) Daily mean TEC variations and **(b)** delay estimation using observed (blue) and model-simulated (red) hourly TEC and SDO EVE-integrated flux. The error bars show standard deviations of mean values.

Figure 8b and f show the TEC plot and difference box plot at 40° N, 15° E during June. At this grid point, the observed TEC values are high compared to the southern hemispheric grid point. The observed TEC is quite comparable with the modeled TEC simulated using SOLAR2000 during 2011 and 2013. However, it shows an overestimation by 2 TECU during 2012. In comparison to SOLAR2000-simulated TEC, the EUVAC-model-based TEC simulation shows an underestimation of about 5–10 TECU. The modeled TEC using the SOLAR2000 flux model is higher than the one simulated using the EUVAC model. A good agreement between the modeled and observed TEC can be seen at the southern and northern hemispheric grid points (Fig. 8e–f), where the bias is less than 10 TECU. The analysis for December is shown in
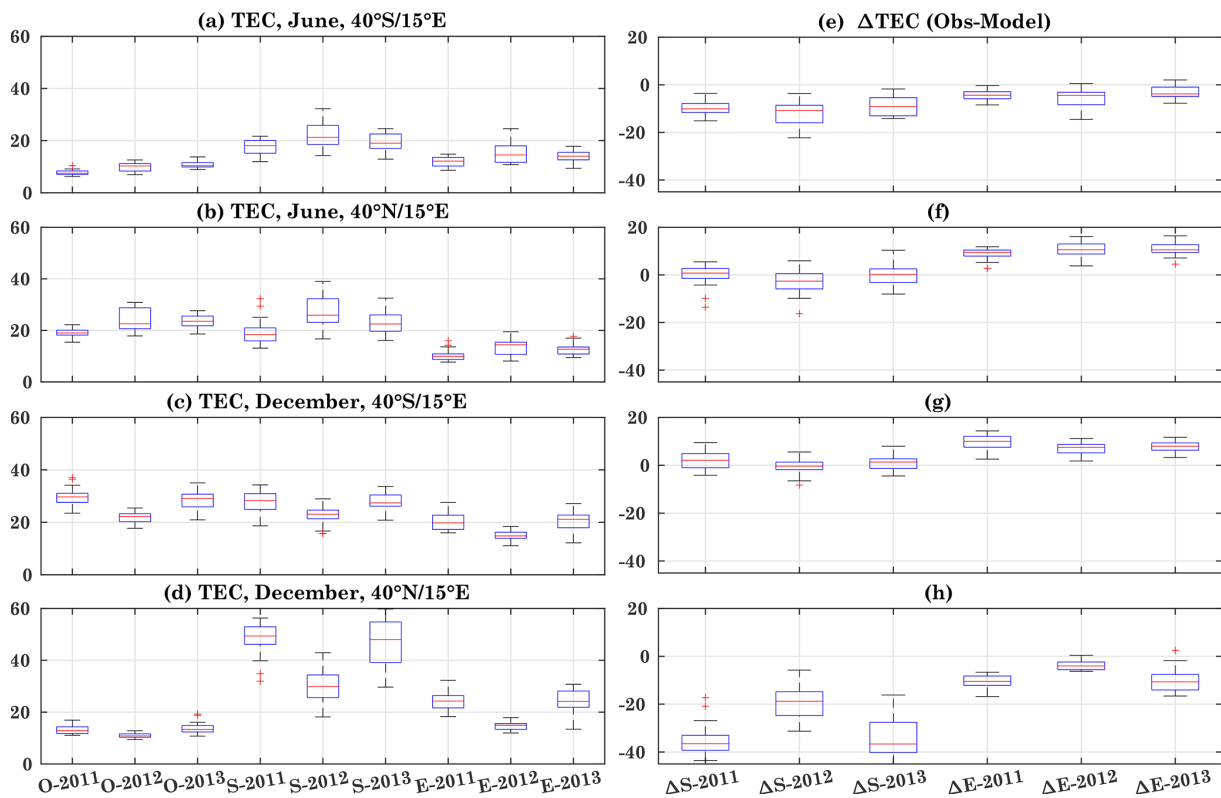
Figure 8. Box plots based on daily TEC during June and December 2011–2013 for 40° S and 40° N. The months and location are mentioned in the figure titles. Here O, S, and E represent observed, CTIPe-SOLAR2000 flux model, and CTIPe-EUVAC flux model TEC, respectively. The left panels show the box plots for the difference between observed TEC with the model-simulated TEC using different flux models. Data points beyond the whiskers are displayed using the "+" sign.
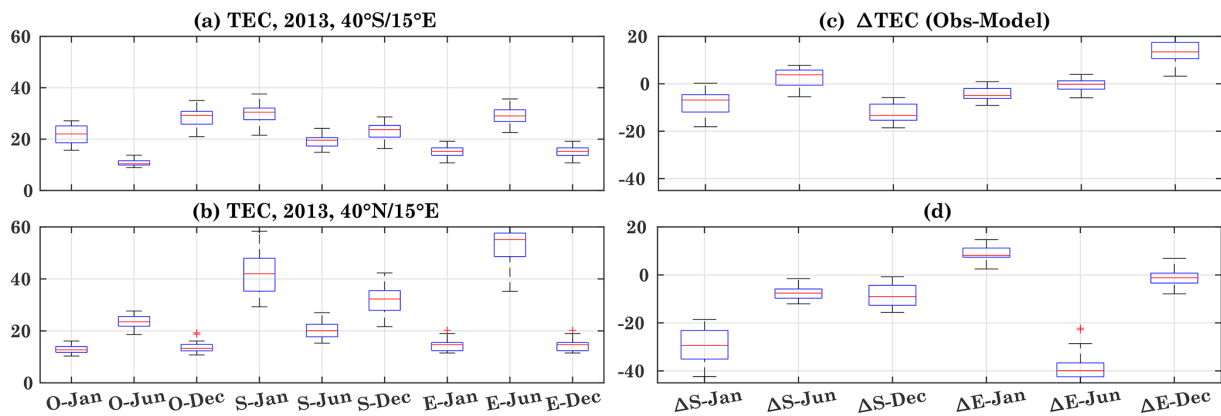

Figure 9. Box plots of observed daily TEC and model-simulated TEC using F10.7A as solar input for 40° S and 40° N during January, June, and December for the year 2013.

Fig. 8c–d. The difference plot (Fig. 8g–h) shows a different behavior than in June. The modeled TEC simulated using the SOLAR2000 is in agreement during December over 40° S, but the modeled TEC simulated using the EUVAC underestimates the observations by about 10 TECU.

Over the grid point 40° N, 15° E, both flux models result in an overestimation, and the SOLAR2000 flux model produces maximum bias during 2011 and 2013, with about 40 and 20 TECU during 2012. The modeled TEC simulated using the EUVAC model shows an overestimation of about 10 TECU.

The overall difference between the model and observations is larger during December as compared to June. The

discrepancy observed in the CTIPe results is possibly due to the various reasons mentioned in the previous section.

Figure 9a–b show the box plots of TEC for January, June, and December during 2013. Here the CTIPe model run used the modified F10.7A index (average of previous 41 d averages with previous day value) as solar input to calculate the spectra in solar flux models. We choose this period to consider different ionizing radiations. Here the difference plots Fig. 9c–d show bias during January, June, and December at 40° S, 15° E and 40° N, 15° E.

At 40° S, 15° E, the modeled TEC simulated using the SOLAR2000 flux model overestimates TEC during January and December and underestimates TEC during June by about 5 TECU. The modeled TEC simulated using the EUVAC model shows quite different behavior. It shows overestimation during January and June but underestimation during December.

In comparison to the southern hemispheric grid point, the TEC over 40° N, 15° E simulated using the SOLAR2000 shows overestimation of TEC and maximum bias during January by about 25 TECU. In the case of the EUVAC model, it shows underestimation during January compared to observed TEC. During June and December, the modeled TEC simulated using EUVAC shows overestimation with respect to the observed TEC.

Here it is interesting to note that the southern hemispheric grid point shows good agreement compared to the Northern Hemisphere. During January, the SOLAR2000 model overestimated TEC by about 20 TECU, while the EUVAC model overestimated TEC by 5 TECU at 40° N, 15° E. The observed TEC shows seasonal variations, while the model is not able to capture seasonal behavior.

We performed a similar comparison using F10.7A (average of previous 81 d averages with previous day value) as solar input proxy in the solar flux models (not shown). The results show a similar bias as the one presented in Fig. 9. The flux values provided by EUVAC are smaller than SOLAR2000 results in the photoionization processes, and this results in a decrease in TEC.

Klipp et al. (2019) compared the IGS TEC with the modeled TEC using different flux models (EUVAC and SOLAR2000) over Central and South American regions. They showed different behavior of empirical models during different solar activity conditions.

The large bias observed in the physics-based model is mainly due to the solar EUV flux input and grid resolution. The model needs further improvement regarding the input of solar flux.

Miyoshi et al. (2018) investigated the effects of the horizontal resolution on the electron density distribution using the GAIA model. They showed that fluctuations produced in model-simulated electron density with periods of less than about 2 h and length scales of less than about 1000 km with a high horizontal resolution of 1° × 1°, which are in good agreement with observations. These fluctuations are not

seen in a low-resolution (2.5° × 2.5°) simulation. Hence, the model resolution is an important factor for the large bias between observations and model simulations.

4 Summary

We presented a climatological analysis of GNSS-observed and CTIPe-model-simulated TEC during 3 years, 2011 to 2013, of the 24th solar cycle, to investigate and compare modeled TEC with the observed ones, the ionospheric delay, periodicity estimation, and relation of TEC with the solar proxy. Our results show a distinct low-latitude and midlatitude TEC response at a longitude of 15° E.

The main results of this study can be summarized as follows:

– The periodicity estimations over the low latitudes, midlatitudes, and high latitudes show that 16–32 d periodicity was dominant during 2012. As compared to the periodicity observed in model-simulated TEC, the 64–128 d periodicity was missing in the observations over all considered latitudes.

– While comparing TEC against the F10.7 index, the correlation is higher in 2011 and 2013 over the Southern Hemisphere as compared to the Northern Hemisphere; i.e., there is a hemispheric asymmetry. A similar characteristic has been observed by Romero-Hernandez et al. (2018). The lowest correlation is observed during 2012.

– The ionospheric delay has been investigated using the modeled and observed TEC against the solar EUV flux. The ionospheric delay estimated using model-simulated TEC is in good agreement with the delay estimated for observed TEC. An average delay for the observed (modeled) TEC is about 17 (16) h. The study confirms the model's capabilities to reproduce the delayed ionospheric response against the solar EUV flux. These results are in close agreement with Schmölter et al. (2020).

– The average difference between the northern and southern hemispheric delay estimated for observed (modeled) TEC is about 1 (2) h. The average delay is higher in the Northern Hemisphere as compared to the Southern Hemisphere.

– Furthermore, the observed TEC is compared with the modeled TEC simulated using the SOLAR2000 and EUVAC flux models within CTIPe at the northern and southern hemispheric grid points. The analysis indicates that TEC simulated using the SOLAR2000 flux model overestimates the observed TEC, which is not the case when using the EUVAC flux model. The large bias observed in the physics-based model is mainly due to the solar EUV flux input and grid resolution. Our results

show that the model needs further improvement in respect to the solar flux input to further reduce the presented deviation to TEC measurements.

Author contributions. RV together with CJ and MC performed the CTIPe model simulations. RV drafted the first version of the manuscript. ES, CJ, and JB actively contributed to the analysis. All authors discussed the results and contributed to the final version of the paper.

Competing interests. Christoph Jacobi is one of the editors-in-chief of *Annales Geophysicae*. The authors declare that they have no conflict of interest.

Review statement. This paper was edited by Dalia Buresova and reviewed by Gerhard Schmidtke and one anonymous referee.

References

Abdu, M. A.: Electrodynamics of ionospheric weather over low latitudes, Geoscience Letters, 3, 11, https://doi.org/10.1186/s40562-016-0043-6, 2016.

Afraimovich, E. L., Astafyeva, E. I., Oinats, A. V., Yasukevich, Yu. V., and Zhivetiev, I. V.: Global electron content: a new conception to track solar activity, Ann. Geophys., 26, 335–344, https://doi.org/10.5194/angeo-26-335-2008, 2008.

Altadill, D., Apostolov, E., Solé, J., and Jacobi, C.: Origin and development of vertical propagating oscillations with periods of planetary waves in the ionospheric F region, Phys. Chem. Earth Pt. C, 26, 387–393, https://doi.org/10.1016/s1464-1917(01)00019-8, 2001.

Altadill, D., Apostolov, E. M., Jacobi, Ch., and Mitchell, N. J.: Six-day westward propagating wave in the maximum electron density of the ionosphere, Ann. Geophys., 21, 1577–1588, https://doi.org/10.5194/angeo-21-1577-2003, 2003.

Appleton, E. V.: Two Anomalies in the Ionosphere, Nature, 157, 691, https://doi.org/10.1038/157691a0, 1946.

Balan, N., Otsuka, Y., Bailey, G. J., and Fukao, S.: Equinoctial asymmetries in the ionosphere and thermosphere observed by the MU radar, J. Geophys. Res.-Space, 103, 9481–9495, https://doi.org/10.1029/97ja03137, 1998.

CDDIS: GNSS Atmospheric Products, available at: http://cddis.nasa.gov/Data_and_Derived_Products/GNSS/atmospheric_products.html, last access: 15 August 2018.

Chen, P., Liu, H., Ma, Y., and Zheng, N.: Accuracy and consistency of different global ionospheric maps released by IGS ionosphere associate analysis centers, Adv. Space Res., 65, 163–174, https://doi.org/10.1016/j.asr.2019.09.042, 2020.

Codrescu, M. V., Fuller-Rowell, T. J., Munteanu, V., Minter, C. F., and Millward, G. H.: Validation of the Coupled Thermosphere Ionosphere Plasmasphere Electrodynamics model: CTIPE-Mass Spectrometer Incoherent Scatter temperature comparison, Space Weather, 6, S09005, https://doi.org/10.1029/2007sw000364, 2008.

Codrescu, M. V., Negrea, C., Fedrizzi, M., Fuller-Rowell, T. J., Dobin, A., Jakowsky, N., Khalsa, H., Matsuo, T., and Maruyama, N.: A real-time run of the Coupled Thermosphere Ionosphere Plasmasphere Electrodynamics (CTIPe) model, Space Weather, 10, S02001, https://doi.org/10.1029/2011sw000736, 2012.

Fang, T.-W., Fuller-Rowell, T., Yudin, V., Matsuo, T., and Viereck, R.: Quantifying the Sources of Ionosphere Day-To-Day Variability, J. Geophys. Res.-Space, 123, 9682–9696, https://doi.org/10.1029/2018ja025525, 2018.

Fernandez-Gomez, I., Fedrizzi, M., Codrescu, M. V., Borries, C., Fillion, M., and Fuller-Rowell, T. J.: On the difference between real-time and research simulations with CTIPe, Adv. Space Res., 64, 2077–2087, https://doi.org/10.1016/j.asr.2019.02.028, 2019.

Fuller-Rowell, T. J.: The "thermospheric spoon": A mechanism for the semiannual density variation, J. Geophys. Res.-Space, 103, 3951–3956, https://doi.org/10.1029/97ja03335, 1998.

Fuller-Rowell, T. J. and Rees, D.: A Three-Dimensional Time-Dependent Global Model of the Thermosphere, J. Atmos. Sci., 37, 2545–2567, https://doi.org/10.1175/1520-0469(1980)037<2545:atdtdg>2.0.co;2, 1980.

Fuller-Rowell, T. J. and Rees, D.: Derivation of a conservation equation for mean molecular weight for a two-constituent gas within a three-dimensional, time-dependent model of the thermosphere, Planet. Space Sci., 31, 1209–1222, https://doi.org/10.1016/0032-0633(83)90112-5, 1983.

Hedin, A. E.: Correlations between thermospheric density and temperature, solar EUV flux, and 10.7 cm flux variations, J. Geophys. Res.-Space, 89, 9828–9834, https://doi.org/10.1029/ja089ia11p09828, 1984.

Hernández-Pajares, M., Juan, J. M., Sanz, J., Orus, R., Garcia-Rigo, A., Feltens, J., Komjathy, A., Schaer, S. C., and Krankowski, A.: The IGS VTEC maps: a reliable source of ionospheric information since 1998, J. Geodesy, 83, 263–275, https://doi.org/10.1007/s00190-008-0266-1, 2009.

Hinteregger, H. E., Fukui, K., and Gilson, B. R.: Observational, reference and model data on solar EUV, from measurements on AE-E, Geophys. Res. Lett., 8, 1147–1150, https://doi.org/10.1029/gl008i011p01147, 1981.

Huang, J., Hao, Y., Zhang, D., and Xiao, Z.: Changes of solar extreme ultraviolet spectrum in solar cycle 24, J. Geophys. Res.-Space, 121, 6844–6854, https://doi.org/10.1002/2015ja022231, 2016.

Jacobi, C., Jakowski, N., Schmidtke, G., and Woods, T. N.: Delayed response of the global total electron content to solar EUV variations, Adv. Radio Sci., 14, 175–180, https://doi.org/10.5194/ars-14-175-2016, 2016.

Jakowski, N., Fichtelmann, B., and Jungstand, A.: Solar activity control of ionospheric and thermospheric processes, J. Atmos. Terr. Phys., 53, 1125–1130, https://doi.org/10.1016/0021-9169(91)90061-b, 1991.

Jin, H., Miyoshi, Y., Pancheva, D., Mukhtarov, P., Fujiwara, H., and Shinagawa, H.: Response of migrating tides to the stratospheric sudden warming in 2009 and their effects on the ionosphere studied by a whole atmosphere-ionosphere model GAIA with COSMIC and TIMED/SABER observations, J. Geophys. Res.-Space, 117, A10323, https://doi.org/10.1029/2012ja017650, 2012.

Klipp, T. S., Petry, A., de Souza, J. R., Falcão, G. S., de Campos Velho, H. F., de Paula, E. R., Antreich, F., Hoque, M., Kriegel, M., Berdermann, J., Jakowski, N., Fernandez-Gomez, I., Borries, C., Sato, H., and Wilken, V.: Evaluation of ionospheric models for Central and South Americas, Adv. Space Res., 64, 2125–2136, https://doi.org/10.1016/j.asr.2019.09.005, 2019.

LASP: EVE Data, available at: http://lasp.colorado.edu/eve/data_access/evewebdata, last access: 15 August 2018a.

LASP: F10.7 index, available at: http://lasp.colorado.edu/lisird/data/noaa_radio_flux/, last access: 15 August 2018b.

Lean, J. L., Warren, H. P., Mariska, J. T., and Bishop, J.: A new model of solar EUV irradiance variability 2. Comparisons with empirical models and observations and implications for space weather, J. Geophys. Res.-Space, 108, 1059, https://doi.org/10.1029/2001ja009238, 2003.

Lean, J. L., Woods, T. N., Eparvier, F. G., Meier, R. R., Strickland, D. J., Correira, J. T., and Evans, J. S.: Solar extreme ultraviolet irradiance: Present, past, and future, J. Geophys. Res.-Space, 116, A01102, https://doi.org/10.1029/2010ja015901, 2011.

Lee, C.-K., Han, S.-C., Bilitza, D., and Seo, K.-W.: Global characteristics of the correlation and time lag between solar and ionospheric parameters in the 27-day period, J. Atmos. Sol.-Terr. Phy., 77, 219–224, https://doi.org/10.1016/j.jastp.2012.01.010, 2012.

Liu, H., Tao, C., Jin, H., and Nakamoto, Y.: Circulation and Tides in a Cooler Upper Atmosphere: Dynamical Effects of CO_2 Doubling, Geophys. Res. Lett., 47, e2020GL087413, https://doi.org/10.1029/2020gl087413, 2020.

Liu, H.-L., Bardeen, C. G., Foster, B. T., Lauritzen, P., Liu, J., Lu, G., Marsh, D. R., Maute, A., McInerney, J. M., Pedatella, N. M., Qian, L., Richmond, A. D., Roble, R. G., Solomon, S. C., Vitt, F. M., and Wang, W.: Development and Validation of the Whole Atmosphere Community Climate Model With Thermosphere and Ionosphere Extension (WACCM-X 2.0), J. Adv. Model. Earth Sy., 10, 381–402, https://doi.org/10.1002/2017ms001232, 2018.

Liu, L., Wan, W., Ning, B., and Zhang, M.-L.: Climatology of the mean total electron content derived from GPS global ionospheric maps, J. Geophys. Res.-Space, 114, A06308, https://doi.org/10.1029/2009ja014244, 2009.

Mallat, S.: A Wavelet tour of signal processing: the sparse way, 3rd Edn., Academic Press, Burlington, MA, 832 pp., 2009.

Mendillo, M., Rishbeth, H., Roble, R., and Wroten, J.: Modelling F2-layer seasonal trends and day-to-day variability driven by coupling with the lower atmosphere, J. Atmos. Sol.-Terr. Phy., 64, 1911–1931, https://doi.org/10.1016/s1364-6826(02)00193-1, 2002.

Millward, G. H., Moffett, R. J., Quegan, S., and Fuller-Rowell, T. J.: A coupled thermosphere-ionosphere-plasmasphere model (CTIP), in: Solar-Terrestrial Energy Program: Handbook of Ionospheric Models, edited by: Schunk, R. W., Cent. for Atmos. and Space Sci., Utah State Univ., Logan, Utah, USA, 239–279, 1996.

Miyoshi, Y., Jin, H., Fujiwara, H., and Shinagawa, H.: Numerical Study of Traveling Ionospheric Disturbances Generated by an Upward Propagating Gravity Wave, J. Geophys. Res.-Space, 123, 2141–2155, https://doi.org/10.1002/2017ja025110, 2018.

Negrea, C., Codrescu, M. V., and Fuller-Rowell, T. J.: On the validation effort of the Coupled Thermosphere Ionosphere Plasmasphere Electrodynamics model, Space Weather, 10, S08010, https://doi.org/10.1029/2012sw000818, 2012.

Noll, C. E.: The crustal dynamics data information system: A resource to support scientific analysis using space geodesy, Adv. Space Res., 45, 1421–1440, https://doi.org/10.1016/j.asr.2010.01.018, 2010.

Pancheva, D., Schminder, R., and Laštovička, J.: 27-day fluctuations in the ionospheric D-region, J. Atmos. Terr. Phys., 53, 1145–1150, https://doi.org/10.1016/0021-9169(91)90064-e, 1991.

Percival, D. B. and Walden, A. T.: Wavelet Methods for Time Series Analysis, Cambridge University Press, Cambridge, UK, https://doi.org/10.1017/CBO9780511841040, 2000.

Pesnell, W. D., Thompson, B. J., and Chamberlin, P. C.: The Solar Dynamics Observatory (SDO), Sol. Phys., 275, 3–15, https://doi.org/10.1007/s11207-011-9841-3, 2011.

Quegan, S., Bailey, G., Moffett, R., Heelis, R., Fuller-Rowell, T., Rees, D., and Spiro, R.: A theoretical study of the distribution of ionization in the high-latitude ionosphere and the plasmasphere: first results on the mid-latitude trough and the light-ion trough, J. Atmos. Terr. Phys., 44, 619–640, https://doi.org/10.1016/0021-9169(82)90073-3, 1982.

Ren, D., Lei, J., Wang, W., Burns, A., Luan, X., and Dou, X.: Does the Peak Response of the Ionospheric F_2 Region Plasma Lag the Peak of 27-Day Solar Flux Variation by Multiple Days?, J. Geophys. Res.-Space, 123, 7906–7916, https://doi.org/10.1029/2018ja025835, 2018.

Richards, P. G., Fennelly, J. A., and Torr, D. G.: EUVAC: A solar EUV Flux Model for aeronomic calculations, J. Geophys. Res.-Space, 99, 8981–8992, https://doi.org/10.1029/94ja00518, 1994.

Richmond, A. D., Ridley, E. C., and Roble, R. G.: A thermosphere/ionosphere general circulation model with coupled electrodynamics, Geophys. Res. Lett., 19, 601–604, https://doi.org/10.1029/92gl00401, 1992.

Ridley, A., Deng, Y., and Tóth, G.: The global ionosphere–thermosphere model, J. Atmos. Sol.-Terr. Phy., 68, 839–864, https://doi.org/10.1016/j.jastp.2006.01.008, 2006.

Romero-Hernandez, E., Denardini, C. M., Takahashi, H., Gonzalez-Esparza, J. A., Nogueira, P. A. B., de Padua, M. B., Lotte, R. G., Negreti, P. M. S., Jonah, O. F., Resende, L. C. A., Rodriguez-Martinez, M., Sergeeva, M. A., Neto, P. F. B., la Luz, V. D., Mon-

ico, J. F. G., and Aguilar-Rodriguez, E.: Daytime ionospheric TEC weather study over Latin America, J. Geophys. Res.-Space, 123, 10345–10357, https://doi.org/10.1029/2018ja025943, 2018.

Schmölter, E., Berdermann, J., Jakowski, N., Jacobi, C., and Vaishnav, R.: Delayed response of the ionosphere to solar EUV variability, Adv. Radio Sci., 16, 149–155, https://doi.org/10.5194/ars-16-149-2018, 2018.

Schmölter, E., Berdermann, J., Jakowski, N., and Jacobi, C.: Spatial and seasonal effects on the delayed ionospheric response to solar EUV changes, Ann. Geophys., 38, 149–162, https://doi.org/10.5194/angeo-38-149-2020, 2020.

Tapping, K. F.: Recent solar radio astronomy at centimeter wavelengths: The temporal variability of the 10.7 cm flux, J. Geophys. Res.-Atmos., 92, 829–838, https://doi.org/10.1029/jd092id01p00829, 1987.

Tobiska, W., Woods, T., Eparvier, F., Viereck, R., Floyd, L., Bouwer, D., Rottman, G., and White, O.: The SOLAR2000 empirical solar irradiance model and forecast tool, J. Atmos. Sol.-Terr. Phy., 62, 1233–1250, https://doi.org/10.1016/s1364-6826(00)00070-5, 2000.

Unglaub, C., Jacobi, C., Schmidtke, G., Nikutowski, B., and Brunner, R.: EUV-TEC proxy to describe ionospheric variability using satellite-borne solar EUV measurements: First results, Adv. Space Res., 47, 1578–1584, https://doi.org/10.1016/j.asr.2010.12.014, 2011.

Vaishnav, R., Jacobi, C., Berdermann, J., Schmölter, E., and Codrescu, M.: Ionospheric response to solar EUV variations: Preliminary results, Adv. Radio Sci., 16, 157–165, https://doi.org/10.5194/ars-16-157-2018, 2018.

Vaishnav, R., Jacobi, C., and Berdermann, J.: Long-term trends in the ionospheric response to solar extreme-ultraviolet variations, Ann. Geophys., 37, 1141–1159, https://doi.org/10.5194/angeo-37-1141-2019, 2019.

Woods, T. and Rottman, G.: Solar ultraviolet variability over time periods of aeronomic interest, in: Atmospheres in the Solar System: Comparative Aeronomy, edited by: Mendillo, M., Nagy, A., and Waite, J., American Geophysical Union, Washington, D.C., USA, 221–233, https://doi.org/10.1029/130gm14, 2002.

Woods, T., Bailey, S., Eparvier, F., Lawrence, G., Lean, J., McClintock, W., Roble, R., Rottman, G., Solomon, S., Tobiska, W., and White, O. R.: TIMED Solar EUV experiment, Phys. Chem. Earth Pt. C, 25, 393–396, https://doi.org/10.1016/s1464-1917(00)00040-4, 2000.

Woods, T., Eparvier, F., Bailey, S. M., Chamberlin, P., Lean, J., Rottman, G., Solomon, S., Tobiska, W., and Woodraska, D.: Solar EUV Experiment (SEE): Mission overview and first results, J. Geophys. Res.-Space, 110, A01312, https://doi.org/10.1029/2004ja010765, 2005.

Woods, T., Eparvier, F., Hock, R., Jones, A., Woodraska, D., Judge, D., Didkovsky, L., Lean, J., Mariska, J., Warren, H., McMullin, D., Chamberlin, P., Berthiaume, G., Bailey, S., Fuller- Rowell, T., Sojka, J., Tobiska, W. K., and Viereck, R.: Extreme Ultraviolet Variability Experiment (EVE) on the Solar Dynamics Observatory (SDO): Overview of Science Objectives, Instrument Design, Data Products, and Model Developments, Sol. Phys., 275, 115–143, https://doi.org/10.1007/s11207-009-9487-6, 2010.

Zou, L., Rishbeth, H., Müller-Wodarg, I. C. F., Aylward, A. D., Millward, G. H., Fuller-Rowell, T. J., Idenden, D. W., and Moffett, R. J.: Annual and semiannual variations in the ionospheric F2-layer. I. Modelling, Ann. Geophys., 18, 927–944, https://doi.org/10.1007/s00585-000-0927-8, 2000.

5 Paper 4: Role of eddy diffusion in the ionospheric delayed response

In this paper, CTIPe model simulations have been performed to consolidate the preliminary results of Vaishnav et al. (2018) and the hypothesis of Jakowski et al. (1991), in order to understand the possible physical mechanisms of the ionospheric delay. Simulations of the ionospheric response to solar flux changes driven by the twenty-seven days solar rotation have been performed. To understand the role of I-T coupling in this study we perform model runs changing the eddy diffusion and solar activity conditions.

An ionospheric delayed response has been investigated by Schmölter et al. (2020) over European stations. They reported an ionospheric delay of about 18 h over these stations. Hence, we emphasis to reproduce and investigate the ionospheric delay response over an European location (40°N) and discuss the physical mechanism.

Our main contributions to scientific understanding of ionospheric delay:

- The ionospheric delay at the solar rotation period is well reproduced and is about 1 d.

- The results of mechanistic studies with CTIPe show that eddy diffusion is an important factor that strongly influences the delay introduced in TEC based on the solar activity conditions. This verifies the hypothesis of Jakowski et al. (1991).

- When eddy diffusion is reduced to 75% of the original value, the delay is slightly longer (about 25 h), while when transport is increased, the delay is reduced to 20 h. An increase in eddy diffusion leads to faster transport processes and an increased loss rate, resulting in a reduction of the ionospheric time delay.

- At low latitudes, the influence of solar activity is stronger, as EUV radiation drives ionization processes that lead to compositional changes. Therefore, the combined effect of eddy diffusion and solar activity shows a larger delay in the low and mid-

latitude region.

The analysis has a few limitations that need to be addressed in future research. Our results suggest that eddy diffusion plays a crucial role in the ionospheric delay. Therefore, further numerical modeling and observational results are needed to understand the profound role of lower atmospheric forcing and T-I coupling. For this study, constant atmospheric conditions were used to understand the role of solar flux and eddy diffusion on ionospheric delay. Further studies are needed in the future to explore the physical processes using actual observations. It would also be interesting to study the combined effect of solar variations, geomagnetic variations, and lower atmospheric forcings.

This paper,**Vaishnav et al., 2021b** is committed to investigate the role of eddy diffusion on the ionospheric delay.

Research paper

[Vaishnav et al., 2021b] Vaishnav, R., Jacobi, C., Berdermann, J., Codrescu, M., and Schmölter, E. (2021). Role of eddy diffusion in the delayed ionospheric response to solar flux changes, Annales Geophysicae, 39, 641–655, 2021, https://doi.org/10.5194/angeo-39-641-2021.

Author contributions statement

The doctoral student performed the following tasks independently for this paper: Conceptualizing the approach, perform CTIPe model run, analyzing the model simulated data, compiling and creating graphs, interpretation and conclusion, and writing the first draft of the paper.

Annales
Geophysicae

Role of eddy diffusion in the delayed ionospheric response to solar flux changes

Rajesh Vaishnav[1], **Christoph Jacobi**[1], **Jens Berdermann**[2], **Mihail Codrescu**[3], **and Erik Schmölter**[2]

[1]Leipzig Institute for Meteorology, Universität Leipzig, Stephanstr. 3, 04103 Leipzig, Germany
[2]German Aerospace Center, Kalkhorstweg 53, 17235 Neustrelitz, Germany
[3]Space Weather Prediction Centre, National Oceanic and Atmospheric Administration, Boulder, Colorado, USA

Correspondence: Rajesh Vaishnav (rajesh_ishwardas.vaishnav@uni-leipzig.de)

Abstract. Simulations of the ionospheric response to solar flux changes driven by the 27 d solar rotation have been performed using the global 3-D Coupled Thermosphere Ionosphere Plasmasphere electrodynamics (CTIPe) physics-based numerical model. Using the F10.7 index as a proxy for solar extreme ultraviolet (EUV) variations in the model, the ionospheric delay at the solar rotation period is well reproduced and amounts to about 1 d, which is consistent with satellite and in situ measurements. From mechanistic CTIPe studies with reduced and increased eddy diffusion, we conclude that the eddy diffusion is an important factor that influences the delay of the ionospheric total electron content (TEC). We observed that the peak response time of the atomic oxygen to molecular nitrogen ratio to the solar EUV flux changes quickly during the increased eddy diffusion compared with weaker eddy diffusion. These results suggest that an increase in the eddy diffusion leads to faster transport processes and an increased loss rate, resulting in a decrease in the ionospheric time delay. Furthermore, we found that an increase in solar activity leads to an enhanced ionospheric delay. At low latitudes, the influence of solar activity is stronger because EUV radiation drives ionization processes that lead to compositional changes. Therefore, the combined effect of eddy diffusion and solar activity leads to a longer delay in the low-latitude and midlatitude region.

1 Introduction

The solar activity plays a significant role in controlling the variations in the thermosphere–ionosphere (T/I) system, in particular through solar extreme ultraviolet (EUV) and ultraviolet (UV) radiation and their variability. In addition, there are several factors which control the behavior of the T/I system, such as tidal and gravity wave forcing from the lower atmosphere, neutral winds, and related currents in the ionosphere. These are especially predominant during low solar activity, leading to reduced correlation of solar flux and ionospheric electron density then (Vaishnav et al., 2019). The ionosphere itself is created through photoionization of the major constituents (atomic oxygen, molecular nitrogen, and molecular oxygen), while photodissociation may change the mixing ratios of these constituents (especially atomic oxygen), leading to modifications of the ionization rates.

Due to these varying ionization rates for different atoms and molecules, a series of layers of electron density forms, known as D, E, F1, and F2 regions. The maximum peak of electron density is observed in the F2 region. The F2 region electron densities mainly depend on photochemical processes, such as photodissociation, photoionization, and loss by recombination with molecular nitrogen, and transport processes, such as neutral wind and diffusion. On top of this, there are many processes which can drive or disturb the ionospheric ion distribution, such as diffusion, transport, cooling, and heating mechanisms. Transport can be divided into three main categories, namely eddy diffusion, molecular diffusion, and advection processes (Brasseur and Solomon, 2005). The

F2 region is strongly influenced by the global thermospheric circulation (Rishbeth, 1998).

The physical mechanism of the delayed ionospheric response cannot be explained with solar variations, seasonal variations, or changes due to geomagnetic activity. We also cannot explain the delay with photoionization and photodissociation processes alone. This has been discussed in several studies (Jakowski et al., 1991; Schmölter et al., 2018, 2020, and references therein), and the importance of the T/I coupling was pointed out. The T/I coupling is important for the delay. This has been mentioned in several studies by now but has scarcely been investigated. The most important impacts we would expect due to this coupling are compositional changes that can impact the major processes, and this could be due to gravity-wave-induced diffusion.

The lower thermospheric composition is not only influenced by gravity waves, but also by other parts of the lower atmospheric wave spectrum, including atmospheric tides and planetary waves. The main source of eddy diffusion is breaking of gravity waves. Gravity waves are usually generated in the lower atmosphere by various mechanisms such as convection, wind shears, storms, and airflow over mountains. Their amplification and wave breaking due to instabilities produces mixing (Li et al., 2005). Atmospheric tidal and planetary wave activity can also significantly contribute to eddy diffusion. For example, the tides induce a net transport of atomic oxygen via the mean meridional circulation generated by tidal dissipation (Jones et al., 2014a, b). Above the mesopause, the intradiurnal variability associated with atmospheric tides strongly affects the transport of NO_x (Meraner and Schmidt, 2016), and seasonally varying gravity wave and tidal mixing influence the mesosphere–lower thermosphere (MLT) region (Qian et al., 2013). Moreover, the possible role in the semiannual oscillation in thermospheric mass density is discussed by Jones et al. (2018). Siskind et al. (2014) showed that the vertical transport by nonmigrating tides causes a significant reduction in the calculated peak electron density of the ionospheric F2 layer.

Several studies have reported the influence of gravity waves and turbulence on the T/I composition and calculated the eddy diffusion coefficient in the MLT region (Kirchhoff and Clemesha, 1983; Sasi and Vijayan, 2001; Swenson et al., 2019). Based on radar measurements, Kirchhoff and Clemesha (1983) calculated a minimum (maximum) eddy diffusion coefficient of 45 (123) $m^2 s^{-1}$ during fall (summer). Similarly, Sasi and Vijayan (2001) used Doppler radar observations and show that the eddy diffusion varies from 25 to 300 $m^2 s^{-1}$ during September and June.

Turbulent mixing is an important process affecting the composition of the T/I system. The effect of turbulence on different minor and major species has been discussed on several occasions (e.g., Keneshea and Zimmerman, 1970; Shimazaki, 1971; Chandra and Sinha, 1974; Rishbeth et al., 1987; Rees and Fuller-Rowell, 1988; Fuller-Rowell and Rees, 1992; Danilov and Konstantinova, 2014; Pilinski and

Crowley, 2015; Swenson et al., 2018). Various coupled models have been developed to understand the T/I region variations, considering the availability of experimental and theoretical knowledge. Earlier 1-D models, which include eddy diffusion coefficients, have been used to model the T/I region (e.g., Colegrove et al., 1965; Shimazaki, 1971; Jakowski et al., 1991). Nowadays, more improved, 3-D models like the Coupled Thermosphere Ionosphere Plasmasphere Electrodynamics (CTIPe) model (Fuller-Rowell and Rees, 1980) or the National Center for Atmospheric Research (NCAR) Thermosphere–Ionosphere–Electrodynamics General Circulation Model (TIE-GCM) (Richmond et al., 1992) are available to explore the dynamics of the T/I region. These models cannot be expected to reproduce the real ionospheric variability exactly due to limited knowledge of various processes in the T/I region and their corresponding inputs (e.g., Shim et al., 2011; Codrescu et al., 2012), but they are capable of providing insight into relevant dynamical processes in the T/I.

Rees and Fuller-Rowell (1988) used a sinusoidal eddy turbulence profile and analyzed the effect of eddy turbulence on temperature, atomic oxygen, and nitric oxide. They showed that an increase in turbulence near the mesopause leads to an increase in atomic oxygen and nitric oxide. This leads to a change in the thermal structure by strongly modifying the gravity wave flux.

The solar radiation reaching the Earth exhibits a periodicity of about 27 d, owing to the solar rotation. As a result, the T/I system also varies with this periodicity. Many studies revealed a delay in ionospheric parameters, such as total electron content (TEC, given in TEC units, 1 TECU = 10^{16} electrons m^{-2}), electron density, peak electron density of F_2 region (NmF2, cm^{-3}), and the corresponding height (hmF2, km), to the 27 d solar flux variation (Jakowski et al., 1991; Liu et al., 2006; Afraimovich et al., 2008; Lee et al., 2012; Anderson and Hawkins, 2016; Jacobi et al., 2016; Schmölter et al., 2018, 2020, 2021; Vaishnav et al., 2018, 2021; Ren et al., 2018, and references therein). Most of the studies found an ionospheric delay of about 1–2 d, with a possible uncertainty of about half a day. Schmölter et al. (2018), using high temporal resolution data, found an ionospheric delay of about 17–19 h using TEC and Geostationary Operational Environmental Satellite (GOES) EUV datasets. The detailed seasonal and spatial effect on the ionospheric delay was studied by Schmölter et al. (2020). Their study revealed a strong geomagnetic effect on the ionospheric delay. They also noticed that the delay over Southern Hemisphere stations is larger than over Northern Hemisphere stations.

Numerical simulations using a 1-D model have revealed that the delay might be due to the slow diffusion of atomic oxygen at 180 km height, generated by solar UV radiation in the Schumann–Runge continuum, causing photodissociation of molecular oxygen above the turbopause (Jakowski et al., 1991).

Ren et al. (2018) investigated the ionospheric time delay using observations and simulations with the TIE-GCM model. They discussed the possible role of ion production and loss mechanisms and the O/N_2 ratio in the ionospheric delay against the solar EUV flux. A strong effect of geomagnetic activity was reported. The ionospheric response time is controlled by photochemical, dynamical, and electrodynamical processes. Ren et al. (2019) suggested that the time delay in thermospheric temperature is due to the difference between the total heating and cooling rates. The study also found a possible role of the general circulations in the upper atmosphere in the time delay. Similarly, the peak response time of the neutral mass density corresponds to the time of equilibrium between the effect of the barometric process and the change in its abundance (Ren et al., 2020). Moreover, Ren et al. (2021) suggest the possible role of geomagnetic activity in the time delay of the thermospheric mass density, which varies with altitude, latitude, and local time.

Despite such a general understanding, however, the exact mechanism of the ionospheric delay needs further investigation. Therefore, here we attempt to quantify the process which is probably responsible for the ionospheric delay using the CTIPe model (Fuller-Rowell and Rees, 1980). Vaishnav et al. (2018) indicated that transport processes might play an important role in the ionospheric delay observed in TEC using CTIPe model simulations. Based on this assumption, numerical simulations have been performed to consolidate the preliminary results of Vaishnav et al. (2018) and the hypothesis of Jakowski et al. (1991) and to explain the physical mechanisms of the ionospheric delay. To understand the role of T/I coupling in this study, we perform model runs changing the eddy diffusion.

An ionospheric delayed response has been investigated by Schmölter et al. (2020) over European stations. They reported an ionospheric delay of about 18 h over these stations. Therefore, in this paper, the emphasis is to reproduce and investigate the ionospheric delay response over a European location (40° N).

2 CTIPe model simulations

The CTIPe model is used to understand the influence of eddy diffusion in the neutral composition and its role in the delay mechanism. The CTIPe model is an advanced version of the CTIM model (Fuller-Rowell et al., 1987) and is a global, first-principle, nonlinear, time-dependent, 3-D, numerical, physics-based coupled thermosphere–ionosphere–plasmasphere model consisting of four fully coupled distinct components, namely, (a) a neutral thermosphere model (Fuller-Rowell and Rees, 1980); (b) a high-latitude ionosphere convection model (Quegan et al., 1982); (c) a midlatitude and low-latitude ionosphere plasmasphere model (Millward et al., 1996); and (d) an electrodynamics model (Richmond et al., 1992). The thermosphere component of the CTIPe model solves the continuity, momentum, and energy equations to calculate the wind components, global temperature, and composition.

The transport terms particularly specify the $E \times B$ drift and include ion-neutral interactions under the effect of the magnetospheric electric field. The geographic latitude/longitude resolution is 2°/18°. In the vertical direction, the atmosphere is divided into 15 logarithmic pressure levels at an interval of one scale height, starting with a lower boundary at 1 Pa (about 80 km altitude) to above 500 km altitude at pressure level 15. The high-latitude ionosphere (poleward of geomagnetic coordinates 55° N/S) and the midlatitude and low-latitude ionosphere and plasmasphere are implemented as separate components, and there is an artificial boundary between these two model components. The equations for the neutral thermosphere model are solved self-consistently with a high-latitude ionosphere model (Quegan et al., 1982). The numerical solution of the composition equation describes transport, turbulence, and diffusion of atomic oxygen, molecular oxygen, and nitrogen (Fuller-Rowell and Rees, 1983). External inputs are needed to run the model, such as solar UV and EUV, Weimer electric field, TIROS/NOAA auroral precipitation (note, however, that particle precipitation is turned off during our simulations), and tidal forcing from the Whole Atmosphere Model (WAM). The F10.7 index (Tapping, 1987) is used as a solar proxy for calculating ionization, heating, and oxygen dissociation processes. Within CTIPe, a reference solar spectrum based on the EUVAC model (Richards et al., 1994) and the Woods and Rottman (2002) model, driven by variations of F10.7 input, is used. The EUVAC model is used for the wavelength range from 5 to 105 nm and the Woods and Rottman (2002) model from 105 to 175 nm. Solar flux is obtained from the reference spectra using the following equation:

$$f(\lambda) = f_{\text{ref}}(\lambda)[1 + A(\lambda)(P - 80)], \tag{1}$$

where f_{ref} and A are the reference spectrum and a solar variability factor, and $P = 0.5 \times (\text{F10.7} + \text{F10.7}A)$, where F10.7$A$ is the average of F10.7 over 41 d. Detailed information on the CTIPe model is available in Codrescu et al. (2008, 2012).

In this paper, our primary goal is to understand the influence of eddy diffusion on the ionospheric response during the 27 d solar rotation. Therefore, several model runs were performed in this study with different diffusion conditions under different artificial solar activity conditions. Three runs were performed with sinusoidally varying solar activity from 75–125 sfu, keeping all other conditions constant. Constant atmospheric and astronomical conditions of 15 March 2013 were used to perform these experiments.

Several authors have suggested that the eddy diffusion is strongly varying based on the months or seasons (e.g., Kirchhoff and Clemesha, 1983; Sasi and Vijayan, 2001; Swenson et al., 2019). Therefore, the experiments were performed using an eddy diffusion coefficient K_T, which amounts to 75 %,

100 %, and 125 % of the original values in the model, and we refer to these runs as $K_T \times 0.75$, $K_T \times 1.0$, and $K_T \times 1.25$, where $K_T \times 1.0$ represents the reference run.

3 Mechanistic studies

In the CTIPe model, the T/I composition is calculated by combining the continuity equation with the diffusion equation. The model estimates changes in the composition of the major species (O, O_2, and N_2) self-consistently, including wind and temperature (Fuller-Rowell and Rees, 1983), as well as molecular diffusion, production, and loss mechanisms.

The continuity equation for the mass mixing ratio, $\psi_i = (n_i \cdot m_i)/\rho$ of the ith species, with n_i as number density, m_i as the molecular mass, and ρ as atmospheric density, may be written as

$$\frac{\partial \psi_i}{\partial t} = \frac{1}{\rho}(m_i S_i) - \boldsymbol{V} \cdot \nabla \psi_i - \omega \frac{\partial \psi_i}{\partial p}$$
$$- \frac{1}{\rho} \nabla \cdot (n_i m_i \boldsymbol{C}_i) + \frac{1}{\rho} \nabla \cdot (K_T n \nabla m \psi_i), \qquad (2)$$

where S_i represents sources and sinks of the species, K_T is the eddy diffusion coefficient, $\boldsymbol{V}$ is the horizontal neutral wind vector, n is the total number density, m is the mean molecular mass, and $\boldsymbol{C}_i$ is the diffusion velocity of the ith species. The terms on the right-hand side of Eq. (2) are, in their respective order, sources and sinks of species, horizontal advection, vertical advection, molecular diffusion, and eddy diffusion.

The mathematical form of the eddy diffusion coefficient K_T used in the CTIPe model as a function of height is given by Shimazaki (1971) and Fuller-Rowell and Rees (1992):

$$K_T = D \exp\left(-A_1(h - h_o)^2\right) \quad h \geq h_o, \qquad (3)$$

$$K_T = (D - D_o) \exp\left(-A_2(h - h_o)^2\right)$$
$$+ D_o \exp\left(-A_3(h - h_o)\right) \quad h \leq h_o. \qquad (4)$$

A peak value of $D = 150\,\text{m}^2\,\text{s}^{-1}$ at $h_o = 105\,\text{km}$ altitude and $D_o = 100\,\text{m}^2\,\text{s}^{-1}$ is used for the $K_T \times 1.0$ reference run. The shape parameters $A_1 = 0.03$, $A_2 = 0.03$, and $A_3 = 0.05$ are taken from Shimazaki (1971). As pointed out by Fuller-Rowell and Rees (1992), eddy diffusion has the greatest influence on atomic oxygen and nitric oxide in the lower thermosphere. A detailed description of the chemistry of the major species is available in Fuller-Rowell (1984).

In our experiments, the CTIPe model was first run with constant F10.7 input for 10 d to achieve a diurnally reproducible condition, and after this spin-up, F10.7 was modified for 27 d using a sine function:

$$\text{F10.7}(t) = 100 - 25 \cos\left(\frac{2\pi t}{27}\right), \qquad (5)$$

where t represents the time in days.

The various terms of the composition equation are shown in Fig. 1 for the noontime (12:00 UT) for the atomic oxygen mass mixing ratio (ψ_O) at 40° N, 18° E in the reference run. The figure shows the behavior of all terms at pressure level 12 (260 km). The vertical dashed red line shows the maximum of the input solar flux as per Eq. (2). Figure 1a shows that the molecular diffusion term shows a delay of less than 1 d for ψ_O. The horizontal and vertical advection are decreasing with the increasing input solar flux with a delay of less than 1 d and 1 d, respectively (Fig. 1b). Similar variations can be seen in the chemical production and loss terms (source and sink term). The delay between production and loss is about 1–2 d in the case of ψ_O, as shown in Fig. 1c. The change in the production term in the composition equation is based on the photoionization processes contributing to ψ_O.

Ren et al. (2020) discussed the physics behind the time delay in different thermospheric neutrals. They found that the peak response time of the mass density of the neutrals (O and N_2) corresponds to the time of equilibrium between the effect of the barometric process and the change in their abundance.

Figure 2 shows the daily zonal mean TEC for three different runs with different eddy diffusion coefficients as a function of time and magnetic latitude. The zonal averages represent the average TEC values over all longitudes at a specific magnetic latitude. In the CTIPe model, TEC is calculated over the altitude range from 80 to 2000 km. In Fig. 2, the zonal mean TEC is shown by the contours, and the white curves show the corresponding variability of the F10.7 index. Here, moderate solar activity conditions (75–125 sfu) have been used.

The daily zonal mean TEC show the overall effect of solar flux on the T/I system, since we used constant atmospheric and astronomical conditions for these simulations.

The results from the reference run $K_T \times 1.0$, with the original value of the eddy diffusion coefficient, are shown in Fig. 2b. The simulations reproduce the real latitudinal as well as temporal variations with the variability in the solar flux. The zonal mean TEC distributions are symmetric around the geomagnetic equator, with maximum amplitudes of about 70 TECU. The TEC values decrease towards the high latitudes. The distribution of TEC highly depends on the ionization of neutrals and various processes such as transport and recombination. The TEC amplitude variations reflect the effects of solar activity and compositional changes.

The $K_T \times 0.75$ run results are shown in Fig. 2a. It shows an increase of TEC in the low-latitude to midlatitude region in comparison to the reference run. The reduction of turbulence leads to slower transport and an increase in TEC. Figure 2c shows the zonal mean TEC for the $K_T \times 1.25$ run. In comparison to the reference run, TEC is reduced by a significant amount. These results show that eddy diffusion has a direct impact on TEC.

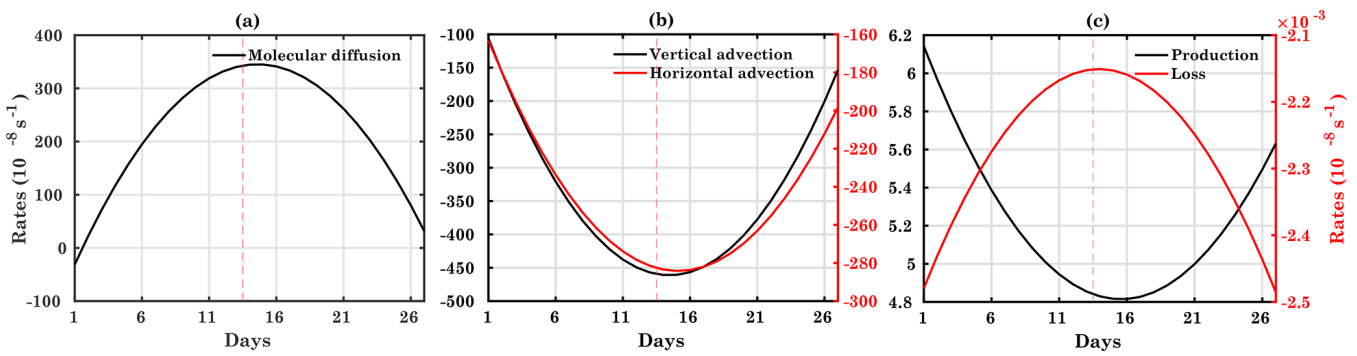Figure 3a shows the global mean TEC (GTEC) as simulated by the three different runs along with the F10.7 in-

Figure 1. Time series of different terms: **(a)** molecular diffusion, **(b)** horizontal advection and vertical advection, and **(c)** production and loss for atomic oxygen mass mixing ratio. Both the y axes are marked with the corresponding color. The vertical dashed red line represents the middle of the 13th model day. All the parameters are plotted for pressure level 12 (260 km) for noontime at 40° N, 18° E.
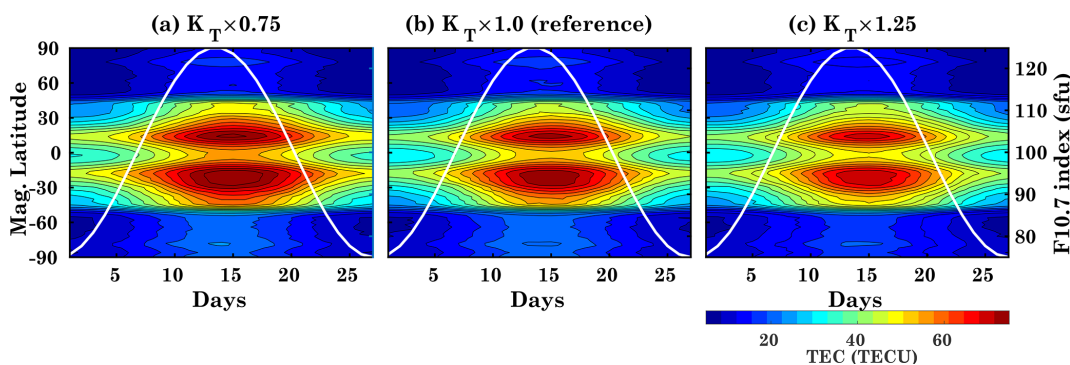

Figure 2. CTIPe-simulated daily mean zonal mean TEC for the runs **(a)** $K_T \times 0.75$, **(b)** $K_T \times 1.0$ (reference), and **(c)** $K_T \times 1.25$. The white curves show the F10.7 index input.

dex (white curve). It shows an obvious 27 d variation of GTEC corresponding to the F10.7 index variations but with a slightly different delay for the different runs. The GTEC values vary from about 8 TECU to maximum values of about 15 TECU for the reference run, corresponding to the solar flux variation. It can be seen that TEC increases linearly with F10.7. In comparison to the reference run, TEC values decreased significantly for the increased eddy diffusion condition, while it is increased for the reduced eddy diffusion conditions (see also Fig. 2).

The model F10.7 index input has been calculated according to Eq. (5) but as hourly values in order to calculate the delay and cross-correlation between GTEC and F10.7, which are shown in Fig. 3b.

For the reference run $K_T \times 1.0$, the delay is about 24 h, which is close to the value derived from observations as reported by Schmölter et al. (2018, 2020). Therefore, the model is capable of reproducing the observed ionospheric delay. In the case of reduced eddy diffusion to 75 % of the original value in run $K_T \times 0.75$, the delay is somewhat longer (about 25 h). This indicates that the delay increases due to the slower transport processes in this run. In line with this, with increased transport in the $K_T \times 1.25$ run, the delay reduces

to 20 h. These results suggest that an increase in the eddy diffusion leads to faster transport processes and an increased loss rate, resulting in a decrease of the ionospheric time delay. The loss rates are discussed below. The ionospheric time delay is mainly due to the imbalance between the production and loss of the ions and electrons (Ren et al., 2018).

We also analyzed the model results separately for the Northern Hemisphere (NH) and the Southern Hemisphere (SH), but the differences between the hemispheres are small and amount to 3, 4, and 4 h for the $K_T \times 0.75$, $K_T \times 1.0$, and $K_T \times 1.25$ runs, respectively (not shown).

Figure 4 shows the variation of the time delay at low [±30°], middle [± (30–60°)], and high [± (60–90°)] geomagnetic latitudes for different eddy diffusion conditions. At low latitudes (Fig. 4a), the delay is more sensitive to eddy diffusion than at middle and high latitudes, as this region is not only controlled by the EUV. Here, dynamics plays an essential role, especially in the equatorial ionization anomaly. Thus, small changes in eddy diffusion can lead to a more significant change in the ionospheric delay. In general, the delay at low latitudes is longer than for the global average in Fig. 3. For the $K_T \times 1.25$ run, the delay is reduced by 4 h compared to the reference run.
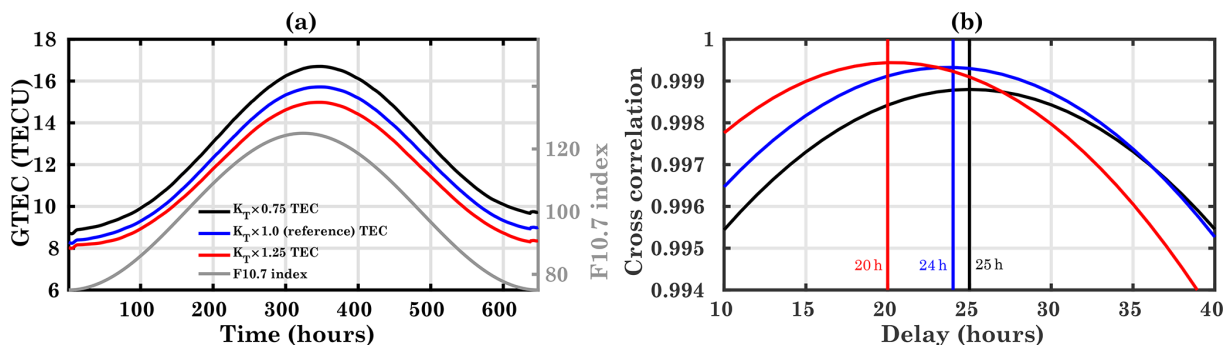
Figure 3. (a) Time series of modeled GTEC for different runs **(a)** $K_T \times 0.75$, **(b)** $K_T \times 1.0$ (reference), and **(c)** $K_T \times 1.25$, together with F10.7 given as a gray line. **(b)** Cross-correlation and the delay between global mean TEC and F10.7 for the different runs.
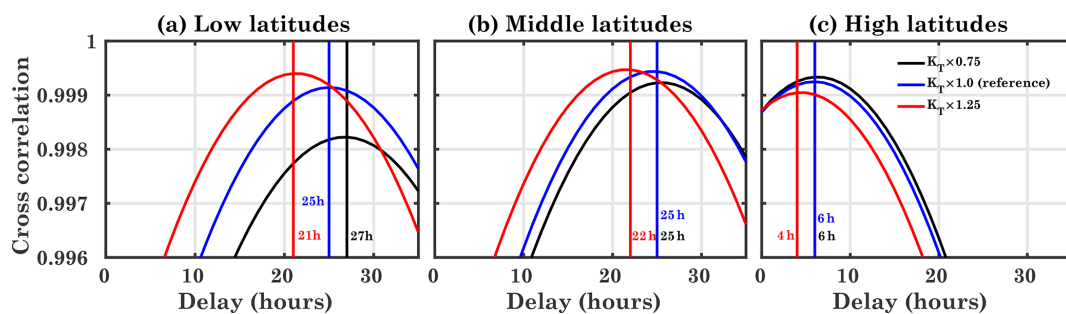

Figure 4. Cross-correlation and the delay between regional mean TEC and the F10.7 index at low **(a)**, middle **(b)**, and high **(c)** geomagnetic latitudes for different runs.

At midlatitudes (Fig. 4b) the delay in the $K_T \times 1.25$ run is about 22 h; i.e., it is longer than on a global average. This is also true for the other runs where the delay is qualitatively the same and amounts to about 25 h. In this region for run $K_T \times 0.75$, the delay is similar to the one of the reference run and is about 25 h.

At high latitudes (Fig. 4c), the variation in the delay is qualitatively the same as at middle and low latitudes; i.e., a decrease in diffusion increases the delay and vice versa. However, at high latitudes, a change in diffusion has a smaller effect, and the delay varies between 4 and 6 h for the different runs. For all runs, the delay is much smaller at high latitudes than at midlatitudes. In comparison to low-latitudes and midlatitudes, the high latitudes show less time delay in run $K_T \times 0.75$. The delay in high latitudes is also less sensitive to diffusion changes compared to the low-latitude and midlatitude regions. Similar to the runs presented in Fig. 3, the model has been run for low solar activity conditions with F10.7 in the range 70–90 sfu and using four different diffusion conditions, $K_T \times 0.5$, $K_T \times 1.0$ (reference), $K_T \times 1.5$, and $K_T \times 2.0$, which amounts to 50 %, 100 %, 125 %, and 150 % of the original values in the model, respectively, as shown in Fig. 5. Figure 5a shows the time series of TEC for different runs and the F10.7 input. In comparison to Fig. 3a, the TEC values are smaller, following the F10.7 index. For these runs, the magnitude of eddy diffusion has

been changed by 50 %. Therefore, significant differences in TEC size are observed. In the reference run, TEC varies from about 8 TEC to 11.3 TECU, while it shows a similar pattern for decreased/increased eddy diffusion with the difference in relative amplitude of TEC. The difference in the TEC curves in Fig. 5a depends on the solar flux and the magnitude of the eddy diffusion coefficient. Also, the delay is calculated using the hourly TEC datasets and the F10.7 index, as shown in Fig. 3a. For the reference run $K_T \times 1.0$, the delay in the simulated GTEC is about 19 h, while the delay increases to 34 h for the $K_T \times 0.5$ run, and it decreases with the increased diffusion conditions. Here, the delay is more sensitive to the eddy diffusion compared to the 25 % change cases, since the solar activity is less dominant. Compared to low solar activity, the eddy diffusion is less dominant in moderate solar activity, and the delay fluctuations are smaller. It should be noted that increasing solar activity leads to an increase in ionospheric delay.

To shed more light on the spatial patterns of the correlation between the F10.7 index and TEC, as well as on the ionospheric delay, the latter is shown in Fig. 6 for each model grid point. Figure 6b shows the spatial map for the reference run $K_T \times 1.0$. Maximum longitudinal differences are observed in the low-latitude and midlatitude region. Near the equatorial region, the delay varies from 10 to 40 h. At high latitudes, the delay is about 0 to 10 h.
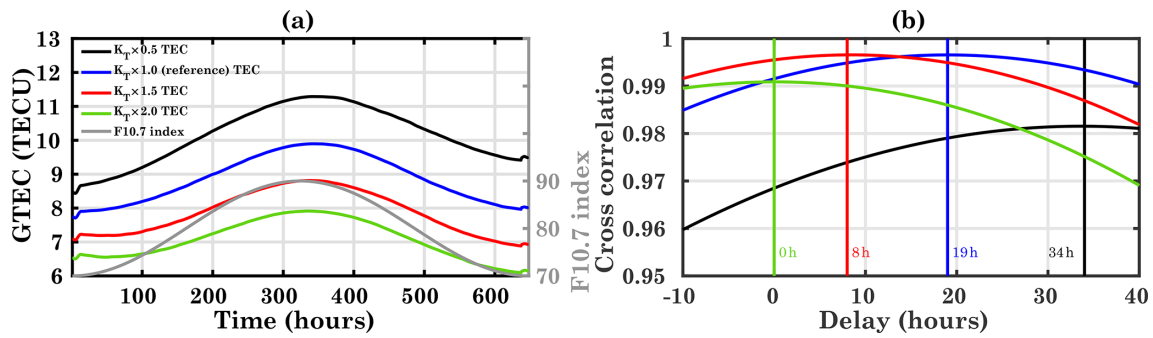
Figure 5. (a) Time series of modeled TEC for the different diffusion conditions $K_T \times 0.5$, $K_T \times 1.0$ (reference), $K_T \times 1.5$, and $K_T \times 2.0$. F10.7 is added as a gray line. **(b)** Cross-correlation and the delay between global mean TEC and F10.7 for the different diffusion conditions.
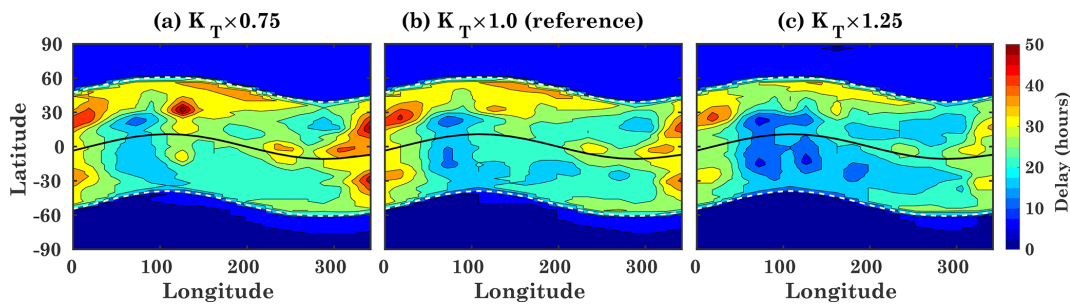

Figure 6. Spatial distribution of time delay between the CTIPe-TEC and the F10.7 index for different transport conditions, **(a)** $K_T \times 0.75$, **(b)** $K_T \times 1.0$ (reference), and **(c)** $K_T \times 1.25$. The black line represents the magnetic equator, and dashed white lines represent magnetic latitudes (55° N/S).
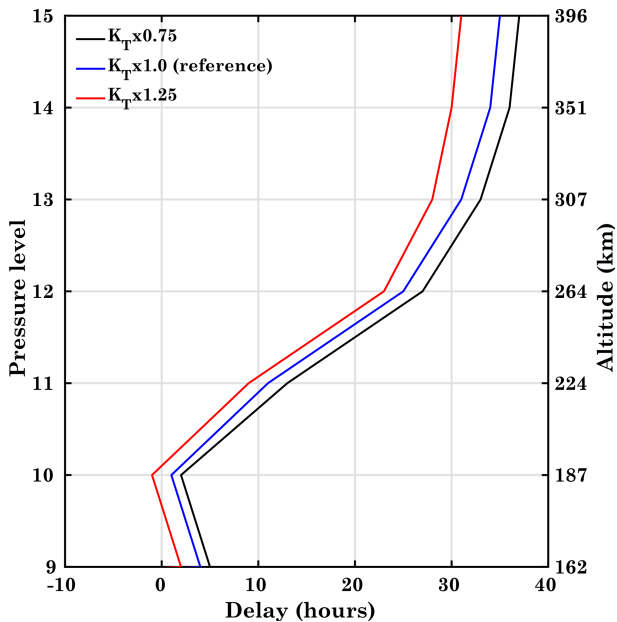
Figure 7. Vertical distribution of time delay between the atomic oxygen ion density and the F10.7 index for different transport conditions, $K_T \times 0.75$, $K_T \times 1.0$ (reference), and $K_T \times 1.25$, at geographic coordinates 40° N, 18° E.

The longitudinal variation of the delay follows the magnetic field. The maximum delay is, in line with the results in Fig. 4, generally observed at lower and middle latitudes.

As is the case with GTEC, at all latitudes, the delay in local TEC is generally increased in run $K_T \times 0.75$ and decreased in run $K_T \times 1.25$ with respect to the $K_T \times 1.0$ run. In the CTIPe model, the low-latitude and midlatitude ionosphere model and the high-latitude ionosphere model are implemented separately. Therefore, the significant change in delay seen at 55° N/S may be owing to model peculiarities in CTIPe.

In the following, we investigate the height variation of the delay using the atomic oxygen ion density at geographic coordinates 40° N, 18° E (magnetic latitude 39.06° N). Figure 7 shows the delay between the atomic oxygen ion density and the F10.7 index at different pressure levels. At pressure level 12 (260 km), the delay is about 24, 18, and 6 h for the different eddy diffusion cases $K_T \times 0.75$, $K_T \times 1.0$, and $K_T \times 1.25$, respectively. The delay continues to increase above pressure level 12, where it is quite close to the delay observed in TEC. This is owing to the fact that the delay observed in TEC is mainly determined by the delay of the F region, i.e., at higher pressure levels (200–260 km).

The eddy diffusion can influence the general circulation and hence the thermospheric neutral species. However, the thermospheric circulation is controlled not only by eddy dif-
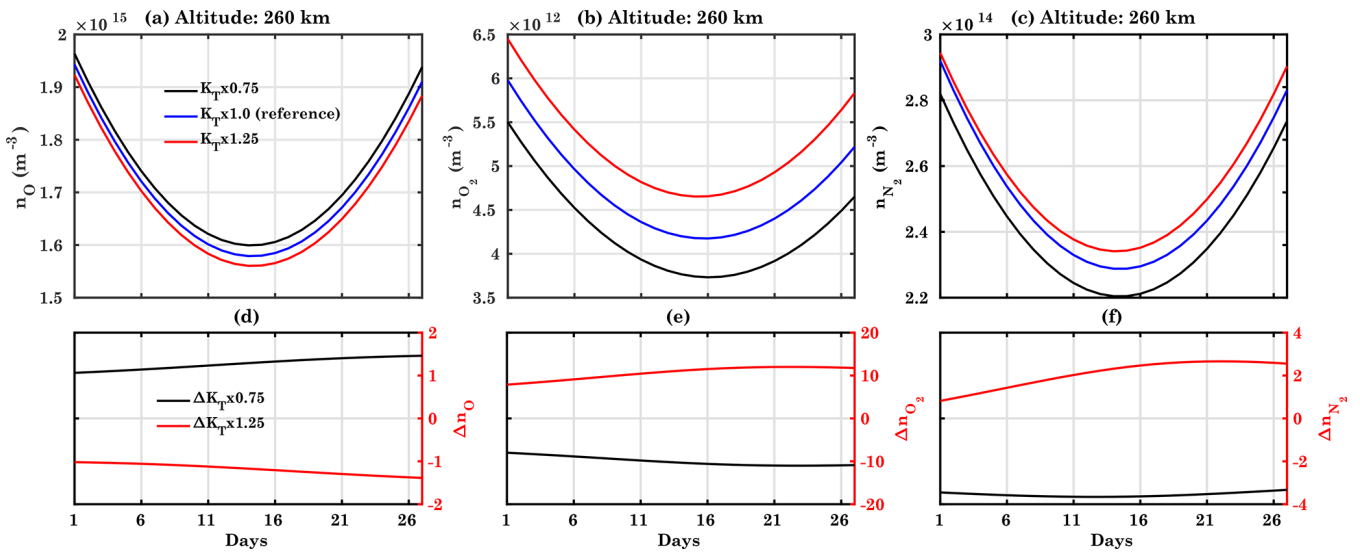
Figure 8. Variation of the CTIPe-simulated **(a)** n_O, **(b)** n_{O_2}, and **(c)** n_{N_2} for different diffusion conditions $K_T \times 0.75$ (black), $K_T \times 1.0$ (blue), and $K_T \times 1.25$ (red) (upper panel) for pressure level 12 (260 km). The percentage difference between the $K_T \times 1.0$ run (blue curve) and the runs with modified eddy diffusion conditions, $K_T \times 0.75$ (black) and $K_T \times 1.25$ (red), is shown in the lower parts of the panels.
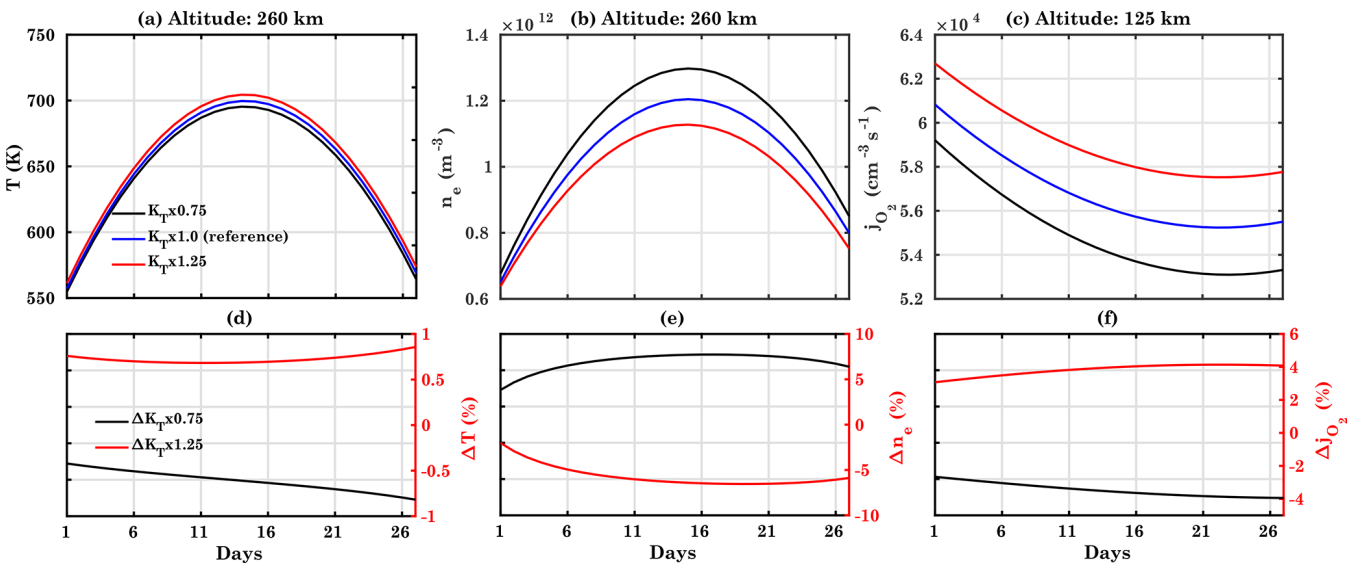

Figure 9. Same as Fig. 8 for **(a)** T, **(b)** n_e for the pressure level 12 ($\sim$ 260 km), and **(c)** j_{O_2} for pressure level 7 ($\sim$ 125 km).

fusion, but also by temperature, pressure, and neutral species, etc. All these parameters are affected by solar EUV radiation. To investigate how eddy diffusion affects the T/I system, we further analyze the evolution of various parameters such as the atomic oxygen number density (n_O), molecular oxygen density (n_{O_2}), molecular nitrogen density (n_{N_2}), molecular oxygen dissociation rates (j_{O_2}), neutral temperature (T), and electron density (n_e). Figures 8 and 9 show the variations of these parameters for the 27 d cycle for the reference run (blue color in the upper panel) and percentage differences (lower panel: on the second y axis) from the reference run

for the other diffusion conditions, $K_T \times 0.75$ and $K_T \times 1.25$, respectively, at geographic coordinates 40° N, 18° E.

Figure 8 shows the variation of n_O, n_{N_2}, and n_{O_2} at pressure level 12 ($\sim$ 260 km). Eddy diffusion has a strong influence on O, N$_2$, and O$_2$. Figure 8a shows the variations of the atomic oxygen density at pressure level 12 for a 27 d solar rotation period. It shows that the atomic oxygen density decreases with increasing solar flux, connected with an increase in temperature, which is shown in Fig. 9a. In comparison to the reference run, the percentage difference increases to about 1 % for the $K_T \times 0.75$ run during the 27 d run. This is partly, but not completely, due to the temperature decrease by
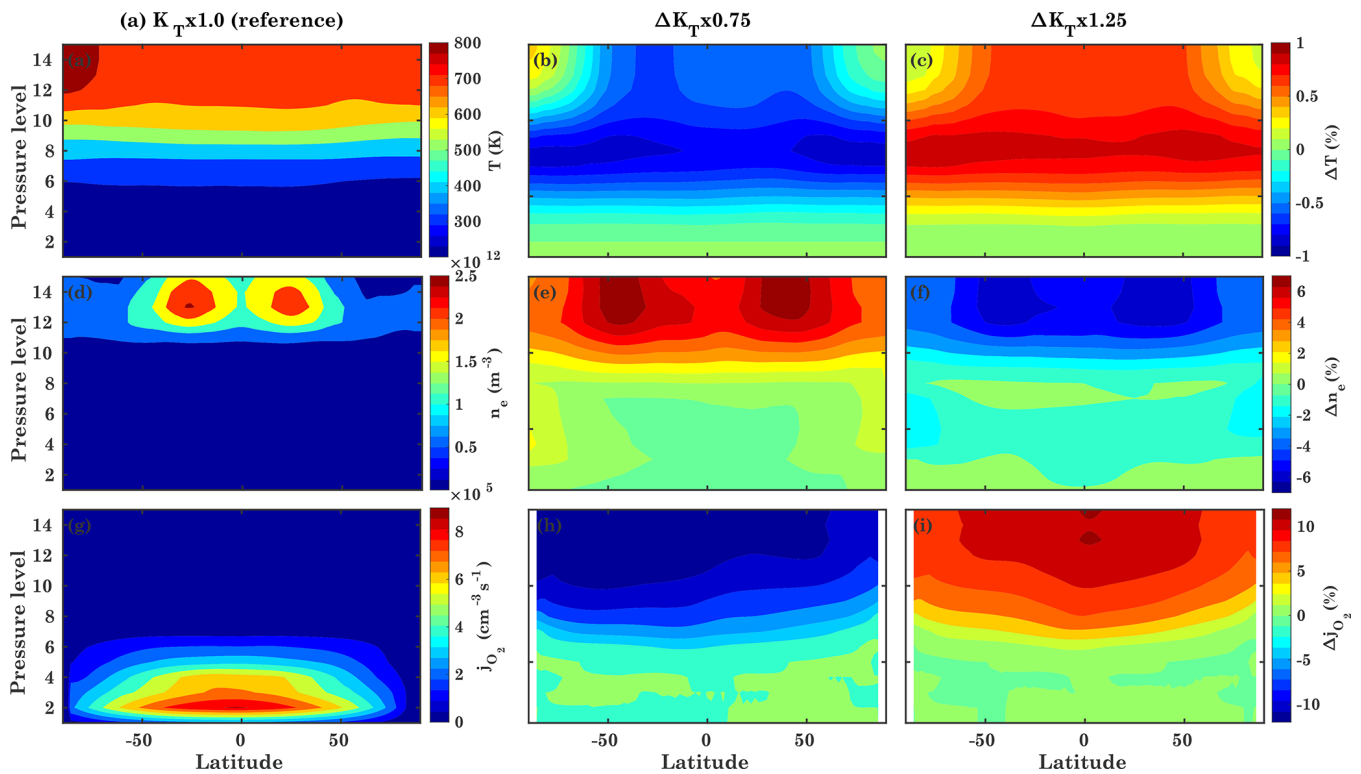
Figure 10. (a) CTIPe-simulated T (upper row), n_e (middle row), and j_{O_2} (bottom row), for the 14th model day. The other columns show the percentage difference between the $K_T \times 1.0$ simulation and the simulations with modified eddy diffusion conditions: **(b)** $K_T \times 0.75$ and **(c)** $K_T \times 1.25$.

$\sim 0.7\%$ (Fig. 9a). Thus, reduced transport leads to reduced atomic oxygen. For the $K_T \times 1.25$ run, the atomic oxygen density decreases by about 1.5 %. These differences are not connected with the solar cycle but evolve gradually over the full time interval.

Similar to the atomic oxygen density variations, the molecular oxygen and nitrogen densities also decrease with increasing solar flux (Fig. 8b and c). For the molecular oxygen density, the percentage difference decreases to about 10 % for the $K_T \times 0.75$ run, while it increases to about 10 % for the $K_T \times 1.25$ run. Similar variations are observed in the behavior of the molecular nitrogen density (Fig. 8c). Once the diffusion increased, the n_{O_2} increases compared to the reference run, demonstrating that diffusion is a critical process to control the evolution of oxygen. Therefore, we register a change in the total composition due to an increase or decrease in eddy diffusion.

Figure 8d and b show the percentage difference between the reference run results and those of the runs with increased or decreased eddy diffusion. For the $K_T \times 0.75$ run, the atomic oxygen density increases to about 1 %, while the molecular oxygen decreases by 10 %. Similar to the molecular oxygen, the molecular nitrogen density also decreases by ~ 3 %. In comparison to $K_T \times 0.75$, opposite trends can be seen for the $K_T \times 1.25$ run.

In Fig. 9a and b, the 27 d behavior at an altitude of ~ 260 km is shown for T and n_e. T increases with increasing solar irradiance. As an increase in solar irradiance expands the range of the thermosphere region, the scale height of each component changes. An increase in solar radiation flux will also increase the height of each pressure level. In Fig. 9e, non-monotonic variations are observed in the difference between the reference run and $K_T \times 1.25$. This could be due to the combined effect of different diffusion cases and solar flux. Compared to the reference case, the temperature decreases by about 0.7 % for the $K_T \times 0.75$ run, while it increases by 0.7 % for the $K_T \times 1.25$ run. Similar to T, n_e also varies with the solar flux. An increase in the solar radiation flux leads to an increase in ionization and thus to an increase in electron density.

The j_{O_2} also vary for different diffusion conditions, as shown in Fig. 9c for pressure level 7 (altitude ~ 125 km). An increase in eddy diffusion reduces j_{O_2}, leading to an increase in n_{O_2} and a reduction in n_O. Exactly the opposite behavior is observed for a decrease in eddy diffusion.

Since we are dealing with vertical transport processes, it is essential to analyze the latitudinal variation against pressure levels. Figure 10 shows the percentage difference of T, j_{O_2}, and n_e in the $K_T \times 0.75$ and $K_T \times 1.25$ runs with respect to $K_T \times 1.0$ for the 14th model day. Figure 10b and
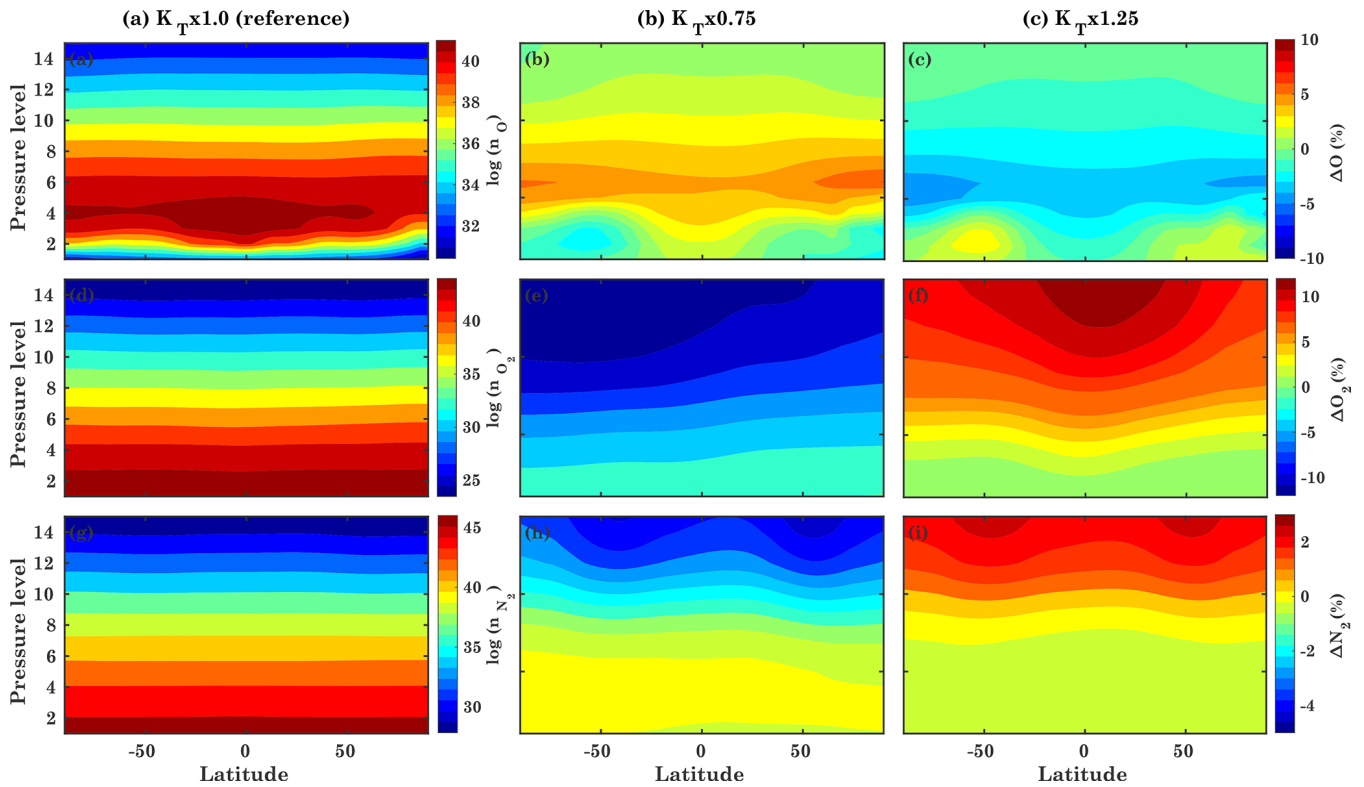
(a) K_Tx1.0 (reference) (b) K_Tx0.75 (c) K_Tx1.25

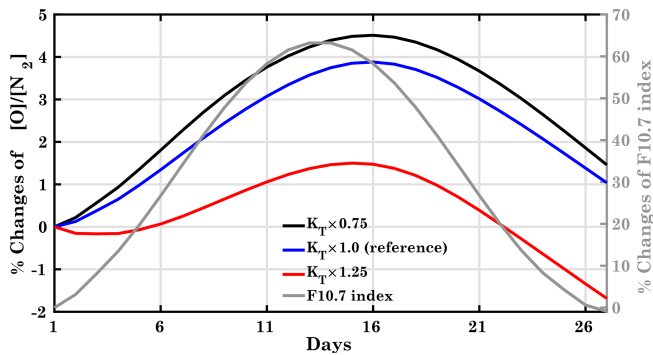**Figure 11.** Same as Fig. 10 but for n_O, n_{O_2}, and n_{N_2}.

Figure 12. Percentage change of the [O]/[N$_2$] ratio for different diffusion conditions, $K_T \times 0.75$, $K_T \times 1.0$ (reference), and $K_T \times 1.25$, at pressure level 12 at geographic coordinates 40° N, 18° E. The right y axis refers to the percentage change of the F10.7 index (gray curve).

c show that due to a decrease/increase in eddy diffusion, T decreases/increases at all pressure levels.

The lowest four pressure levels belong to the lower boundary, where the neutral wind, temperature, and height of the pressure level are imposed as boundary conditions from the WAM model. An increase of the eddy diffusion by a factor of 25 % ($K_T \times 1.25$) leads to an increase in T by 1 %. It mainly affects pressure levels 7–9 (125–160 km). The percentage

difference in T is negligible at pressure levels 5–6 (110 km), but the variations increase with altitude. Figure 10d shows the latitude–pressure distribution of n_e. For the $K_T \times 0.75$ run, it shows that for a reduction in eddy diffusion, n_e is increased in the thermosphere above pressure level 9 (160 km). Interestingly, above this altitude, n_e increases by about 7 %. Electron density increases in the low-latitude region at pressure level 4 (98 km) and in the high-latitude region at pressure level 5 (105 km). The response of the thermosphere n_e to an enhancement of eddy diffusion is entirely different. For the $K_T \times 1.25$ run, n_e decreases at higher pressure levels, but it increases at lower pressure levels, except for midlatitudes at 98 km and high latitudes at 105 km.

The variation in j_{O_2} is shown in Fig. 10g. The percentage difference for the $K_T \times 0.75$ run compared to the reference run decreases by about 7% for pressure levels 5–7 (105–125 km), and it decreases by 7 % for the $K_T \times 1.25$ run.

Figure 11a shows the variation of n_O. For the $K_T \times 0.75$ run, n_O is increased by 5 %–7 % above the turbopause. The enhanced diffusion leads to an increase of n_O in the lower thermosphere due to the downward transport of n_O from higher altitudes (Rees and Fuller-Rowell, 1988). Note that eddy diffusion has a more substantial impact at high latitudes below the turbopause. Chandra and Sinha (1974) showed that due to photochemical effects, the variation of eddy diffusion
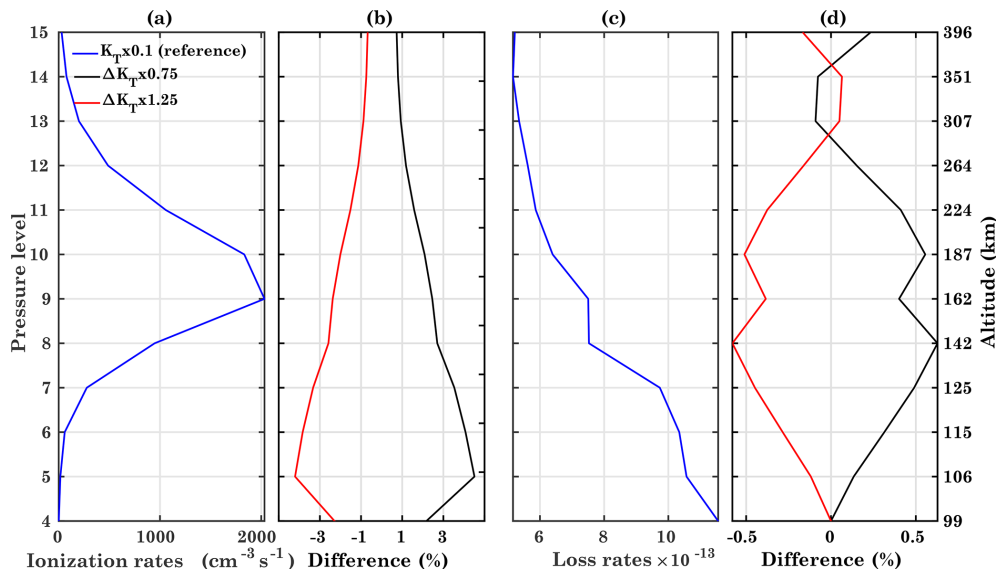
Figure 13. Atomic oxygen ionization (**a**) and loss rates (**c**) due to molecular nitrogen for the reference run $K_T \times 1.0$ and its difference (**b, d**) with $K_T \times 0.75$ and $K_T \times 1.25$ at different pressure levels on the 14th model day at geographic coordinates 40° N, 18° E.

does not contribute significantly to n_O below 100 km, but above 100 km it decreases with increasing eddy diffusion.

Enhanced eddy diffusion leads to an increase in n_{O_2} of about 10 %–12 % above the turbopause in the $K_T \times 1.25$ run, with j_{O_2} decreasing by about 0.5 %, as shown in Fig. 10d. Thus, the decrease in j_{O_2} increases n_{O_2}, and this leads to a decrease in n_O. Similar variations are also observed in the case of enhanced diffusion conditions for n_{N_2}, with an increase of about 2 %–3 % for the enhanced eddy diffusion conditions. The variation in eddy diffusion affects the composition at different altitudes through molecular diffusion.

Enhanced eddy diffusion leads to an increase in molecular oxygen. This leads to a decrease in atomic oxygen at all altitudes above 100 km due to molecular diffusion. As a result, there is a significant decrease in the [O]/[N₂] ratio. Qian et al. (2009) studied the effect of modified eddy diffusion on thermospheric composition using the NCAR TIE-GCM model and reported similar results. These simulations revealed a new finding how eddy diffusion can strongly affect the thermospheric composition (O, O₂, and N₂) through the ionospheric delay.

The steady-state electron density N can be written according to Rishbeth (1998):

$$N \sim \frac{q}{\beta} \sim \frac{I[\text{O}]}{\gamma_1\,[\text{N}_2] + \gamma_2\,[\text{O}_2]}, \tag{6}$$

where q, β, I, and γ_1, γ_2 are the production term, the loss term, the solar ionizing flux, and the reaction rates, respectively.

The composition of the T/I system is mainly controlled by various production and loss mechanisms. The production of electrons is mainly due to the ionization of atomic oxygen through solar EUV, and the loss is mainly controlled by

N₂. The production of atomic oxygen ions depends not only on the atomic oxygen density, but also on the solar radiation. Ren et al. (2018) explained that the delay observed in the electron density depends on the production and loss processes as well as the [O]/[N₂] ratio. The major loss of ions in the F regions is given by the following reactions:

$$\text{O}^+ + \text{N}_2 \rightarrow \text{NO}^+ + \text{N}$$
$$\text{O}^+ + \text{O}_2 \rightarrow \text{O}_2^+ + \text{O}.$$
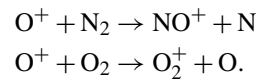
The rate coefficients γ_1 and γ_2 in Eq. (6) are given, e.g., by St.-Maurice and Torr (1978). These reaction rate coefficients are dependent on the effective temperature (T_f), which significantly affects the loss reaction and composition:

$$T_f = 0.63 \times T_i + 0.36 \times T_N. \tag{7}$$

Here T_i and T_N are ion temperature and the neutral temperature, respectively. For low values of $T_f < 1100$ K, the loss rate coefficients γ_1 and γ_2 decrease with increasing T_f, while for $T_f > 1100$ K, the loss rate γ_1 increases as a result of the electron density decrease with increasing F10.7 index. The nonlinear relation between the loss rate coefficients and T_f is shown by Su et al. (1999).

Figure 12 shows the variations of the [O]/[N₂] ratio for different diffusion conditions at geographical latitude/longitude 40° N, 18° E at an altitude of about 260 km (pressure level 12). For the reference run, the delay is about 2–3 d, since the peak response is observed at day 16. The [O]/[N₂] ratio strongly decreases with increasing eddy diffusion, and the delay is also shifted to 1 d. Thus, the variation in eddy diffusion strongly affects the [O]/[N₂] ratio, which in turn affects the delay mechanism.

Figure 13 shows the effect of eddy diffusion on the atomic oxygen ionization (a) and loss rates (c) through molecular nitrogen at 40° N, 18° E, and the difference between the reference run and other diffusion cases is shown in Fig. 13b and d. The reference case $K_T \times 1.0$ and the $K_T \times 0.75$ and $K_T \times 1.25$ runs are represented by blue, black, and red curves, respectively. The maximum ionization occurs at pressure level 9–10 (162–187 km) (Fig. 13a). Figure 13b shows a decrease of ionization rates with enhanced eddy diffusion, whereas they are increased for reduced eddy diffusion. The production term in Eq. (6) depends strongly on the ionization rates and the atomic oxygen density. Therefore, increased eddy diffusion decreases ionization and atomic oxygen density. Figure 13d shows that the loss rates are reduced by about 0.5 % in the F region in the case of enhanced eddy diffusion. Su et al. (1999) discussed the dependence of the loss rates on temperature. They suggested that the loss rate coefficient decreases with increasing T_f. Enhanced eddy diffusion leads to an increase in molecular components while reducing atomic oxygen.

Consequently, enhanced N_2 increases the overall loss term in Eq. (6) and reduces the electron density, resulting in a reduced delay in TEC. Based on the model simulations, we conclude that eddy diffusion is one of the major factors responsible for the changes in thermospheric composition via general circulation and significantly affects the ionospheric delay. Although the current investigation suggests that a small change in loss rates can affect the delay for several hours, further numerical modeling using real observations and varying atmospheric conditions is needed to understand the physical processes.

4 Summary

Using a 1-D model, Jakowski et al. (1991) first reported that the delayed density variation concerning solar EUV variations is probably due to the slow diffusion of atomic oxygen. Based on their hypothesis, the ionospheric delay in TEC, simulated by the CTIPe model, was investigated. Using the F10.7 index, the ionospheric delay at the solar rotation period is well reproduced and amounts to about 1 d (Jacobi et al., 2016; Schmölter et al., 2018). The thermosphere–ionosphere coupling plays an important role in the delay mechanism, and this was reported in several studies, but it was barely investigated. Therefore, this is the first time we investigated the impact of eddy diffusion on the ionospheric delay. To investigate the physical mechanism of ionospheric delay at the solar rotation period, we performed various experiments using CTIPe model. From the mechanistic studies using CTIPe, results show that eddy diffusion is an important factor that strongly influences the delay introduced in TEC based on the solar activity conditions. In the case of reduced eddy diffusion to 75 % of the original value, the delay is slightly longer (about 25 h), while in the case of increased transport, the de-

lay is reduced to 20 h. An increase in eddy diffusion leads to faster transport processes and an increased loss rate, resulting in a reduction of the ionospheric time delay.

At low latitudes, the influence of solar activity is stronger, as EUV radiation drives ionization processes that lead to compositional changes. Therefore, the combined effect of eddy diffusion and solar activity shows more delay in the low-latitude and midlatitude region.

Our results suggest that eddy diffusion plays a crucial role in the ionospheric delay. Therefore, further numerical modeling and observational results are required to better understand the role of lower atmospheric forcings and thermosphere–ionosphere coupling.

For this study, constant atmospheric conditions have been used to understand the role of solar flux and eddy diffusion in the ionospheric delay. In future, further investigation is required to explore the physical processes using actual observations. It would also be interesting to investigate the combined effect of solar variations, geomagnetic variations, and lower atmospheric forcings.

References

Afraimovich, E. L., Astafyeva, E. I., Oinats, A. V., Yasukevich, Y. V., and Zhivetiev, I. V.: Global electron content: a new conception to track solar activity, Ann. Geophys., 26, 335–344, https://doi.org/10.5194/angeo-26-335-2008, 2008.

Anderson, P. C. and Hawkins, J. M.: Topside ionospheric response to solar EUV variability, J. Geophys. Res.-Space, 121, 1518–1529, https://doi.org/10.1002/2015ja021202, 2016.

Brasseur, G. P. and Solomon, S.: Aeronomy of the middle atmosphere: Chemistry and physics of the stratosphere and mesosphere, Vol. 32, 3rd Edn., 646 pp., Springer, Dordrecht, the Netherlands, 2005.

Chandra, S. and Sinha, A. K.: The role of eddy turbulence in the development of self-consistent models of the lower and upper thermospheres, J. Geophys. Res., 79, 1916–1922, https://doi.org/10.1029/ja079i013p01916, 1974.

Codrescu, M. V., Fuller-Rowell, T. J., Munteanu, V., Minter, C. F., and Millward, G. H.: Validation of the Coupled Thermosphere Ionosphere Plasmasphere Electrodynamics model: CTIPE-Mass Spectrometer Incoherent Scatter temperature comparison, Space Weather, 6, S09005, https://doi.org/10.1029/2007sw000364, 2008.

Codrescu, M. V., Negrea, C., Fedrizzi, M., Fuller-Rowell, T. J., Dobin, A., Jakowsky, N., Khalsa, H., Matsuo, T., and Maruyama, N.: A real-time run of the Coupled Thermosphere Ionosphere Plasmasphere Electrodynamics (CTIPe) model, Space Weather, 10, S02001, https://doi.org/10.1029/2011sw000736, 2012.

Colegrove, F. D., Hanson, W. B., and Johnson, F. S.: Eddy diffusion and oxygen transport in the lower thermosphere, J. Geophys. Res., 70, 4931–4941, https://doi.org/10.1029/jz070i019p04931, 1965.

Danilov, A. D. and Konstantinova, A. V.: Reduction of the atomic oxygen content in the upper atmosphere, Geomagn. Aeronomy, 54, 224–229, https://doi.org/10.1134/s0016793214020066, 2014.

Fuller-Rowell, T. J.: A two-dimensional, high-resolution, nested-grid model of the thermosphere: 1. Neutral response to an electric field "spike", J. Geophys. Res., 89, 2971, https://doi.org/10.1029/ja089ia05p02971, 1984.

Fuller-Rowell, T. J. and Rees, D.: A Three-Dimensional Time-Dependent Global Model of the Thermosphere, J. Atmos. Sci., 37, 2545–2567, https://doi.org/10.1175/1520-0469(1980)037<2545:atdtdg>2.0.co;2, 1980.

Fuller-Rowell, T. J. and Rees, D.: Derivation of a conservation equation for mean molecular weight for a two-constituent gas within a three-dimensional, time-dependent model of the thermosphere, Planet. Space Sci., 31, 1209–1222, https://doi.org/10.1016/0032-0633(83)90112-5, 1983.

Fuller-Rowell, T. J. and Rees, D.: Turbulent diffusion variability and implications for the upper thermosphere, Adv. Space Res., 12, 45–56, https://doi.org/10.1016/0273-1177(92)90443-2, 1992.

Fuller-Rowell, T. J., Rees, D., Quegan, S., Moffett, R., and Bailey, G.: Interactions between neutral thermospheric composition and the polar ionosphere using a coupled

ionosphere-thermosphere model, J. Geophys. Res., 92, 7744, https://doi.org/10.1029/ja092ia07p07744, 1987.

Jacobi, C., Jakowski, N., Schmidtke, G., and Woods, T. N.: Delayed response of the global total electron content to solar EUV variations, Adv. Radio Sci., 14, 175–180, https://doi.org/10.5194/ars-14-175-2016, 2016.

Jakowski, N., Fichtelmann, B., and Jungstand, A.: Solar activity control of ionospheric and thermospheric processes, J. Atmos. Terr. Phys., 53, 1125–1130, https://doi.org/10.1016/0021-9169(91)90061-b, 1991.

Jones, M., Forbes, J. M., and Hagan, M. E.: Tidal-induced net transport effects on the oxygen distribution in the thermosphere, Geophys. Res. Lett., 41, 5272–5279, https://doi.org/10.1002/2014gl060698, 2014a.

Jones, M., Forbes, J. M., Hagan, M. E., and Maute, A.: Impacts of vertically propagating tides on the mean state of the ionosphere-thermosphere system, J. Geophys. Res.-Space, 119, 2197–2213, https://doi.org/10.1002/2013ja019744, 2014b.

Jones, M., Emmert, J. T., Drob, D. P., Picone, J. M., and Meier, R. R.: Origins of the Thermosphere-Ionosphere Semiannual Oscillation: Reformulating the "Thermospheric Spoon" Mechanism, J. Geophys. Res.-Space, 123, 931–954, https://doi.org/10.1002/2017ja024861, 2018.

Keneshea, T. J. and Zimmerman, S. P.: The Effect of Mixing Upon Atomic and Molecular Oxygen in the 70–170 km Region of the Atmosphere, J. Atmos. Sci., 27, 831–840, https://doi.org/10.1175/1520-0469(1970)027<0831:teomua>2.0.co;2, 1970.

Kirchhoff, V. W. J. H. and Clemesha, B. R.: Eddy diffusion coefficients in the lower thermosphere, J. Geophys. Res., 88, 5765, https://doi.org/10.1029/ja088ia07p05765, 1983.

Lee, C.-K., Han, S.-C., Bilitza, D., and Seo, K.-W.: Global characteristics of the correlation and time lag between solar and ionospheric parameters in the 27-day period, J. Atmos. Sol.-Terr. Phys., 77, 219–224, https://doi.org/10.1016/j.jastp.2012.01.010, 2012.

Li, F., Liu, A. Z., and Swenson, G. R.: Characteristics of instabilities in the mesopause region over Maui, Hawaii, J. Geophys. Res., 110, D09S12, https://doi.org/10.1029/2004jd005097, 2005.

Liu, L., Wan, W., Ning, B., Pirog, O. M., and Kurkin, V. I.: Solar activity variations of the ionospheric peak electron density, J. Geophys. Res., 111, A08304, https://doi.org/10.1029/2006ja011598, 2006.

Meraner, K. and Schmidt, H.: Transport of nitrogen oxides through the winter mesopause in HAMMONIA, J. Geophys. Res.-Atmos., 121, 2556–2570, https://doi.org/10.1002/2015jd024136, 2016.

Millward, G., Moffett, R., Quegan, S., and Fuller-Rowell, T.: A coupled thermosphere-ionosphere-plasmasphere model (CTIP), STEP handbook on ionospheric models, 239–279, 1996.

Pilinski, M. D. and Crowley, G.: Seasonal variability in global eddy diffusion and the effect on neutral density, J. Geophys. Res.-Space, 120, 3097–3117, https://doi.org/10.1002/2015ja021084, 2015.

Qian, L., Solomon, S. C., and Kane, T. J.: Seasonal variation of thermospheric density and composition, J. Geophys. Res.-Space, 114, A01312, https://doi.org/10.1029/2008ja013643, 2009.

Qian, L., Burns, A. G., Solomon, S. C., and Wang, W.: Annual/semiannual variation of the ionosphere, Geophys. Res. Lett., 40, 1928–1933, https://doi.org/10.1002/grl.50448, 2013.

Quegan, S., Bailey, G., Moffett, R., Heelis, R., Fuller-Rowell, T., Rees, D., and Spiro, R.: A theoretical study of the distribution of ionization in the high-latitude ionosphere and the plasmasphere: first results on the mid-latitude trough and the light-ion trough, J. Atmos. Terr. Phys., 44, 619–640, https://doi.org/10.1016/0021-9169(82)90073-3, 1982.

Rees, D. and Fuller-Rowell, T.: Understanding the transport of atomic oxygen within the thermosphere, using a numerical global thermospheric model, Planet. Space Sci., 36, 935–948, https://doi.org/10.1016/0032-0633(88)90101-8, 1988.

Ren, D., Lei, J., Wang, W., Burns, A., Luan, X., and Dou, X.: Does the Peak Response of the Ionospheric F2 Region Plasma Lag the Peak of 27-Day Solar Flux Variation by Multiple Days?, J. Geophys. Res.-Space, 123, 7906–7916, https://doi.org/10.1029/2018ja025835, 2018.

Ren, D., Lei, J., Wang, W., Burns, A., Luan, X., and Dou, X.: A Simulation Study on the Time Delay of Daytime Thermospheric Temperature Response to the 27-Day Solar EUV Flux Variation, J. Geophys. Res.-Space, 124, 9184–9193, https://doi.org/10.1029/2019ja027000, 2019.

Ren, D., Lei, J., Wang, W., Burns, A., Luan, X., and Dou, X.: Different Peak Response Time of Daytime Thermospheric Neutral Species to the 27-Day Solar EUV Flux Variations, J. Geophys. Res.-Space, 125, e2020JA027840, https://doi.org/10.1029/2020ja027840, 2020.

Ren, D., Lei, J., Wang, W., Burns, A., and Luan, X.: Observations and simulations of the peak response time of thermospheric mass density to the 27-day solar EUV flux variation, J. Geophys. Res.-Space, 126, e2020JA028756, https://doi.org/10.1029/2020JA028756, 2021.

Richards, P. G., Fennelly, J. A., and Torr, D. G.: EUVAC: A solar EUV Flux Model for aeronomic calculations, J. Geophys. Res., 99, 8981, https://doi.org/10.1029/94ja00518, 1994.

Richmond, A. D., Ridley, E. C., and Roble, R. G.: A thermosphere/ionosphere general circulation model with coupled electrodynamics, Geophys. Res. Lett., 19, 601–604, https://doi.org/10.1029/92gl00401, 1992.

Rishbeth, H.: How the thermospheric circulation affects the ionospheric F2 layer, J. Atmos. Sol.-Terr.l Phys., 60, 1385–1402, https://doi.org/10.1016/s1364-6826(98)00062-5, 1998.

Rishbeth, H., Fuller-Rowell, T., and Rees, D.: Diffusive equilibrium and vertical motion in the thermosphere during a severe magnetic storm : A computational study, Planet. Space Sci., 35, 1157–1165, https://doi.org/10.1016/0032-0633(87)90022-5, 1987.

Sasi, M. N. and Vijayan, L.: Turbulence characteristics in the tropical mesosphere as obtained by MST radar at Gadanki (13.5° N, 79.2° E), Ann. Geophys., 19, 1019–1025, https://doi.org/10.5194/angeo-19-1019-2001, 2001.

Schmölter, E., Berdermann, J., Jakowski, N., Jacobi, C., and Vaishnav, R.: Delayed response of the ionosphere to solar EUV variability, Adv. Radio Sci., 16, 149–155, https://doi.org/10.5194/ars-16-149-2018, 2018.

Schmölter, E., Berdermann, J., Jakowski, N., and Jacobi, C.: Spatial and seasonal effects on the delayed ionospheric response to solar EUV changes, Ann. Geophys., 38, 149–162, https://doi.org/10.5194/angeo-38-149-2020, 2020.

Schmölter, E., Berdermann, J., and Codrescu, M.: The delayed ionospheric response to the 27-day solar rotation period analyzed with GOLD and IGS TEC data, J. Geophys. Res.-Space, 126, e2020JA028861, https://doi.org/10.1029/2020JA028861, 2021.

Shim, J. S., Kuznetsova, M., Rastätter, L., Hesse, M., Bilitza, D., Butala, M., Codrescu, M., Emery, B., Foster, B., Fuller-Rowell, T., Huba, J., Mannucci, A. J., Pi, X., Ridley, A., Scherliess, L., Schunk, R. W., Stephens, P., Thompson, D. C., Zhu, L., Anderson, D., Chau, J. L., Sojka, J. J., and Rideout, B.: CEDAR Electrodynamics Thermosphere Ionosphere (ETI) Challenge for systematic assessment of ionosphere/thermosphere models: NmF2, hmF2, and vertical drift using ground-based observations, Space Weather, 9, S12003, https://doi.org/10.1029/2011sw000727, 2011.

Shimazaki, T.: Effective eddy diffusion coefficient and atmospheric composition in the lower thermosphere, J. Atmos. Terr. Phys., 33, 1383–1401, https://doi.org/10.1016/0021-9169(71)90011-0, 1971.

Siskind, D. E., Drob, D. P., Dymond, K. F., and McCormack, J. P.: Simulations of the effects of vertical transport on the thermosphere and ionosphere using two coupled models, J. Geophys. Res.-Space, 119, 1172–1185, https://doi.org/10.1002/2013ja019116, 2014.

St.-Maurice, J. P. and Torr, D. G.: Nonthermal rate coefficients in the ionosphere: The reactions of O^+ with N_2, O_2, and NO, J. Geophys. Res., 83, 969–977, https://doi.org/10.1029/ja083ia03p00969, 1978.

Su, Y. Z., Bailey, G. J., and Fukao, S.: Altitude dependencies in the solar activity variations of the ionospheric electron density, J. Geophys. Res.-Space, 104, 14879–14891, https://doi.org/10.1029/1999ja900093, 1999.

Swenson, G., Yee, Y., Vargas, F., and Liu, A.: Vertical diffusion transport of atomic oxygen in the mesopause region consistent with chemical losses and continuity: Global mean and inter-annual variability, J. Atmos. Sol.-Terr. Phys., 178, 47–57, https://doi.org/10.1016/j.jastp.2018.05.014, 2018.

Swenson, G. R., Salinas, C. C. J. H., Vargas, F., Zhu, Y., Kaufmann, M., Jones, M., Drob, D. P., Liu, A., Yue, J., and Yee, J. H.: Determination of Global Mean Eddy Diffusive Transport in the Mesosphere and Lower Thermosphere From Atomic Oxygen and Carbon Dioxide Climatologies, J. Geophys. Res.-Atmos., 124, 13519–13533, https://doi.org/10.1029/2019jd031329, 2019.

Tapping, K. F.: Recent solar radio astronomy at centimeter wavelengths: The temporal variability of the 10.7-cm flux, J. Geophys. Res., 92, 829–838, https://doi.org/10.1029/jd092id01p00829, 1987.

Vaishnav, R., Jacobi, C., Berdermann, J., Schmölter, E., and Codrescu, M.: Ionospheric response to solar EUV variations: Preliminary results, Adv. Radio Sci., 16, 157–165, https://doi.org/10.5194/ars-16-157-2018, 2018.

Vaishnav, R., Jacobi, C., and Berdermann, J.: Long-term trends in the ionospheric response to solar extreme-ultraviolet variations, Ann. Geophys., 37, 1141–1159, https://doi.org/10.5194/angeo-37-1141-2019, 2019.

Vaishnav, R., Schmölter, E., Jacobi, C., Berdermann, J., and Codrescu, M.: Ionospheric response to solar extreme ultraviolet radiation variations: comparison based on CTIPe model simulations and satellite measurements, Ann. Geophys., 39, 341–355, https://doi.org/10.5194/angeo-39-341-2021, 2021.

Woods, T. N. and Rottman, G. J.: Solar ultraviolet variability over time periods of aeronomic interest, in: Atmospheres in the Solar System: Comparative Aeronomy, American Geophysical Union, 221–233, 2002.

6 Conclusions

This dissertation provides a comprehensive investigation of the delayed ionospheric response to solar extreme ultraviolet (EUV) variability based on solar activity conditions, and validates the hypothesis put forward by Jakowski et al. (1991). In doing so, the dissertation addresses a very complex interaction between solar EUV and total electron content based on observations and modeling. The Coupled Thermosphere Ionosphere Plasmasphere electrodynamics (CTIPe) model simulations and satellite observations are used to quantify the total electron content and its variations, focusing on the ionospheric delayed response at 27 d solar rotation period, the comparison between the observations and the model simulations, the long-term trends of the delayed response, and the physical mechanism of the delay.

We have attempted to analyze several solar proxies with observed TEC to estimate the ionospheric delay on different time scales. An ionospheric delay of about 1-2 d was observed at the 27 d solar rotation period between the daily GTEC and all solar proxies considered, confirming previous results in the literature (e.g. Jakowski et al., 1991; Afraimovich et al., 2008; Min et al., 2009; Lee et al., 2012; Jacobi et al., 2016). We found that the model-simulated ionospheric delay is in agreement with the delay estimated for the observed TEC. The average delay for the observed (modeled) TEC is about 17 (16) h, which is in close agreement with Schmölter et al. (2020). The study confirms the capabilities of the model to reproduce the delayed ionospheric response to the solar EUV flux with daily and hourly resolution. Moreover, the present work showed the hemispheric differences in the ionospheric delay which is higher in Northern hemisphere than Southern hemisphere.

In addition, model simulations are presented to compare the SOLAR2000 and EUVAC flux models within CTIPe. The analysis shows that the SOLAR2000 flux model simulated TEC overestimates the observed TEC, while its not true for the EUVAC flux model. The

observed large bias in the model is mainly due to the solar EUV flux input and grid resolution. Our results suggest that the model needs to be further improved with respect to the solar flux input to further reduce the observed bias to TEC measurements.

In the present thesis, the GTEC measurements were used and analysed with respect to several solar proxies at different time scales to understand the long-term trend and variations in ionospheric delay and cross-correlation. The cross-wavelet analysis represents the 16 to 32 d period in all solar proxies and GTEC. The maximum correlation with GTEC is observed between the He II index, Mg II index, and F30 in the period range of 16 to 32 d along with a time lag of about 1 d. The most suitable proxy to represent solar activity on the time scales of 16 to 32 and 32 to 64 d during low, medium, and high solar activity is He II. The Mg II index, Ly-α, and F30 can be placed second, as these indices show a strong correlation with GTEC, but with some differences between solar maximum and minimum. From the cross-correlation analysis it is found that the trend depends on solar activity. In addition, the spatial and temporal distribution of the cross-correlation was estimated using the Mg II index. The results show significant temporal and spatial variations. A stronger correlation is observed near the equatorial region with a time lag of about 1-2 d.

From the EOFs analysis, it has been found that the first EOF component captures more than 86 % of the variability, and the first three EOF components explain 99 % of the variance. The EOF analysis suggests that the first component is associated with solar flux and the third EOF component captures geomagnetic activity as well as the remaining part of EOF1. EOF2 captures 11 % of the total variability and shows hemispheric asymmetry. Furthermore, the CTIPe model simulations showed that eddy diffusion is an important factor strongly affecting the delay introduced in TEC as a function of solar activity conditions. The ionospheric delay at the solar rotation period is well reproduced and is about 24 h. The simulations showed that the delay is slightly longer (about 25 h) when the eddy diffusion is reduced to 75% of the original value, while the delay is reduced to 20

h when the diffusion is increased. An increase in eddy diffusion leads to faster transport processes and an increased loss rate, resulting in a decrease in the ionospheric time delay. At low latitudes, the influence of solar activity is stronger, as EUV radiation drives ionization processes that lead to compositional changes. Therefore, the combined effect of eddy diffusion and solar activity shows a larger delay in the low and mid-latitude region. The close link between the delayed ionospheric response to solar EUV variability and eddy diffusion can be explained by the fact that eddy diffusion can effectively affect the neutral composition. Increased eddy diffusion decreases the O density, then decreases the temperature, and then thermally reduces the neutral density. This leads to a decrease in the total electron density and subsequently reduces the ionospheric delay. We are enthusiastic about these findings, which contribute to the further understanding of the delayed response.

The present thesis concludes with a comprehensive model analysis and observational analysis of the delayed ionospheric response to solar radiation variations and possible physical mechanisms of ionospheric delay, covering the approaches known from the literature and highlighting weaknesses in these methods. With the sensitive study of the role of eddy diffusion in relation to the ionospheric delay, it is shown that transport processes are an important factor affecting the ionospheric delay at solar rotation period, confirming the hypothesis of Jakowski et al. (1991). In addition, the comparative studies are used to make various model improvements to understand the physical processes.

Finally, we can summarize that the ionospheric delay estimated with model-simulated TEC is in good agreement with the delay estimated for observed TEC. The eddy diffusion is an important factor affecting the ionospheric delay based on the solar activity conditions.

7 Outlook

For a deeper analysis of the delay mechanism, further studies with models and satellite observations are needed, as suggested by Vaishnav et al. (2021a,b). Vaishnav et al. (2021a) found that eddy diffusion is one of the important factors that strongly influences the ionospheric delay for the 27 days solar rotation period. Therefore, we would like to further investigate the interaction between eddy diffusion or transport process and solar activity. In addition, it would be interesting to study the effect of eddy diffusion on different time scales. Solar activity plays a crucial role in the behaviour of the ionosphere. Therefore, different conditions of solar activity must be considered in such a crucial study. For this study, constant atmospheric conditions were used to understand the role of solar flux and eddy diffusion in ionospheric delay. Further studies are needed in the future to investigate the physical processes using actual observations. It would also be interesting to study the combined effect of solar variations, geomagnetic variations, and lower atmospheric forcing. The effect of the lower atmosphere is included in the CTIPe model only in a statistical sense. Therefore, it should be included to understand the role of the lower atmospheric influence. In addition, understanding the delayed response of the ionosphere during the geomagnetic effect, solar flares, and other very strong events is crucial for the development of the weather prediction model. Therefore, it would be of interest to study these events. Vaishnav et al. (2021b) found that the large bias observed in the physics-based model is mainly due to the input of the solar EUV flux and the grid resolution. The model needs to be further improved with respect to the input of the solar flux. In addition, real observations may lead to a better understanding, so the model needs to be improved with more realistic inputs. Furthermore, Vaishnav et al. (2019) studied the long-term response of the ionosphere using different solar proxies and suggested that He II index is one of the best solar proxies. Therefore, an in-depth analysis on different time scales is required to find out the best solar proxy for representing solar activity in T-I model.

Bibliography

Afraimovich, E. L., Astafyeva, E. I., Oinats, A. V., Yasukevich, Y. V., and Zhivetiev, I. V.: Global electron content: a new conception to track solar activity, Annales Geophysicae, 26, 335–344, https://doi.org/10.5194/angeo-26-335-2008, 2008.

Chen, P., Liu, H., Ma, Y., and Zheng, N.: Accuracy and consistency of different global ionospheric maps released by IGS ionosphere associate analysis centers, Advances in Space Research, 65, 163–174, https://doi.org/10.1016/j.asr.2019.09.042, 2020.

Codrescu, M. V., Fuller-Rowell, T. J., Munteanu, V., Minter, C. F., and Millward, G. H.: Validation of the Coupled Thermosphere Ionosphere Plasmasphere Electrodynamics model: CTIPE-Mass Spectrometer Incoherent Scatter temperature comparison, Space Weather, 6, https://doi.org/10.1029/2007sw000364, 2008.

Codrescu, M. V., Negrea, C., Fedrizzi, M., Fuller-Rowell, T. J., Dobin, A., Jakowsky, N., Khalsa, H., Matsuo, T., and Maruyama, N.: A real-time run of the Coupled Thermosphere Ionosphere Plasmasphere Electrodynamics (CTIPe) model, Space Weather, 10, https://doi.org/10.1029/2011sw000736, 2012.

Dewolfe, A. W., Wilson, A., Lindholm, D. M., Pankratz, C. K., Snow, M. A., and Woods, T. N.: Solar Irradiance Data Products at the LASP Interactive Solar Irradiance Datacenter (LISIRD), In AGU Fall255 Meeting 2010, Abstract GC21B-0881, 2010.

Dudok de Wit, T.: A method for filling gaps in solar irradiance and solar proxy data, Astronomy & Astrophysics, 533, A29, https://doi.org/10.1051/0004-6361/201117024, 2011.

Dudok de Wit, T., Kretzschmar, M., Lilensten, J., and Woods, T.: Finding the best proxies for the solar UV irradiance, Geophysical Research Letters, 36, https://doi.org/10.1029/2009gl037825, 2009.

Dudok de Wit, T., Bruinsma, S., and Shibasaki, K.: Synoptic radio observations as proxies for upper atmosphere modelling, Journal of Space Weather and Space Climate, 4, A06, https://doi.org/10.1051/swsc/2014003, 2014.

Fuller-Rowell, T. J.: A two-dimensional, high-resolution, nested-grid model of the thermosphere: 1. Neutral response to an electric field "spike", Journal of Geophysical Research, 89, 2971, https://doi.org/10.1029/ja089ia05p02971, 1984.

Fuller-Rowell, T. J. and Rees, D.: A Three-Dimensional Time-Dependent Global Model of the Thermosphere, Journal of the Atmospheric Sciences, 37, 2545–2567, https://doi.org/10.1175/1520-0469(1980)037<2545:atdtdg>2.0.co;2, 1980.

Fuller-Rowell, T. J. and Rees, D.: Derivation of a conservation equation for mean molecular weight for a two-constituent gas within a three-dimensional, time-dependent model of the thermosphere, Planetary and Space Science, 31, 1209–1222, https://doi.org/10.1016/0032-0633(83)90112-5, 1983.

Fuller-Rowell, T. J., Rees, D., Quegan, S., Moffett, R., and Bailey, G.: Interactions between neutral thermospheric composition and the polar ionosphere using a coupled ionosphere-thermosphere model, Journal of Geophysical Research, 92, 7744, https://doi.org/10.1029/ja092ia07p07744, 1987.

Haberreiter, M., Schöll, M., Dudok de Wit, T., Kretzschmar, M., Misios, S., Tourpali, K., and Schmutz, W.: A new observational solar irradiance composite, Journal of Geophysical Research: Space Physics, 122, 5910–5930, https://doi.org/10.1002/2016JA023492, 2017.

Hernández-Pajares, M., Juan, J. M., Sanz, J., Orus, R., Garcia-Rigo, A., Feltens, J., Komjathy, A., Schaer, S. C., and Krankowski, A.: The IGS VTEC maps: a reliable source of ionospheric information since 1998, Journal of Geodesy, 83, 263–275, https://doi.org/10.1007/s00190-008-0266-1, 2009.

Jacobi, C., Jakowski, N., Schmidtke, G., and Woods, T. N.: Delayed response of the global total electron content to solar EUV variations, Advances in Radio Science, 14, 175–180, https://doi.org/10.5194/ars-14-175-2016, 2016.

Jakowski, N., Fichtelmann, B., and Jungstand, A.: Solar activity control of ionospheric and thermospheric processes, Journal of Atmospheric and Terrestrial Physics, 53, 1125–1130, https://doi.org/10.1016/0021-9169(91)90061-b, 1991.

Lee, C.-K., Han, S.-C., Bilitza, D., and Seo, K.-W.: Global characteristics of the correlation and time lag between solar and ionospheric parameters in the 27-day period, Journal of Atmospheric and Solar-Terrestrial Physics, 77, 219–224, https://doi.org/10.1016/j.jastp.2012.01.010, 2012.

Millward, G., Moffett, R., Quegan, S., and Fuller-Rowell, T.: A coupled thermosphere-ionosphere-plasmasphere model (CTIP), STEP handbook on ionospheric models, pp. 239–279, 1996.

Min, K., Park, J., Kim, H., Kim, V., Kil, H., Lee, J., Rentz, S., Lühr, H., and Paxton, L.: The 27-day modulation of the low-latitude ionosphere during a solar maximum, Journal of Geophysical Research: Space Physics, 114, 1–8, https://doi.org/10.1029/2008JA013881, 2009.

Noll, C. E.: The crustal dynamics data information system: A resource to support scientific analysis using space geodesy, Advances in Space Research, 45, 1421–1440, https://doi.org/10.1016/j.asr.2010.01.018, 2010.

Pesnell, W. D., Thompson, B. J., and Chamberlin, P. C.: The Solar Dynamics Observatory (SDO), Solar Physics, 275, 3–15, https://doi.org/10.1007/s11207-011-9841-3, 2011.

Quegan, S., Bailey, G., Moffett, R., Heelis, R., Fuller-Rowell, T., Rees, D., and Spiro, R.: A theoretical study of the distribution of ionization in the high-latitude ionosphere and the plasmasphere: first results on the mid-latitude trough and the light-ion trough, Journal of Atmospheric and Terrestrial Physics, 44, 619–640, https://doi.org/10.1016/0021-9169(82)90073-3, 1982.

Richards, P. G., Fennelly, J. A., and Torr, D. G.: EUVAC: A solar EUV Flux Model for aeronomic calculations, Journal of Geophysical Research, 99, 8981, https://doi.org/10.1029/94ja00518, 1994.

Richmond, A. D., Ridley, E. C., and Roble, R. G.: A thermosphere/ionosphere general circulation model with coupled electrodynamics, Geophysical Research Letters, 19, 601–604, https://doi.org/10.1029/92gl00401, 1992.

Romero-Hernandez, E., Denardini, C., Takahashi, H., Gonzalez-Esparza, J., Nogueira, P., de Pádua, M., Lotte, R., Negreti, P., Jonah, O., Resende, L., et al.: Daytime ionospheric TEC

weather study over Latin America, Journal of Geophysical Research: Space Physics, 123, 10–345, https://doi.org/10.1029/2018JA025943, 2018.

Schmölter, E., Berdermann, J., Jakowski, N., Jacobi, C., and Vaishnav, R.: Delayed response of the ionosphere to solar EUV variability, Advances in Radio Science, 16, 149–155, https://doi.org/10.5194/ars-16-149-2018, 2018.

Schmölter, E., Berdermann, J., Jakowski, N., and Jacobi, C.: Spatial and seasonal effects on the delayed ionospheric response to solar EUV changes, Annales Geophysicae, 38, 149–162, https://doi.org/10.5194/angeo-38-149-2020, 2020.

Schöll, M., de Wit, T. D., Kretzschmar, M., and Haberreiter, M.: Making of a solar spectral irradiance dataset I: observations, uncertainties, and methods, Journal of Space Weather and Space Climate, 6, A14, https://doi.org/10.1051/swsc/2016007, 2016.

Tapping, K. F.: Recent solar radio astronomy at centimeter wavelengths: The temporal variability of the 10.7-cm flux, Journal of Geophysical Research, 92, 829, https://doi.org/10.1029/jd092id01p00829, 1987.

Vaishnav, R., Jacobi, C., Berdermann, J., Schmölter, E., and Codrescu, M.: Ionospheric response to solar EUV variations: Preliminary results, Advances in Radio Science, 16, 157–165, https://doi.org/10.5194/ars-16-157-2018, 2018.

Vaishnav, R., Jacobi, C., and Berdermann, J.: Long-term trends in the ionospheric response to solar extreme-ultraviolet variations, Annales Geophysicae, 37, 1141–1159, https://doi.org/10.5194/angeo-37-1141-2019, 2019.

Vaishnav, R., Jacobi, C., Berdermann, J., Codrescu, M., and Schmölter, E.: Role of eddy diffusion in the delayed ionospheric response to solar flux changes, Annales Geophysicae, 39, 641–655, https://doi.org/10.5194/angeo-39-641-2021, 2021a.

Vaishnav, R., Schmölter, E., Jacobi, C., Berdermann, J., and Codrescu, M.: Ionospheric response to solar extreme ultraviolet radiation variations: comparison based on CTIPe model simulations and satellite measurements, Annales Geophysicae, 39, 341–355, https://doi.org/10.5194/angeo-39-341-2021, 2021b.

Woods, T. N. and Rottman, G. J.: Solar ultraviolet variability over time periods of aeronomic
    interest, in: Atmospheres in the Solar System: Comparative Aeronomy, pp. 221–233, American
    Geophysical Union, https://doi.org/10.1029/130gm14, 2002.

Woods, T. N., Bailey, S., Eparvier, F., Lawrence, G., Lean, J., McClintock, B., Roble, R.,
    Rottman, G. J., Solomon, S. C., Tobiska, W. K., et al.: TIMED solar EUV experiment,
    Physics and Chemistry of the Earth, Part C: Solar, Terrestrial & Planetary Science, 25, 393–
    396, https://doi.org/10.1016/s1464-1917(00)00040-4, 2000.

Woods, T. N., Eparvier, F. G., Bailey, S. M., Chamberlin, P. C., Lean, J., Rottman, G. J.,
    Solomon, S. C., Tobiska, W. K., and Woodraska, D. L.: Solar EUV Experiment (SEE):
    Mission overview and first results, Journal of Geophysical Research: Space Physics, 110,
    https://doi.org/https://doi.org/10.1029/2004JA010765, 2005.

Woods, T. N., Eparvier, F. G., Hock, R., Jones, A. R., Woodraska, D., Judge, D., Didkovsky,
    L., Lean, J., Mariska, J., Warren, H., McMullin, D., Chamberlin, P., Berthiaume, G., Bailey,
    S., Fuller-Rowell, T., Sojka, J., Tobiska, W. K., and Viereck, R.: Extreme Ultraviolet Vari-
    ability Experiment (EVE) on the Solar Dynamics Observatory (SDO): Overview of Science
    Objectives, Instrument Design, Data Products, and Model Developments, Solar Physics, 275,
    115–143, https://doi.org/10.1007/s11207-009-9487-6, 2010.

Acknowledgements

Curriculum Vitae

Personal Data

Name:	Rajesh Ishwardas Vaishnav
Born:	21 February 1990 in Rajasthan, India
Address:	Stephanstr. 3, 04103 Leipzig
Phone:	+49 341/97-32881
Email:	rajesh_ishwardas.vaishnav@uni-leipzig.de

Research Experience

since 05/2017	PhD candidate at the Institute for Meteorology, University of Leipzig Department: Middle and Upper Atmosphere Project: "Delayed Response of the Ionosphere to solar UV/EUV VARiability (DRIVAR)." Supervisor: Prof. Dr. Christoph Jacobi
05-12/2016	Visiting Assistant at Physical Research Laboratory, A Unit of Department of Space, Government of India Department: Space and Atmospheric Sciences
01-03/2016	Student Visitor at Physical Research Laboratory, A Unit of Department of Space, Government of India Department: Space and Atmospheric Sciences
11/2014-12/2015	Project Associate at Physical Research Laboratory, A Unit of Department of Space, Government of India Department: Space and Atmospheric Sciences Project: "Ceilometer at Ahmedabad, Lidar at Mt. Abu." Supervisor: Dr. Som Kumar Sharma

Education

2014	Master of Science, Physics,
	Gujarat University, Gujarat

2012	Bachelor of Science, Physics,
	Gujarat University, Gujarat

2007	Higher Secondary, Science,
	Central Board of Secondary Education, Rajasthan

Awards

Received "Young Scientist Award" and "Young Scientist Best Poster Award" during Kleinheubacher Tagung, an International Union of Radio Science (URSI) conference in 2019, Germany.

Paper Contributing to the Thesis and Personal Contribution

Rajesh Vaishnav, Christoph Jacobi, Jens Berdermann, Mihail Codrescu, and Erik Schmölter, Role of eddy diffusion in the delayed ionospheric response to solar flux changes, *Annales Geophysicae*, 39, 641–655, 2021, https://doi.org/10.5194/angeo-39-641-2021.

- performed CTIPe model simulations

- performed the data analysis and provided all figures

- prepared the first draft of the manuscript

Rajesh Vaishnav, Erik Schmölter, Christoph Jacobi, Jens Berdermann, and Mihail Codrescu, Ionospheric response to solar extreme ultraviolet radiation variations: comparison

based on CTIPe model simulations and satellite measurements, *Annales Geophysicae*, 39, 341–355, 2021, https://doi.org/10.5194/angeo-39-341-2021.

- performed CTIPe model simulations

- performed the data analysis and provided all figures, together with E. Schmölter

- prepared the first draft of the manuscript

Rajesh Vaishnav, Christoph Jacobi, and Jens Berdermann, Long-term trends in the ionospheric response to solar extreme-ultraviolet variations, *Annales Geophysicae*, 37, 1141–1159, 2019, https://doi.org/10.5194/angeo-37-1141-2019.

- performed the data analysis and provided all figures

- prepared the first draft of the manuscript

Rajesh Vaishnav, Christoph Jacobi, Jens Berdermann, Erik Schmölter, and Mihail Codrescu, Ionospheric response to solar EUV variations: Preliminary results, *Advances in Radio Science*, 16, 157–165, 2018, https://doi.org/10.5194/ars-16-157-2018.

- performed the data analysis and provided all figures

- performed CTIPe model simulations

- prepared the first draft of the manuscript

Other Peer-reviewed Papers

Rajesh Vaishnav, Yuyan Jin, Md Golam Mostafa, Sara R. Aziz, Shunrong Zhang, and Christoph Jacobi, Study of the upper transition height using ISR observations and IRI predictions over Arecibo, *Advances in Space Research*, 68(5), 2177-2185, 2021, https://doi.org/10.1016/j.asr.2020.10.010.

Vaidehi Joshi, Som Sharma, Kondapalli Niranjan Kumar, Nisha Patel, Prashant Kumar, Hassan Bencherif, Priyanka Ghosh, Chintan Jethva, and **Rajesh Vaishnav**, Analysis of the middle atmospheric ozone using SABER observations: A study over mid-latitudes in the northern and southern hemispheres, *Climate Dynamics*, 54, 2481–2492, 2020, https://doi.org/10.1007/s00382-020-05124-6.

Erik Schmölter, Jens Berdermann, Norbert Jakowski, Christoph Jacobi, and **Rajesh Vaishnav**, Delayed response of the ionosphere to solar EUV variability, *Advances in Radio Science*, 16, 149–155, 2018, https://doi.org/10.5194/ars-16-149-2018.

Rajesh Vaishnav, Som Sharma, Prashant Kumar, S. Lal, and K. K. Shukla, A comprehensive statistical study of cloud base height by using Ceilometer over Western India, *Advances in Space Research*, 63(5), 1708-1718, 2018, https://doi.org/10.1016/j.asr.2018.11.006.

Arun S. H., Som Kumar Sharma, Sasmita Chaurasia, **Rajesh Vaishnav**, and Raj Kumar, Fog/low clouds detection over the Delhi Earth Station using the Ceilometer and the INSAT-3D/3DR satellite data, *International Journal of Remote Sensing*, 39(12), 4130-4144, 2018, https://doi.org/10.1080/01431161.2018.1454624.

Som Sharma, Prashant Kumar, **Rajesh Vaishnav**, Chintan Jethva, and Hassan Bencherif, Evaluation of Inter-hemispheric Characteristics of the Tropopause-Stratopause-Mesopause over Sub-tropical regions, *Pure and Applied Geophysics*, 175, 1123–1137, 2017, https://doi.org/10.1007/s00024-017-1706-8.

Som Kumar Sharma, Prashant Kumar, **Rajesh Vaishnav**, Chintan Jethva, and G. Beig, A study of the middle atmospheric thermal structure over western India: Satellite data and comparisons with models, *Advances in Space Research*, 60(11), 2402-2413, 2017, https://doi.org/10.1016/j.asr.2017.09.021.

Som Kumar Sharma, **Rajesh Vaishnav**, Krishna Kumar Shukla, Shyam Lal, Harish Chandra, and Yashwant B. Acharya, Rayleigh Lidar observed atmospheric temperature characteristics over a western Indian location: Intercomparison with satellite observations and models, *The European Physical Journal D*, 71, 187, 2017, https://doi.org/10.1140/epjd/e2017-70609-9.

Som Kumar Sharma, Prashant Kumar, **Rajesh Vaishnav**, Krishna Kumar Shukla, and Devulapalli Venkata Phanikumar, Analysis of total column ozone, water vapour and aerosol optical thickness over Ahmedabad, India, *Meteorological Applications*, 25, 33–39, 2018, https://doi.org/10.1002/met.1666.

Som Kumar Sharma, Prashant Kumar, **Rajesh Vaishnav**, Harish Chandra, Harish Gadhavi, S Sridharan, and A Jayaraman, Analysis of Stratospheric Sudden Warming (SSW) over Tropical and Sub-tropical Regions of India using Rayleigh Lidar, *International Journal of Remote Sensing*, 38(15), 4285-4302 2016, https://doi.org/10.1080/01431161.2017.1317935.

Som Sharma, Prashant Kumar, Chintan Jethva, **Rajesh Vaishnav**, and Hassan Bencherif, Investigations of the middle atmospheric thermal structure and oscillations over sub-tropical regions in the Northern and Southern Hemispheres, *Climate Dynamics*, 48, 3671–3684, 2016, https://doi.org/10.1007/s00382-016-3293-2.

Som Sharma, Prashant Kumar, **Rajesh Vaishnav**, and Shyam Lal, Evaluation of clouds simulated by a weather model over western India, *Remote Sensing Letters*, 7(9), 905–913, 2016, https://doi.org/10.1080/2150704X.2016.1195934.

Som Kumar Sharma, H Chandra, G Beig, Prashant Kumar and **Rajesh Vaishnav**, Investigations of mesospheric temperature inversions over sub-tropical location using

lidar and satellites measurements, *Journal of Atmospheric and Solar-Terrestrial Physics*, 138, 54-65, 2016, https://doi.org/10.1016/j.jastp.2015.12.007.

Som Kumar Sharma, **Rajesh Vaishnav**, Munn V Shukla, Prashant Kumar, Prateek Kumar, P.K. Thapliyal, S. Lal, and Y. B. Acharya, Evaluation of cloud base height measurement from Ceilometer CL31 and MODIS satellite over Ahmedabad, India, *Atmospheric Measurement Techniques*, 9, 711-719, 2016, https://doi.org/10.5194/amt-9-711-2016.

Som Sharma, H. Chandra, and **Rajesh Vaishnav**, Study of the Sporadic E layer over Ahmedabad during high and low sunspot activity years, *Asian Journal of Physics*, 24(6), 875-883, 2015.

Further Publications

Rajesh Vaishnav and Christoph Jacobi, Ionospheric response to the 25-26 August 2018 intense geomagnetic storm, *Rep. Inst. Meteorol. Univ. Leipzig*, 58, 1-10, 2020. https://nbn-resolving.org/urn:nbn:de:bsz:15-qucosa2-741226.

Rajesh Vaishnav, Christoph Jacobi, Jens Berdermann, Mihail Codrescu, and Erik Schmölter, Ionospheric response to solar variability during solar cycles 23 and 24, *Rep. Inst. Meteorol. Univ. Leipzig* 57, 97-106, 2019, ISBN: 978-3-9814401-7-1, https://nbn-resolving.org/urn:nbn:de:bsz:15-qucosa2-741822.

Rajesh Vaishnav, Christoph Jacobi, Jens Berdermann, Erik Schmölter, and Mihail Codrescu, Ionospheric response during low and high solar activity, *Rep. Inst. Meteorol. Univ. Leipzig* 56, 1-10, 2018, ISBN: 978-3-9814401-6-4, https://nbn-resolving.de/urn:nbn:de:bsz:15-qucosa2-317670.

Affirmation

I, Rajesh Ishwardas Vaishnav, declare that I have written this dissertation with the title "Delayed Ionospheric Response to Solar EUV/UV Radiation Variations „ on my own and without illegal help of others.

I did not use any other sources, references or other kind of aid than stated in this thesis. Furthermore, I confirm that this dissertation has not been submitted to any other examination at the University of Leipzig nor to any other institute or university.

....

Place, Date   Signature